Contents

1. Introduction

1.1 Overview

Magnetic ordering induced by defects in semiconductor materials holds the prospect of integrating the complementary functions of magnetism and semiconductor electronics within single semiconductor/magnetic hybrid devices in the emerging field of spintronics. This has successfully been demonstrated [1] by use of diluted magnetic semiconductors (DMS), which are semiconductor materials in which a small fraction of their constituent atoms have been replaced by impurity atoms (commonly those of transition metal ions) capable of inducing ordered magnetic moments in the semiconductor matrix. In particular, a magnetic ground state in which interactions between spins of individual defect centres establishes a collective net magnetic moment in the semiconductor material is desirable since it can be adapted to serve as a means to inject and control spin polarised currents in spintronic device applications [2,3].

In recent years, there has been an intense search for room temperature magnetic ordering in semiconductors doped with transition metal impurities. III-V and II-IV compound semiconductors have mainly been considered as possible candidates, however, low Curie temperature T_C [1], the temperature at which magnetism is lost, and lack of other fundamental spintronic material properties [4] have led to a continued search for alternative materials. An important step towards room temperature magnetic ordering in DMSs was the theoretical prediction of the reciprocal dependence of T_C on the host semiconductor's lattice constant (a_0) as $1/a_0^3$ for hole mediated ferromagnetism [5]. This prediction makes diamond one of the best choices of a host semiconductor material to study room temperature ferromagnetic ordering since it has the smallest lattice constant compared to all other known semiconductors [6]. In addition, diamond's extreme properties [7] makes it highly suitable for spin-based electronic devices capable of operating at high temperature, high frequency and high power applications. In particular, diamond's potential in spintronic applications has already been demonstrated in the nitrogen vacancy (N-V) centre [8], as well as in N-Cr [9] and N-Ni [10] complexes. Recent studies have further shown that isotopically engineered diamond films have the longest room-temperature spin dephasing times ($T_2 = 1.8$ ms) ever

observed in solid-state systems [11], thereby making diamond an attractive candidate material for spintronic and quantum computing applications [12].

In this Thesis, we report *ab initio* Density Functional Theory calculations on the energetic stability and magnetic ordering properties of 3*d* transition metals in diamond, and show that transition metal-doped diamond may form an energetically stable diluted magnetic semiconductor which, in addition to diamond's extreme properties, may successfully be considered for room temperature spintronic device applications.

1.2 Properties of diamond

1.2.1 Crystal structure

Diamond is the solid crystalline form of carbon in which the *s* and *p* atomic orbitals hybridise to form very strong tetrahedral sp^3 bonds. The stable form of carbon is graphite in which the carbon atoms form two dimensional sp^2 bonds, but due to the very large energy barrier between the sp^3 and sp^2 bonding states, diamond can practically be considered as a stable material. The crystal structure of diamond is equivalent to a face-centred cubic (fcc) lattice, with a basis of two identical carbon atoms at $(0, 0, 0)$ and $(1/4\,, 1/4\,, 1/4)$. The conventional unit cell of diamond is cubic (Figure 1), with a lattice constant a_0 of 3.567 Å [6] at room temperature. Each carbon atom in diamond is surrounded by four nearest neighbours which are connected by tetrahedral covalent bonds separated by a distance of 1.544 Å.

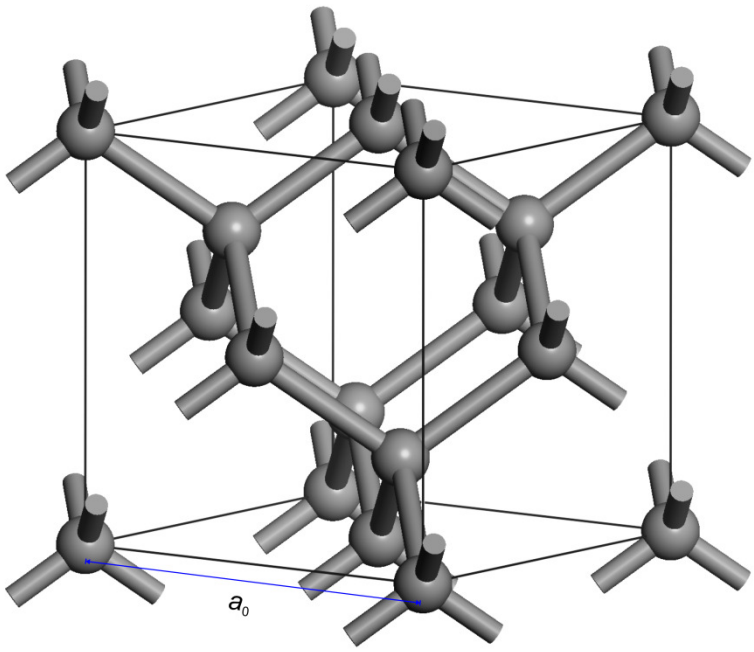

Figure 1.1: Illustration of a diamond unit cell showing tetrahedral bond arrangement.

1.2.2 Classification of diamond

The physical classification of diamond is based on the optical absorption of nitrogen or boron, which are the most common impurities in both natural and synthetic diamond [12]. A brief overview of the classification scheme based on the specifics of optical absorption is outlined below [7,13,14].

1. **Type I diamond**

Type I diamond comprises diamonds in which impurity-related optical and paramagnetic absorption are dominated by nitrogen defects. It is further classified into type Ia and Ib diamonds.

Type Ia comprises nitrogen as non-paramagnetic aggregates, A or B, in fairly substantial concentrations (up to 3000 ppm). Most natural diamonds are of this type. Diamonds containing type A aggregates comprise two nitrogen atoms on adjacent lattice sites, while type B aggregates comprise of four nitrogen atoms symmetrically surrounding a vacancy [14].

Type Ib diamonds contain paramagnetic single substitutional nitrogen atoms as the dominating defects on isolated substitutional lattice sites at concentrations up to 500ppm. These diamonds are rare in nature, but most synthetic diamonds are of this type.

2. **Type II diamond**

Type II diamond comprises of diamonds showing no optical or paramagnetic absorption due to nitrogen related defects, but they are also rare in nature. The nitrogen content in true type II diamonds is below 10^{17} cm^{-3} [7], and they are further categorised into type IIa or type IIb depending on their nitrogen or boron concentration.

Type IIa diamonds have nitrogen concentrations which is low enough such that that it can not be detected by IR or UV absorption measurements.

Type IIb diamonds contains larger proportions of boron than nitrogen. The nitrogen concentration is so low that some of the boron acceptors are not compensated, making the crystal a *p*-type semiconductor. This type of diamond has a blue colour whose depth of colouration varies with the boron concentration.

1.2.3 Diamond as an electronic material

Apart from its appeal as a gemstone, diamond has outstanding mechanical, chemical and electronic properties [7] which arise from its strong sp^3 bonding: diamond is the hardest known material, has the highest thermal conductivity at room temperature, is transparent over a wide range of wavelengths, is the stiffest and least compressible material, and is inert to most chemical reagents [15,16]. In addition, diamond is a wide band gap semiconductor ($E_g = 5.49$ eV at room temperature [6]) with very high electron and hole mobilities [17], electrical breakdown field (about 33 times more than that of silicon [18]) and thermal conductivity (about five times that of copper [19]) at room temperature, which makes it highly suitable for high voltage, high frequency and high power electronic device applications. Table 1.1 summarizes some of the properties of diamond as compared to other common semiconductor materials.

	Diamond	4H-SiC	Si	GaAs	GaN
Band gap (eV)	5.49	3.3	1.12	1.43	3.45
Dielectric constant	5.5	10.1	11.9	13.1	9
Electrical breakdown field ($KVcm^{-1}$)	10000	2200	300	400	2000
Electron mobility ($cm^2V^{-1}s^{-1}$)	4500	1000	1500	8500	1250
Hole mobility ($cm^2V^{-1}s^{-1}$)	3800	115	600	400	850
e-drift velocity ($\times 10^7\ cms^{-1}$)	2.7	2	1	1	2.2
Thermal conductivity ($Wcm^{-1}K^{-1}$)	22	4.9	1.5	0.46	1.3

Table 1.1: Intrinsic material properties of synthetic diamond, Si, 4H-SiC, GaN and GaAs at room temperature [19,20]. 4H is the polytype of SiC that is considered best suited for high power electronic devices as it has the highest mobility.

1.3 Thesis outline

This Thesis presents a quantum mechanical study of the energetic stability and magnetic ordering of 3*d* transition metal impurities at various lattice sites and charge states in diamond. A brief overview of each Chapter is outlined in this Section.

Chapter one gives a general introduction leading into the subject of this research. A brief overview of the current status of semiconductor spin-based electronics and an outline of the properties of diamond are presented.

In Chapter two, a theoretical background of many-body quantum mechanical modelling approach, and the computational methods used in this research are presented. Of particular interest in this Thesis is the Density Functional Theory (DFT) approach which is discussed in detail. The different approximations commonly used to treat the exchange and correctional potential due to many-body interactions in numerical implementation of the Density Functional Theory are discussed. In addition, both the full potential and pseudopotential approaches for solving the Kohn-Sham equations are examined. A general overview of the reliability and accuracy of the DFT approach in calculating material properties is also presented.

Chapter three presents a literature review on diluted magnetic semiconductors and the potential of a diamond-based diluted magnetic semiconductor. In addition, a brief overview of various point defects and impurities, including transition metals and common dopants in diamond is given.

The results of energetic stability of single 3*d* transition metals in diamond are presented in Chapter four, where it is shown that the formation energies of these impurities in diamond varies significantly for different lattice sites and charge states. Trends in ionization energies across the 3*d* series are also presented in Chapter four, and it is shown that incorporation of 3*d* transition metals in diamond introduces multiple impurity levels in diamond's band gap, thus underlining the importance of considering their magnetic properties in various charge states.

Chapter five presents the electronic structure, spin, and symmetry properties of isolated 3*d* transition metals in diamond calculated from a 64-atom diamond supercell. Results of the band structures of all the 3*d* transition metal impurities are presented, and it is shown that incorporation of these impurities into diamond induces strongly spin polarised impurity bands into diamond's band gap. The majority of 3*d* transition metals in various charge states are found to induce non-vanishing magnetic moments in diamond, thus indicating that it is of interest to establish possible magnetic ordering properties of transition metal doped-diamond in the search for a diamond-based diluted magnetic semiconductor.

Chapter six presents the results of magnetic interactions between 3*d* transitions metal atoms in diamond calculated from a 128 atom-diamond supercell containing two transition metal

atoms. The magnetic ordering and magnetic stabilization energies of 3*d* transition metal-doped diamond are demonstrated to be significantly dependent on the charge state of the transition metal impurity, and therefore on the type of diamond doping (intrinsic, *n*-type or *p*-type). Cr, Mn, Co and Fe are predicted to order ferromagnetically in diamond with significant magnetic moments and stabilization energies, with substitutional Fe^{+2} and Fe^{+1} predicted to have the highest ferromagnetic stabilization energy of 33 meV, which is much higher than what has been obtained in other semiconductors which have been considered so far for spintronic applications. In addition to diamond's extreme properties, these results demonstrate that transition metal-doped diamond may form a stable diluted magnetic semiconductor which is likely to order ferromagnetically at high Curie temperatures, and is likely to have significant applications in the emerging field of spintronics.

A summary and conclusions of the results obtained in this study are given in Chapter seven.

2. Theoretical background

2.1 Quantum Mechanical Modelling

Quantum mechanical modelling offers a possibility to study the properties of complex many-body systems through the use of computational simulations. This approach plays an important role in elucidating certain properties of material systems with sufficient accuracy where experimental results are inconclusive, or not available [21].

Experimental techniques such as Electron Spin Resonance (ESR) have the ability to determine, for example, the symmetry of a magnetic defect centre, but unfortunately not all properties of such a defect centre can be established precisely using experimental approaches [22,23]. In particular, there is a lack of direct experimental techniques to study some magnetic properties of materials such as spin polarised electronic structure and magnetic moment distribution, including half-metallic ordering, which are crucial for spintronic device development [24]. One possibility to study such properties is through the use of quantum mechanical modelling techniques. This approach is capable of providing relevant information up to good accuracy on the band structure of a material, its spin density distribution and type magnetic ordering, from which promising materials for spintronic applications can be predicted.

Modelling of solid state systems using quantum mechanical techniques requires solving the Schrödinger equation for a system containing a large number of interacting particles ($N \sim 10^{23}$). The total energy of such a system (Equation 2.1) comprise of the kinetic energy of both the nucleus and electrons (first term) and electron-electron interactions (second term), together with the combined effects of electron-nuclei (third term) and nuclei-nuclei interactions (fourth term) which makes it difficult to solve analytically.

Therefore, approximate techniques are required to obtain the numerical solution of the Schrödinger equation describing such a system of many-body interacting particles. These techniques include molecular mechanics, semi-empirical and *ab initio* or first principles methods [25].

$$H = -\frac{\hbar^2}{2}\sum_{i}^{N+ZN}\left(\frac{\nabla^2_{\mathbf{r}_i(nucl)}}{m_{nucl}} - \frac{\nabla^2_{\mathbf{r}_i(elec)}}{m_{elec}}\right) + \frac{1}{8\pi\varepsilon_o}\sum_{i\neq j}^{N+ZN}\frac{e^2}{\left|\mathbf{r}_{i(elec)} - \mathbf{r}_{j(elec)}\right|}$$

$$-\frac{1}{4\pi\varepsilon_o}\sum_{i,j}^{N+ZN}\frac{e^2 Z_i}{\left|\mathbf{r}_{i(nucl)} - \mathbf{r}_{j(elec)}\right|} + \frac{1}{8\pi\varepsilon_o}\sum_{i,j}^{N+ZN}\frac{e^2 Z_i Z_j}{\left|\mathbf{r}_{i(nucl)} - \mathbf{r}_{j(nucl)}\right|} \qquad (2.1)$$

Ab initio electronic structure methods provide the most accurate and consistent predictions over a wide range of systems by solving the Schrödinger equation of a many-body interacting system with as few approximations as possible, and are computationally intensive. On the other hand, semi-empirical methods replace explicit calculations with parameters which have been fitted with experimental data, while molecular mechanics methods are based upon the principles of classical physics ("ball and spring models") and are purely empirical in nature, hence computationally fast. Therefore, semi-empirical and molecular mechanics methods neglect explicit treatment of the electronic structure by employing experimental data, hence are limited in scope and can only address systems similar to the ones they have been parameterized from; but they often provide the only means to study very large chemical systems (*e.g.* polymers or solutions) or non-homogeneous mixtures where exact treatment of electronic structure is not critical. On the other hand, *ab initio* methods can explicitly treat the electronic structure of materials from "first principles'' and are capable of addressing spin related properties of solid state systems, hence have been used in this study to model the magnetic properties of transition metal defects in diamond.

2.1.1 *Ab initio* electronic structure methods

Ab initio electronic structure techniques strive to find an accurate solution to the Schrödinger equation for a set of electrons moving in a potential created by the atomic nuclei. These techniques predict the electronic and geometric structure of a solid with good accuracy by calculating the quantum-mechanical total energy of the system, and subsequently minimizing it (with respect to the electronic and nuclear coordinates) to determine the structure of minimum energy corresponding to a possible stable state of the system. In order to achieve this, a series of approximation techniques are required to separate the electron-electron, electron-nuclei and nuclei-nuclei interaction terms in a many-body interacting system (Equation 2.1).

The first approximation (the Born-Oppenheimer approximation [26]) ignores the kinetic energy of the nuclei by treating it adiabatically due to the large difference in mass between the electrons and nuclei. Consequently, the electrons are assumed to respond instantaneously to the motion of the nuclei. This leads to the separation of electronic and nuclear coordinates in the many-body wavefunctions, thus reducing the nuclear potential component of Equation 2.1 to a given source of positive charge external to the electron cloud. The Born-Oppenheimer approximation therefore reduces the complexity of the many-interacting body problem to that of a many-interacting electron problem, whose Hamiltonian can explicitly be written as

$$\mathbf{H} = E_{T_{KE}} + E_{\mathbf{V}_{Int}} + \left(E_{\mathbf{V}_{Ext}} + E_{II} \right) \tag{2.2}$$

where

$E_{T_{KE}} = \frac{\hbar^2}{2m} \sum_j \nabla_j^{\,2}$ is the kinetic energy operator of the electron gas,

$E_{\mathbf{V}_{Int}} = \frac{1}{2} \sum_{i \neq j} \frac{1}{\left| \mathbf{r}_i - \mathbf{r}_j \right|}$ is the potential due to the electron-electron interactions and

$E_{\mathbf{V}_{Ext}} = \sum_{i,I} V_I \left(\left| \mathbf{r}_i - \mathbf{R}_I \right| \right)$ is the potential due to the classical interaction of the nuclei. E_{II} referes to any other terms that may contribute to the total energy of the system but are not relevant to the problem of describing electron-electron interactions [26].

The complete solution to Equation (2.2) still remains difficult to achieve due to the exchange and correlation effects of coulomb and electronic interactions whose exact functional form is not known – but are of fundamental importance in describing solid state processes. Hence further approximations are needed to solve the many interacting-electron problem described in Equation 2.2 for a set of electrons moving in a potential created by the nuclei in a particular solid state system. The most widely used approximations are the Density Functional Theory (DFT) and the Hartree-Fock (HF) formulation. The HF approach often includes various semi-empirical approximations and is based upon the 3N dimensional wave functions of the electrons. It treats electron exchange exactly but ignores correlation effects and hence cannot be used to model metallic and magnetic systems. On the other hand, the

DFT scheme is based on the three dimensional electron density and, unlike the HF formulation, treats both exchange and correlation effects approximately. The DFT technique is very versatile and computationally simple compared to the HF approach and other semi-empirical methods, and can be used to model both metallic and magnetic systems (including heavy atoms) with good accuracy.

2.2 Density Functional Theory

The Density functional theory (DFT) reduces the complexity of a strongly interacting electron-electron system in the presence of the atomic nuclei (Equation 2.2) by mapping it exactly onto that of a single particle moving in an effective non-local potential [27]. Although this effective potential is not precisely known, simple approximations to it work remarkably well in predicting the properties of solid-state and other material systems with good accuracy as compared to experimental techniques.

The basic concept of the Density Functional Theory is that any property of a system of many-interacting particles can be viewed as a functional of its ground state charge density. For a system of interacting electrons, DFT states that the total energy, E_T of interacting electrons in an external potential, $V_{Ext}(\mathbf{r})$ is given exactly as a functional of its ground state density, $\rho_o(\mathbf{r})$ [22], and can be written explicitly as

$$E_T = E\left[\rho_o(\mathbf{r})\right]. \tag{2.3}$$

DFT is based upon the Hohenberg-Kohn theory [27] which formulates a one-to-one correspondence between the ground state electron density, $\rho_o(\mathbf{r})$ of a many electron system and its external potential, $V_{Ext}(\mathbf{r})$ up to an additive constant. Also, for any particular $V_{Ext}(\mathbf{r})$, the exact ground state energy of the system is the global minimum value of its energy functional which corresponds to the exact ground state electron density. Therefore, the total ground state energy of the system for any external potential may be written as a sum of its kinetic and interaction energies, plus an external potential which is uniquely determined by the ground state electronic density:

$$E_T\left[\rho(\mathbf{r})\right] = T_{KE}\left[\rho(\mathbf{r})\right] + V_{Int}\left[\rho(\mathbf{r})\right] + V_{Ext}\left[\rho(\mathbf{r})\right] \tag{2.4}$$

For a particular $V_{Ext}\left[\rho(\mathbf{r})\right]$, the kinetic energy of the electrons $T_{KE}\left[\rho(\mathbf{r})\right]$ and the internal interaction potential $V_{Int}\left[\rho(\mathbf{r})\right]$ is a universal functional of the electron density, called the Hohenberg-Kohn density functional $F_{HK}\left[\rho(\mathbf{r})\right]$.The internal potential contains contributions from electron exchange and correlation interaction potential V_{xc} plus the contribution due to the classical electrostatic energy [39], called the Hartree potential V_H . Therefore, the Hohenberg-Kohn density functional can be expressed as

$$F_{HK}\left[\rho(\mathbf{r})\right] = T\left[\rho(\mathbf{r})\right] + \int \frac{\rho(\mathbf{r}')}{|\mathbf{r}-\mathbf{r}'|} d\mathbf{r}' + V_{xc}\left[\rho(\mathbf{r})\right] \tag{2.5}$$

where $T\left[\rho(\mathbf{r})\right]$ is the kinetic energy functional of the non-interacting system of electrons and $V_H = \int \frac{\rho(\mathbf{r}')}{|\mathbf{r}-\mathbf{r}'|} d\mathbf{r}'$ is the Hartree potential due the classical electrostatic energy. The total energy functional given in Equation 2.4 can thus be re-written as

$$E_{Tot}\left[\rho(\mathbf{r})\right] = T\left[\rho(\mathbf{r})\right] + \int \frac{\rho(\mathbf{r}')}{|\mathbf{r}-\mathbf{r}'|} d\mathbf{r}' + V_{xc}\left[\rho(\mathbf{r})\right] + V_{Ext}\left[\rho(\mathbf{r})\right] \tag{2.6}$$

which may be interpreted as a one-electron equation with the energy functional of a non-interacting classical electron gas, subject to two external potentials: one due to the nuclei $V_{Ext}(\mathbf{r})$ and the other due to exchange and correlation effects $V_{xc}(\mathbf{r})$. Consequently these external potentials and the electron density completely define the quantum mechanical problem. The wave functions are in principle uniquely determined via the corresponding Schrödinger equation, from which all system properties dependent on the total energy can be obtained.

The minimal value of the total energy functional defined by Equation (2.6) is determined by applying Rayleigh-Ritz variational principle [28-30], and it can be shown that the true minimum is reached when the electron density is the correct ground state density. The corresponding Hamiltonian to the variational total energy functional is called the Kohn-Sham equation [27]:

$$\left[-\frac{\hbar^2}{2m}\Delta^2 + \int \frac{\rho(\mathbf{r})}{\mathbf{r}-\mathbf{r}'}d\mathbf{r}' + V_{Ext}(\mathbf{r}) + V_{xc}(\mathbf{r})\right]\psi_i(\mathbf{r}) = H_{KS}\psi_i(\mathbf{r}) = \varepsilon_i\psi_i(\mathbf{r}) \tag{2.7}$$

which effectively replaces the many-body problem by an auxiliary independent one particle problem (a new Schrödinger-like equation) expressed in terms of the charge density, where ψ_i are the single particle Kohn-Sham wave functions (which are the *N* lowest-energy solutions of the Kohn-Sham equation) defined by

$$\rho(\mathbf{r}) = \sum_{i=1}^{N} \psi(\mathbf{r})^* \psi(\mathbf{r}) \tag{2.8}$$

and the exchange correlation potential is given by its functional derivative with respect to the electron density

$$V_{xc}(\mathbf{r}) = \frac{\delta E_{xc}\left[\rho(\mathbf{r})\right]}{\delta\rho(\mathbf{r})}. \tag{2.9}$$

In order to solve the Kohn-Sham single particle equations (Equation 2.7), the electronic wave functions for the occupied orbitals need to be known. Unfortunately, these wave functions depend on the electron density which is also initially unknown. Therefore solving the Kohn-Sham equations requires an iterative process where an initial trial electron density $\rho_1(\mathbf{r})$ needs to be "guessed", usually by superimposing the isolated electron densities, from which the starting wave functions can be obtained. These in turn are used to construct the starting Kohn-Sham Hamiltonian from which an improved electron density $\rho_2(\mathbf{r})$ is obtained. The resulting wave functions are then used to obtain better approximations to the electron density $\rho_{3\ldots n}(\mathbf{r})$ and the cycle continues until the final electron density is consistent with the Hamiltonian. This process is called Self Consistent Field (SCF) approach [31].

2.2.1 Spin Density Functional Theory

For spin magnetic systems, the ground state spin density has a broken symmetry (imbalanced spin-up and spin-down electron spin densities, i.e. $\rho_\uparrow \neq \rho_\downarrow$) and thus their total energy and other ground state properties are described by a functional which depend on the magnetization density $m(\mathbf{r}) = \rho_\uparrow(\mathbf{r}) - \rho_\downarrow(\mathbf{r})$ as an additional field to the ordinary charge density.

Therefore for a spin polarised system, the total energy given in Equation 2.3 becomes a functional of both the ground state spin-up and spin-down densities:

$$E_T = E\left[\rho_0^{\uparrow}(\mathbf{r}), \rho_0^{\downarrow}(\mathbf{r})\right]. \tag{2.10}$$

This modifies the Kohn-Sham equations (Equation 2.7) to include an additional term, $\pm\mu_B B_{xc}(\mathbf{r})$ used to describe the ground state magnetization of the electron system, where $\mu_B = e\hbar/2mc$ is the Bohr-mageton and $\mathbf{B}_{xc}$ is the magnetic exchange field which an electron experiences. The modified Kohn-Sham equation for spin-polarised systems therefore becomes

$$\left[-\frac{\hbar^2}{2m}\Delta^2 + \int \frac{\rho(\mathbf{r})}{\mathbf{r}-\mathbf{r}'}d\mathbf{r}' + V_{ext}(\rho) + V_{xc}(\rho) - \mu_B B_{xc}(\mathbf{r})\right]\psi_i = H_{KS}\psi_i(\rho), \tag{2.11}$$

where the charge density defined by Equation (2.8) is decomposed into spin-up and spin-down densities corresponding to different sets of the Kohn-Sham orbitals:

$$\rho_{\uparrow}(\mathbf{r}) = \sum_i^{N/2} \left|\psi_i^{\uparrow}(\mathbf{r})\right|^2 \tag{2.12 a}$$

$$\rho_{\downarrow}(\mathbf{r}) = \sum_i^{N/2} \left|\psi_i^{\downarrow}(\mathbf{r})\right|^2 \tag{2.12 b}$$

Therefore the total energy of a spin-polarised system becomes a functional of the two spin-polarised charge densities. The total spin density due to spin polarization is given as $\mu(r) = \rho_{\uparrow}(\mathbf{r}) - \rho_{\downarrow}(\mathbf{r})$, from which the total magnetic moment (**M**) can be expressed as

$$\mathbf{M} = \int \left[\rho_{\uparrow}(\mathbf{r}) - \rho_{\downarrow}(\mathbf{r})\right] \mathrm{d}\mathbf{r}^3. \tag{2.13}$$

To calculate the properties of a spin-polarised many-body system thus needs a two dimensional spin space, which in turn requires a larger fraction of the Brillouin zone to be sampled. In practice, a spin polarized calculation proceeds separately for up and down spins and needs more computational resources to converge since both the normal charge density $(\rho_{\uparrow} + \rho_{\uparrow})$ and the spin charge density $(\rho_{\uparrow} - \rho_{\downarrow})$ have to converge separately.

Because of the additional degrees of freedom contained in the spin density, spin-polarised Kohn-Sham equations often have manifold metastable self consistent solutions corresponding to different spin polarisations. Determining which of these is the ground state, and if there are any solutions that have been missed, requires an exhaustive search which is computationally intensive [32]. This is because the energy differences between different metastable configurations are so small that SCF calculations starting near a metastable solution may tend to converge to it – leaving the very existence of other solutions to go unseen if all possible spin configurations are not carefully considered [33]. However, a constrained DFT technique, known as Fixed Spin Moment (FSM) [34], greatly simplifies the search for the true ground state magnetic ordering. When this approach is used, it is however necessary to confirm whether a particular spin state is the true local minimum by continuing the calculation using Unrestricted Spin Optimization (USO) techniques. In this Thesis, both approaches were followed by considering multiple initial spin states and geometry configurations to ensure that the true spin ground state was found, as well as all the other relevant metastable spin states.

The tendency towards a specific magnetic ordering state is determined by a balance between the kinetic energy and the exchange-correlation effects [32]. Whereas the parallel alignment of the electronic spins leads to a gain of exchange energy, it also causes a loss of kinetic energy which explains why most many-atomic solid state systems are usually non-magnetic. In solids, the gain in exchange energy is dominated by the loss in kinetic energy which arises from the delocalization of the valence electrons. Magnetism thus occurs only if these electrons are sufficiently localized as in the case of elemental ferromagnets Fe, Co and Ni [35].

2.2.2 Approximations to exchange-correlation potential

The Density Functional Theory is in principle an exact theory of many interacting body systems, but in practice, approximations are needed for the exchange-correlation potential V_{xc} since its exact functional form is not precisely known. The application of the Density Functional Theory approach therefore depends on the reliability and accuracy of the approximations used. Although more accurate forms of exchange-correlation potential have been developed, there is currently no known systematic way to achieve an arbitrary high level of accuracy [26]. The commonly used approximations to the exchange and correlation

potential are the Local Density Approximation (LDA) and Generalised Gradient Approximations (GGA).

In the LDA, the exchange-correlation energy of an electronic system is constructed by approximating the exchange correlation energy of the electrons at a local point within the electron gas to that of a homogeneous electron gas (since the exchange-correlation energy of a homogeneous electron gas is exactly known) that has the same density as the electron gas. Thus,

$$E_{xc}^{LDA}\left[\rho(\mathbf{r})\right]=\int \rho(\mathbf{r})\varepsilon_{xc}\left[\rho(\mathbf{r})\right]d\mathbf{r} \tag{2.14}$$

where $\varepsilon_{xc}(\rho)$ is the exchange correlation function of a homogeneous electron gas [31] which can be modified to include spin effects by treating the spin-up and spin-down electrons independently. This leads to the Local Spin Density Approximation (LSDA) where the charge density is taken as the sum of spin-up and spin-down electron densities.

The L(S)DA method assumes that the exchange-correlation energy is purely local and thus ignores corrections to the exchange-correlation energy at a point **r** due to nearby inhomogenities in the electron density. On the other hand, the GGA technique corrects this assumption by making the exchange-correlation contribution not only dependent on the local density, but also on the neighbouring density as well as the magnitude of its gradient, $|\nabla\rho|$ at each point. Therefore,

$$E_{xc}^{GGA}\left[\rho(\mathbf{r})\right]=\int \rho(\mathbf{r})\varepsilon_{xc}\left[\rho(\mathbf{r})\right]f_{xc}\left[\rho(\mathbf{r}),|\nabla\rho(\mathbf{r})|\right]d\mathbf{r} \tag{2.15}$$

where $f_{xc}(\rho,|\nabla\rho|)$ is a suitably chosen continuity enhancement factor dependent on the density of the electron gas as well as the magnitude of its gradient, which modifies the L(S)DA according to the variation of the density in the vicinity of the considered point. With an appropriate choice of the density function and the magnitude of its gradient, the GGA technique results in a consistent improvement of the exchange-correlation energy compared to the L(S)DA method [36,37].

2.2.3 Solving the Kohn-Sham equation

Solving the Kohn-Sham equation (Equations 2.7 and 2.11) for the ground state charge density requires solving an infinite set of one-electron equations with V_{xc} being the exchange-correlation operator in the L(S)DA or GGA approximation. One approach to constructing the Kohn-Sham single particle orbitals ψ_m (Equations 2.8 and 2.12) is to use a basis set in terms of which the electronic wave function can be expanded as a linear combination of these basis orbitals as

$$\psi_m(\mathbf{r}) = \sum_{P=1}^{P} c_p^m \varphi_p^b(\mathbf{r}) \tag{2.16}$$

where the wave function, ψ_m belongs to a function space with infinite dimension P and its solution depends on finding appropriate expansion coefficients c_p^m to express it in a given basis function set φ_p^b [31]. Given a choice of basis functions (e.g. plane waves [32]) and the fact that the total energy is variational, c_p^m becomes the only variables in the problem and the solution of the self consistent Kohn-Sham equations amounts to determining the expansion coefficients for the occupied orbitals that minimize the total energy. The most common approach to solving the self consistent Kohn-Sham equations requires optimization of c_p^m and determination of the self consistent charge density. The expansion coeficients c_p^m that solves the single particle Kohn-Sham equations for a fixed charge density are repeatedly determined to find the total energy of the system using standard matrix techniques, thus making the Schrödinger equation for the single particle Kohn-Sham equations a generalized eigenvalue problem which may be expressed as

$$\sum_{P=1}^{P} \left(\mathbf{H} - \varepsilon_i \mathbf{S} \right) c_p^m = 0 \tag{2.17}$$

where $\mathbf{H}$ and $\mathbf{S}$ are the energy-independent Hamiltonian and overlap matrices, respectively. This equation is solved at each **k**-point for integration in the irreducible wedge of the Brillouin zone (IBZ) sampled in three dimensional *k*-space as determined by the local point symmetry of a given structure. Practically, it may not be possible to express the true occupied Kohn-Sham orbitals exactly in terms of basis sets, but instead an approximate solution that is optimal (in the sense that it gives the lowest possible total energy) can be reached using by

using a basis set of sufficient quality and the SCF approach as explained in Section 2.2. The quality of a basis set can therefore be measured by the extent to which the total energy evaluated using the basis set orbitals differs from the true Kohn-Sham energy. In addition, a good basis set needs to be efficient, unbiased, mathematically simple and complete, which respectively, refers to the number of the basis functions needed to achieve a given level of convergence, whether or not the basis favours certain regions of space over others (and does not artificially favour a particular solution), the difficulty in calculating matrix elements and whether the basis can be improved arbitrarily by adding additional functions of the same type [32].

Any suitable complete basis set can be used to represent the Kohn-Sham orbitals and many choices are available. The most commonly used include Linear Combination of Atomic Orbitals (LCAO), Gaussians or Slater-Type-Orbitals (GTOs or STOs) and plane wave basis sets [38].

Using plane wave basis sets to represent Kohn-Sham orbitals offers a number of advantages compared to other basis sets [39]. These include the simplicity of the basis functions (which make no preconceptions regarding the form of the solution), the absence of basis set superposition error as well as the ability to efficiently calculate the forces on atoms. Also, Bloch's theorem makes plane waves the natural choice for the representation of electron orbitals in a periodic system. In addition, the fact that the kinetic energy operator is diagonal in reciprocal space whereas potential energy is diagonal in real space also favours use of plane wave representation since it easy to use Fast Fourier Transforms (FFT) in switching between these energy representations, which significantly reduces the computational cost [40]. Furthermore, as a plane wave basis set is non-local, no Pulay forces [41] will arise when calculating the forces on the ions in the system. Hence these ionic forces may be calculated with greater efficiency.

One principle disadvantage of a plane wave basis set is its inefficiency when used in a full potential calculation [32], since the number of basis functions needed to describe atomic wavefunctions accurately near the nucleus would be prohibitive. To overcome this limitation, pseudopotentials [22,26] or hybrid basis sets [32] are introduced to describe atomic wavefunctions with strongly varying potentials. Therefore, in practice, the plane wave approach for solving the Kohn-Sham equations are often carried out in two schemes: either as

a full potential or pseudopotential calculation, depending on whether the plane waves are used to treat the potential due to all electrons in an atom or only the valence electrons (including the semi core states).

2.2.3.1 Full potential plane wave methods

Full Potential Plane Wave (FP-PW) methods are among the most accurate schemes for solving the Kohn-Sham equations. They take into consideration all electrons of an atom, including the core electrons where the potential and wave functions are strongly varying, and therefore have the advantage that properties dependent on the behaviour of core electrons, such as the polarization of core electrons and hyperfine interactions, can be determined with high accuracy. However, full potential plane waves are relatively slow [32] to converge in the core region of the atom, and thus are usually augmented with some other atomic-like basis set functions in regions close to the atomic cores. In the region far removed from the nuclei, the electrons are freer and can be described by plane waves. Accordingly, the unit cell space is divided into non-overlapping spheres (called muffin-tin (MT) spheres) centred at atomic sites and an interstitial region between the spheres as illustrated in Figure 2.1.

2.2.3.1.1 Augmented Plane Wave method

The Augmented Plane Wave (APW) method calculates the energy which corresponds to the eigenvalue for each atomic orbital. This makes the basis functions to be explicitly energy

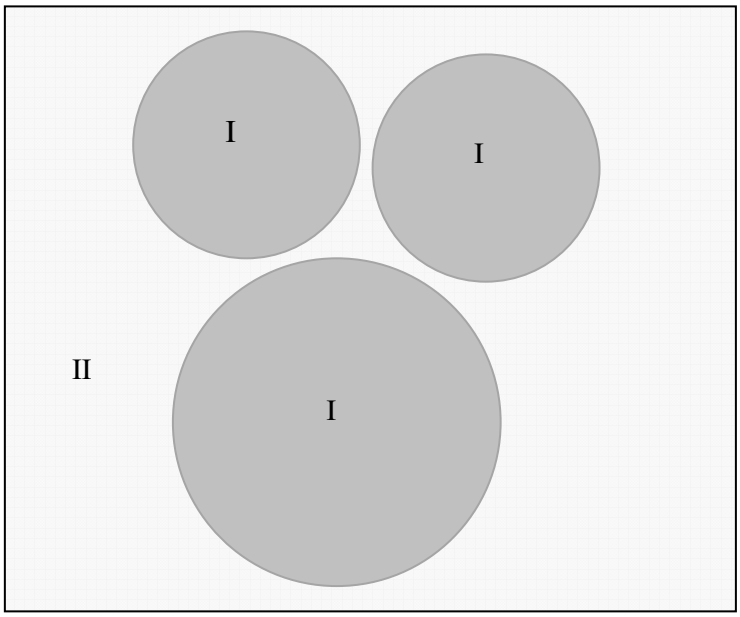

Figure 2.1: Partitioning of a unit cell space into Muffin-Tin spheres (I) and an interstitial region (II).

dependent, thus leading to a non-linear eigen-value problem. This energy dependence can be represented in the MT and the interstitial regions (Figure 2.1) as [32]

$$\varphi_{\mathbf{K}}^{\mathbf{k}}(\mathbf{r},E)=\begin{cases}\dfrac{1}{\sqrt{V}}e^{i(\mathbf{k}+\mathbf{K})\cdot\mathbf{r}} & r\in II\\ \sum_{l,m}A_{l,m}^{\alpha,\mathbf{k}+\mathbf{K}}u_l^{\alpha}(r',E)Y_m^l(r') & r'<R_{\alpha}\end{cases} \tag{2.18}$$

where V is the volume occupied by the MT spheres, $r'=r-R_{\alpha}$ is the position inside sphere α with polar coordinates r' and $\hat{r}$, and u_l^{α} is the solution of the radial Schrödinger equation for the atomic sphere α at an unknown energy E. $A_{l,m}^{\alpha,\mathbf{k}+\mathbf{K}}$ is an energy dimension parameter which is also unknown chosen so as to match (at the atomic sphere boundary) the atomic solution to each plane wave only in value, but not in slope. For a true atom, the boundary condition that $u_l^{\alpha}(r',E)$ should vanish for $r\to\infty$ limits the number of energies E for which a solution u_l^{α} can be found and thus act as efficient basis functions since they closely

resemble how the actual eigen-function will look like in that region of the unit cell crystal. Inside the MT spheres, the Kohn-Sham orbitals are only accurately described by the APW basis functions if the energy of the APW basis function is the same as the eigen-energy.

Hence the basis functions have explicit energy dependence, resulting in a non linear Eigen value problem (with energy dependence in the Hamiltonian and overlap matrices). Consequently, the eigenvalues have to be determined via an iterative procedure, with many trial energies, requiring a large number of matrix diagonalizations. This makes the APW method inherently slow and computationally expensive, making it suitable only in systems with few eigenvalues.

2.2.3.1.2 Linearized Augmented Plane Wave method

Unlike APW, Linearized Augmented Plane Wave (LAPW) method introduces linearization of energy dependence by solving the radial Schrödinger equation for a fixed linearization energy by adding the energy derivative of this function [32,42]. The basis functions, u_l in the MT spheres are supplemented by their energy derivatives $\dot{u}_l$ but both u_l and $\dot{u}_l$ are now evaluated at a fixed energy E_o. The original energy dependence of the radial basis function in the APW approach is thereby replaced by the Taylor expansion series:

$$u_l\left(r',E\right)=u_l\left(r',E_o\right)+\left(E-E_o\right)\dot{u}_l\left(r',E_o\right)+... \tag{2.19}$$

(terminated after the linear term [43]). The radial functions u_l and its energy derivative $\dot{u}_l$ are solutions of the Euler equations [44]:

$$H^{sph}u_l\left(E_l,r\right)=E_l u_l\left(E_l,r\right) \tag{2.20a}$$

and

$$H^{sph}\dot{u}_l\left(E_l,\mathbf{r}\right)=E_l\dot{u}_l\left(E_l,\mathbf{r}\right)+u\left(E_l,\mathbf{r}\right) \tag{2.20b}$$

where H^{sph} is the spherical Hamiltonian (containing only the $l=0$ of the effective potential within the muffin tin region) of the radial Schrödinger equation. Then, the explicit form of the linearized basis function, called LAPW, becomes:

$$\varphi_{\mathbf{K}}^{\mathbf{k}}\left(\mathbf{r},E\right)=\begin{cases}\dfrac{1}{\sqrt{V}}e^{i(\mathbf{k}+\mathbf{K})\cdot\mathbf{r}} & r\in II \\ \sum_{l,m}\left[A_{l,m}^{\alpha,\mathbf{k}+\mathbf{K}}u_l^{\alpha}\left(r',E_o\right)+B_{lm}^{\alpha,\mathbf{k}+\mathbf{K}}\dot{u}_l^{\alpha}\left(r',E_o\right)\right]Y_m^l\left(\hat{r}'\right) & r'<R_{\alpha}\end{cases} \tag{2.21}$$

where the coefficients $A_{l,m}^{\alpha,\mathbf{k}+\mathbf{K}}$ and $B_{lm}^{\alpha,\mathbf{k}+\mathbf{K}}$ are unknown energy dimension parameters chosen so as to match (at the atomic sphere boundary) the atomic solution to each plane wave both in value and slope.

2.2.3.1.3 Linearized Augmented Plane Wave Method + Local Orbitals

Linearization in the LAPW method introduces the problem that for a given l value only the states of one principal quantum number can be described. This is a limitation in the treatment of low lying valence states (also called semicore states). In order to treat these semicore states efficiently, another type of basis functions called Local Orbitals (LO), defined for a particular l and m in a particular atomic sphere, are added. Thus,

$$\varphi_{\alpha,LO}^{lm}\left(\mathbf{r}\right)=\begin{cases}0 & r\in II \\ \left[\begin{array}{l}A_{lm}^{\alpha,LO}u_l^{\alpha}\left(r',E_{1,l}^{\alpha,LO}\right)+B_{lm}^{\alpha,LO}\dot{u}_l^{\alpha}\left(r',E_{1,l}^{\alpha,LO}\right)\\ +C_{lm}^{\alpha,LO}u_l^{\alpha}\left(r',E_{2,l}^{\alpha,LO}\right)\end{array}\right]Y_m^l\left(\hat{r}'\right) & r'\le R_{\alpha}\end{cases} \tag{2.22}$$

where the coefficients $A_{lm}^{\alpha,LO}$, $B_{lm}^{\alpha,LO}$ and $C_{lm}^{\alpha,LO}$ are determined by normalization [32] together with the requirement that the LO and its slope must be equal to zero at the sphere boundary. This condition makes the plane waves continuous and smooth at the sphere boundary. The basis functions should completely be confined within the atomic spheres (i.e. do not leak out of the MT sphere) and in practice one has to select such functions for some physically relevant states of the system under consideration. Thus use of the LO slightly increases the matrix size of the linear eigen-value problem. However, they remarkably improve variational convergence and efficiently treat the semicore states. Since LOs are not connected to plane waves in the interstitial region, they have no **k** or **K** vector dependence and have non-vanishing amplitude within the MT sphere in their respective atoms.

2.2.3.1.4 Augmented Plane Wave + local orbitals

In Augmented Plane Wave + local orbitals (APW+lo) approach [44], the basis functions are independent of the energy of the corresponding eigen-value and has the same basis set size as in the APW method. This approach makes use of APWs with a fixed set of energies, but with an additional new local orbital (lo) so as to have enough variational flexibility of the radial basis functions. To avoid the non-linear eigen-value problem of the APW approach, each radial wave function in the MT sphere is determined at fixed linearization energy. But since fixed energies do not give a good description of the eigenfunctions, the basis set is augmented with a second type of basis functions called local orbitals (abbreviated as lo, different from the LO used in LAPW) given by

$$\varphi_{\alpha,lo}^{lm}(\mathbf{r}) = \begin{cases} 0 & r \in I \\ \left[A_{lm,lo}^{\alpha} u_l^{\alpha}\left(r', E_{1,l}^{\alpha}\right) + B_{lm,lo}^{\alpha} \dot{u}_l^{\alpha}\left(r', E_{1,l}^{\alpha}\right) \right] Y_m^l(\hat{\mathbf{r}}) & r \le R_{\alpha} \end{cases} \tag{2.23}$$

where the two coefficients $A_{lm,lo}^{\alpha}$ and $B_{lm,lo}^{\alpha}$ are determined by normalization and by the requirement that the local orbitals must have zero value and slope at the muffin tin boundary. This boundary condition makes the plane waves continuous, but not necessarily smooth, at the sphere boundary. Consequently, basis functions with kinks are introduced at the sphere boundary, thus making it necessary to include terms describing the MT surface in the kinetic energy part of the Hamiltonian. However, the additional variational freedom allows these basis sets to still accurately describe the wave function.

The APW+lo approach significantly reduces the basis set matrix and practically converges to the same results as LAPW within a shorter computational time [45]. However, it is sometimes advantageous [46] to use mixed LAPW and APW+lo or $\mathrm{APW}+\mathrm{lo}+\mathrm{LO}$ as implemented in the WIEN2k *ab initio* modelling code [46].

2.2.3.2 Pseudopotential plane wave methods

In contrast to the full potential methods discussed above, pseudopotential methods [22,26] are based on the fact that core states are not necessarily essential for the description of chemical bonding, and that a good description of the valence wave functions inside the core region is not strictly required since core states are highly localized and are not involved in chemical bonding. Therefore if the solution inside some cut-off radius between the core and valence region is replaced with a smooth wave function (called pseudo wave function), then there will be no loss of information in describing those properties of materials (e.g. chemical interaction) which are dependent on the valence electrons. However pseudopotential methods are inefficient in obtaining information that is inherently contained in the region near the nucleus (e.g. hyperfine fields and polarization at the core).

The pseudopotential approach replaces the rapidly varying core potential of an atom with an effective potential, called pseudopotential, which acts only on the valence electrons outside a selected core radius (Figure 2.2). This allows the electronic wave function to be expanded using a much smaller number of plane wave basis sets, thus making computation much faster compared to full potential plane wave methods.

Although full potential methods have superior accuracy, pseudopotential techniques have become increasingly popular and have been found to maintain good accuracy for a wide variety of materials, including magnetic systems [47]. The results reported in this Thesis have been obtained using *ab initio* DFT pseudopotential methods, with selected cases also repeated using full potential methods to confirm the reliability of the results.

The pseudopotential valence wave function χ_v is constructed by combining the core φ_c and the true valence φ_v real wave functions as follows:

$$|\chi_v\rangle = |\varphi_v\rangle + \sum_c \alpha_{cv} |\varphi_c\rangle \tag{2.24}$$

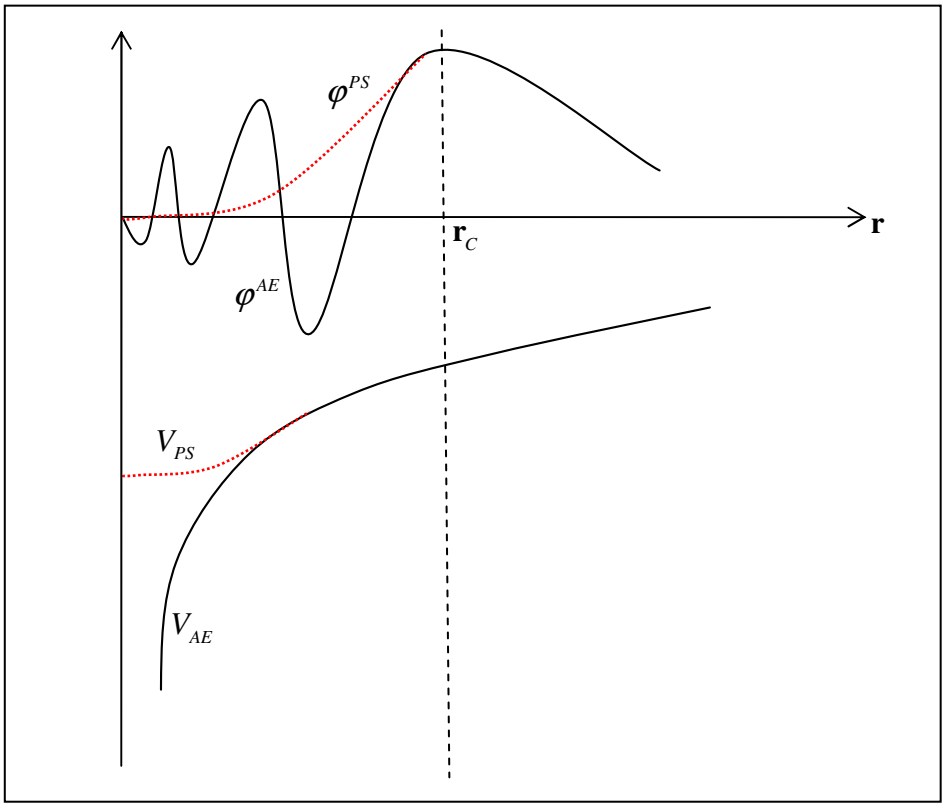

Figure 2.2: Schematic illustration of the replacement of the all-electron wave function $\varphi^{AE}(\mathbf{r})$ and core potential $V_{AE}(\mathbf{r})$ by a pseudo-wave function $\varphi^{PS}(\mathbf{r})$ and pseudopotential $V_{PS}(\mathbf{r})$, respectively. For $r > r_c$, the pseudo-wave function and the pseudopotential are identical to the real wave function and real potential, respectively (adapted from reference [32]).

where $\alpha_{cv} = \langle \varphi_c | \chi_v \rangle \neq 0$ is the real wave function of the core states. This pseudo wave function satisfies the Schrödinger equation, from which the modified pseudo-Hamiltonian can be written as

$$H_{PS} = H + \sum_c (\varepsilon_v + \varepsilon_c) |\varphi_c\rangle\langle\varphi_v| \tag{2.25}$$

where H is the original Hamiltonian. H_{PS} has the same eigenvalues as the original Hamiltonian but a smoother, nodeless wave function. The associated potential is called a pseudopotential and is given by

$$V_{PS} = V + \sum_c (\varepsilon_v + \varepsilon_c) |\varphi_c\rangle\langle\varphi_v| \tag{2.26}$$

where $V = (Z_c/r)\hat{I}$ ($\hat{I}$ is the identity operator) is the bare nuclear potential.

The most general form of V_{PS} is

$$V_{PS} = \sum |lm\rangle V_l \langle lm| \tag{2.27}$$

where $\langle lm| = Y(\theta,\phi)$ are spherical harmonics and V_l is the pseudopotential corresponding to a given angular momentum *l*.

An important consideration in the generation of a pseudopotential for a particular element is the number of plane waves required for its accurate representation. A pseudopotential is regarded as *soft* when few Fourier components are required (or *hard* otherwise). Another crucial property of pseudopotential applications is *transferability*, i.e. a pseudopotential constructed for a particular atom in some specific chemical or structural environment should be used reliably for the same atomic species in different environments [48] (e.g. semi-conductor, metal, molecule, surface, etc.).

In order to improve transferability of a pseudopotential, the core radius should be small, and for it to be soft, the core radius needs to be large. These two competing criteria must be optimized in order to produce a pseudopotential that is both accurate and as soft as possible. In addition, the valence charge density associated with chemical bonds should be reproducible. How the total charge inside and outside the core is matched with that of the all-electron wave function leads to the different types of pseudopotentials, which include norm conserving and ultrasoft pseudopotentials.

2.2.3.2.1 Norm Conserving Pseudopotentials

In Norm Conserving Pseudopotentials [25], the total pseudocharge inside the core is required to match that of the all-electron wave function so as to satisfy the condition of orthogonality [22].This requirement is called norm-conservation and it guarantees that the pseudopotential is useful, not only in every energy range, but also in all environments such that its eigenvalues do not depart significantly from those used in its construction [22].

In order to improve transferability, the core radius should be small, but not smaller than the position of the outermost node of the all-electron wave function (so as to guarantee a nodeless wave function). This conflicting effect of r_c creates a trade-off between accuracy and efficiency while retaining reasonable transferability.

The following general criteria are used for the construction of norm-conserving pseudopotentials [22]:

1. For a chosen configuration of the atom, the eigenvalues of the all electron wave function should be identical to those of the pseudo-wave function.
2. The radial pseudo-valence wave functions should be nodeless and should be identical to the radial all-electron wave function outside the cut-off radius.
3. The total charge density inside the region $r < r_c$ should be equal for both the all-electron R_{AE} and pseudo-wave functions R_{PS} (norm conservation condition):

$$\int_0^{r_c} \left| rR_{PS}(r) \right|^2 dr = \int_0^{r_c} \left| rR_{AE}(r) \right|^2 dr \tag{2.28}$$

4. For $r \geq r_c$, the normalized radial pseudo wave function must equal the normalized all-electron wave function.

Norm conserving pseudopotentials are generally hard and require a large number of plane waves to converge, hence they are computationally expensive. In practice, it is therefore necessary to impose other conditions which can reduce the number of plane waves as it is the main factor which determines the energy cut-off in the expansion of wave functions in a basis set of plane wave, and consequently the computational cost of the calculation.

Although the pseudo wave functions in all pseudopotential methods are expected to be as smooth and accurate as possible, norm conserving pseudopotentials achieve accuracy at some sacrifice of smoothness. For 3*d* transition elements, and in many other important magnetic systems [49], constructing a pseudo-wave-function which is smoother than the all-electron one is not easy and requires a large number of plane wave basis sets to converge. However, these difficulties [50,51] have been compensated to some extent by the development of iterative techniques which are capable of handling large plane-wave basis sets. Such methods are most efficient if the non-local part of the pseudopotential can be recast in a separable form, either by expanding the semi-local potential approximately as a sum of separable terms [25] or by generating a fully nonlocal separable pseudopotential based on a given semi-local pseudopotential [52].

2.2.3.2.2 Ultrasoft Pseudopotentials

Ultrasoft Pseudopotentials (USP) [53] relax the norm conservation condition of norm conserving pseudopotentials by a transformation which re-expresses the problem in terms of a smooth function and an auxiliary function around each ion core. This approach allows calculations to be performed with the lowest possible cut-off energy for the expansion of the plane wave basis set, thus improving transferability while holding the cut-off radius fixed (even for a large cut-off radius).

The total energy in the USP approach is similar that in norm conserving pseudopotentail plane wave methods, but with the nonlocal ultrasoft potential expressed as

$$V_{US} = \sum_{i,j} D_{i,j} \left| \gamma_i^{lm} \right\rangle \left\langle \gamma_j^{lm} \right| \tag{2.29}$$

where γ and D are characteristic parameters of the potential used and differ for different l and m. The ultrasoft potential V_{US} consists of the generalised separable norm conserving pseudopotential and a term which vanishes only if the generalized norm conservation condition is enforced [22]. By relaxing the norm conservation constraint, all the wave functions at different reference energies can be replaced independently by pseudo wave functions by requiring the matching of the logarithmic derivatives at the cut-off radius (thus, practically, the cut-off radius can be chosen quite large, well beyond the maximum of the radial wave function, resulting in smooth wave functions). This condition means that the pseudo and the all-electron wave functions become identical beyond the cut-off radius (Figure 2.2), but the charge density enclosed in the pseudized region is still different and can be expressed as

$$\rho(\mathbf{r}) = \sum_i \left| \varphi_i(\mathbf{r}) \right|^2 + \sum_i \sum_{n,m,j} Q_{nm}(\mathbf{r}) \left\langle \varphi_i \left| \gamma_n^i \right\rangle \right\langle \gamma_m^i \left| \varphi_i \right\rangle * \tag{2.30}$$

where φ_i are the wave functions of the i occupied states and $Q_{nm}(\mathbf{r})$ are the augmentation functions that are strictly localized in the core regions. Integrating this charge density and introducing a generalized orthonormality condition gives

$$\left\langle \varphi_i \left| \hat{S} \right| \varphi_j \right\rangle = \delta_{ij} \tag{2.31}$$

where $\hat{S}$ is a Hermitian overlap operator given by

$$\hat{S} = 1 + \sum_{n,m,j} \left[\int Q(\mathbf{r}) dr \right] |\gamma_n\rangle \langle \gamma_m|. \tag{2.32}$$

The charge density given by Equation (2.30) integrates to a number of valence electrons in the system, and the local potential includes the usual Hartree and exchange-correlation contributions:

$$V_{LOC}[\rho(\mathbf{r})] = V_{PS}(\mathbf{r}) + V_H[\rho(\mathbf{r})] + V_{xc}[\rho(\mathbf{r})]. \tag{2.33}$$

The overlap operator $\hat{S}$ is non-local; therefore there is a contribution from the Hartree and exchange-correlation potentials to the non-local part of the potential. Hence, the non-local contribution also depend self consistently on the charge density, adjusting itself to changes in the charge configuration due to the environment. This feature improves transferability of ultrasoft pseudopotentials over norm conserving pseudopotentials.

The Kohn-Sham self consistent equations for the USP then become a generalized eigen-value problem

$$\left(H - \varepsilon_i \hat{S}\right) |\phi_i\rangle = 0 \tag{2.34}$$

whose solutions are the pseudo-wave functions ϕ_i for each reference atomic state *i*, and *H* can be presented as a sum of the kinetic and local potential as

$$H = T + V_{PS}(\mathbf{r}) + V_H[\rho(\mathbf{r})] + V_{xc}[\rho(\mathbf{r})]. \tag{2.35}$$

Like in the norm conserving pseudopotentials, an all-electron calculation is carried out on a free atom when generating ultrasoft pseudopotentials, leading to a screened atomic potential. The following general criteria are followed when constructing ultrasoft pseudopotentials [22].

1. The pseudo eigenvalues should be equal to the all-electron eigenvalues, and the corresponding orbitals should match exactly outside the core radii.
2. The scattering properties should be correct at each reference energy. Thus, the transferability can systematically be improved by increasing the number of such energies.
3. The valence charge density should be precisely equal to the all-electron valence density in the reference configuration.

2.2.4 Non-Linear core corrections in pseudopotential approximations

Pseudopotential approximations in general assume that the core and valence charge densities are well separated such that the kinetic and exchange-correlation interactions can be approximated to be linear. However, this approximation may lead to systematic errors in the total energy if there is a significant overlap between the two densities. In particular, spin-polarised calculations introduce additional non-linearity which necessitates an explicit consideration of the non-linear dependence of the energy on the core charge density. In addition, spin-polarisation in magnetic systems, including transition elements, originate from valence electron orbitals whose charge and spin density amplitudes overlap with those of the core electrons [45]. Accordingly, it is important to describe the behaviour of such wave functions near the core region as accurately as possible such that the dependence of the core wave functions on the surrounding environment is taken care of in determining the exchange correlation potential seen by the valence electrons.

Within the pseudopotential approximation, the total exchange-correlation potential is a function of both the valence and core charge densities, together with the spin polarisation [54]. This can be written implicitly as

$$V_{xc}(\rho^v + \rho^c, p) = \underbrace{\left[V_{xc}(\rho^v + \rho^c, p) - V_{xc}(\rho^v, p^v)\right]}_{\text{included in the pseudopotential}} + \underbrace{V_{xc}(\rho^v, p^v)}_{\text{calculated}} \tag{2.36}$$

where

$$p(\mathbf{r}) = \frac{\rho^v_{\uparrow}(\mathbf{r}) - \rho^v_{\downarrow}(\mathbf{r})}{\rho^v(\mathbf{r}) + \rho^c(\mathbf{r})} \tag{2.37}$$

is the spin-polarisation and ρ^v and ρ^c are the valence and core charge densities, respectively. The dependence of the exchange correlation potential on spin polarisation also makes it a non linear function of the charge density, thus making the ionic pseudopotential dependent on the valence configuration in spin polarised systems. Therefore, nonlinear–core correction to the exchange and correlation interaction potential is essential in the determination of the magnetic ordering properties of spin-polarised systems [45,55,56], such as the ones being modelled in the current study.

2.2.5 Accuracy and reliability of DFT methods

The accuracy and reliability of DFT methods such as those discussed above are mainly determined by the choice of the exchange-correlation functional, whose exact form is unknown.

In addition, computational errors arise from inaccurate representation of the wave functions (and energy) if insufficient number of plane wave basis sets are used in practical computations (usually due to computational cost) [57,58]. Despite these shortcomings, the density functional theory, in principle, is highly accurate and is capable of predicting many electronic and structural properties of solid state and other material systems with good accuracy, in comparison with experimental data. The level of accuracy achieved by these methods depends mainly on the property of interest and, also on other related properties of the material [58]. However, quantitative discrepancies between DFT and experimental results in most cases follow similar trends among different material systems [59,60] and therefore systematic errors for a particular DFT technique can easily be corrected from experience and comparison with experiment. For example, the formation energies of defects involve comparison of similar configurations by keeping the number of atoms and the charge state constant, hence systematic errors due (and DFT approximations) can approximately cancel out [61].

Other than the inherent limitations of the DFT approach, additional sources of errors encountered in calculations are usually due to numerical computations which arise mainly from the choice of the supercell size, the plane wave energy cut-off and *k*-point sampling. The magnitude of the error arising from each of these variables in the current study has been minimized by increasing their level of convergence. Converged calculations have been found to systematically fall within 1.0×10^{-4} eV for differences in total energies and 1.0×10^{-3} Å for structural properties. This accuracy is crucial in magnetic systems, since different magnetic states are often separated by energies in the order of meV, and therefore their corresponding quantum mechanical total energies should be sufficiently converged in order to reliably extract such small energy differences.

2.3 Geometry optimization

Geometry optimization in modelling of material systems allows refinement of an initial geometry and other physical parameters (e.g. lattice constants) so as to obtain the total energy corresponding to a stable state of the system. First, the electronic properties are calculated for a specific fixed geometry. The forces acting on the atoms are then calculated and the positions of the atoms are updated. To find the optimal positions and geometry of the atoms, the cycle is repeated until the total forces acting on individual atoms and the change in total energy between the steps fall below some user-predefined convergence tolerance limit. Structural optimization therefore ensures an accurate description of the system's electronic structure, including all other properties dependent on the total energy of the system. However, only a local minimum of the system, rather than its global minimum, may be reached during a geometry optimization process. The type of minimum reached depends greatly on the initial geometry used, amongst other factors. It is therefore important to use as many relevant initial configuration geometries as possible to ensure that the global minimum of the system is reached [23].

Structural optimization methods generally treat the atomic nuclei in a classical manner, but the energy and forces between them are calculated using quantum mechanical approximations. Many of these approximations are based on the principle of finding the minimum of an energy hypersurface as a function of its geometrical configuration (or atomic position) [23]. Other geometry optimization approximations optimize the total forces acting on a system of atoms using the damped classical Newtonian mechanics approach [41,46], as discussed in the following Section.

2.3.1 Quasi-Newtonian geometry optimization

Quasi Newtonian geometry optimization algorithms employ a quadratic model of the potential energy surface to converge to an energy minimum corresponding to a given structural configuration. The predicted potential energy hypersurface, E' and force $\mathbf{f}$ for a given geometry optimization step $\mathbf{s}$ is given by

$$E' = E - \mathbf{f}^T\mathbf{s} + \frac{1}{2}\mathbf{s}^T\mathbf{H}\mathbf{s} \tag{2.38}$$

and

$$\mathbf{f' = f - Hs} \tag{2.39}$$

respectively, where $\boldsymbol{H}$ is the approximate Hessian (matrix of second energy derivatives, or force constants with respect to geometry).

From equation (2.38), the forces become zero at the energy minimum (or any other stationary point in the energy hypersurface), from which the next step towards the global minimum can be obtained equation (2.39) [41]. Algorithms which employ this approach calculate an approximation to the Hessian (or its inverse) from various gradient approximations (for example, conjugate gradient methods which use information about the previous step to update the Hessian) either by directly computing it or by creating an estimate of it that improves as the calculation proceeds. Among the most successful Hessian update approaches is the BFGS (Broyden–Flecher–Goldfarb–Shanno) [62-65] and has been used in all calculations reported in this Thesis as implemented in the WIEN2k [46] and the CASTEP [41] materials computation codes.

In the BFGS approach, the Hessian matrix for the next geometry optimization step is updated as

$$\mathbf{H}_{k+1} = \mathbf{H}_k + \Delta\mathbf{H}_k \tag{2.40}$$

and for any two consecutive iterations, $\Delta\mathbf{H}_k$ is given by

$$\Delta\mathbf{H}_k = \left[\frac{a_k a_k^T}{s_k^T a_k} + \frac{\mathbf{H}_k \mathbf{s}_k s_k^T \mathbf{H}_k}{s_k^T \mathbf{H}_k \mathbf{s}_k} \right] \tag{2.41}$$

where $a_k = \mathbf{f_k} - \mathbf{f_{k+1}}$ is determined from the gradients of the two consecutive geometries. The commonly used method to determine the best step size $\mathbf{s}_k$ (and its direction) employs a quadratic model trust-region algorithm [66] with an additional constraint that $\mathbf{s}_{k+1} \leq R$ (where R is the trust region radius). The choice of the initial Hessian determines how long the geometry minimization process will take. For most algorithms, the first estimate of the Hessian is a unitary matrix which changes significantly in the course of the minimization. The BFGS update in most cases will tend to correct itself rather quickly within the first few steps compared to other approaches [66].

2.4 Formation energy

The formation energy of a defect in a semiconductor crystal provides information on its energetic stability, as well as on the relative stabilities between different configurations and charge states in which it is likey to occur. In addition, differences in formation energies of the defect provide an estimate of defect ionization energy levels within the host material's band gap, thereby giving an indication on the nature of the defect's electrical activity.

The most common technique used for performing formation energy calculations on an impurity defect within the DFT technique is the use of an enlarged unit cell, called a supercell [67] (which becomes the new unit cell of the system), in which the defect center is surrounded by a finite number of non-impurity atoms of the host. The success of this technique in predicting the structures of defects, their formation energies and other properties of material systems is well proven [68-71]. A major advantage of this approach is that the band structure and other properties of the defect-containing supercell can easily be compared with that of a similar supercell of the pure semiconductor host. Thus, changes induced by the presence of the impurity defect can be determined more accurately than in cluster methods, which often suffer from spurious quantum confinement effects as well as surface termination and defect-surface interaction effects that may introduce extra bands in the band gap [72]. Although interactions between the defect and its periodic images in the supercell approach may occur, their effect can be minimized if the size supercell is large enough.

2.4.1 Formation energy of a transition metal impurity in diamond

In this Section, the computational methodologies adapted for calculating the formation energies of 3*d* transition metal defects in diamond are discussed. Particular attention is given to those computational aspects which were used for calculating the formation energies and charge transition levels of isolated transition metal defects in a diamond supercell.

The formation energy E_f of a transition metal (TM) impurity in a particular charge state q in a diamond supercell is given by

$$E_f[TM]^q = E_T[n_C, n_{TM}]^q - E_T[n_C] - n_{TM}(\mu_{TM}) + q(\varepsilon_F - \varepsilon_V) \tag{2.42}$$

where $E_T[n_C, n_{TM}]^q$ is the total energy of the diamond supercell in charge state q containing

n_C carbon atoms and n_{TM} transition metal atoms, while $E_T[n_C]^q$ is the total energy of an equivalent pure diamond supercell; μ_{TM} is the corresponding chemical potential of the transition metal impurity and ε_F is the Fermi energy measured relative to the valence band maximum ε_V in the bulk. For elemental host semiconductor crystals like diamond, the chemical potential of a transition metal is equivalent to the energy per an atom in its respective crystal structure phase [73].

The formation energy calculated using this method in principle ignores contributions from vibrational entropy and pV contributions to Gibbs' free energy per particle since it is calculated at zero point temperature in the DFT approach. Explicit calculations of free energy entropy contributions are computationally demanding but they are generally assumed to be small enough not to affect qualitative conclusions. For instance, experimental and theoretical results for entropies of point defects have shown that entropy values are typically in the range of $0 - 10k$ [72] (where k is the Boltzmann constant), and approximately cancel out when comparing structures with and without defects [61]. The pV contribution to the Gibbs free energy per particle in solids can also be assumed to be negligible at reasonable pressures, and the electronic specific heat is so small that the temperature dependence of the electronic contribution can also be neglected [61].

In the neutral charge state, the formation energy of a transition metal impurity in diamond is independent of the electron chemical potential which defines the Fermi level of the electron reservoir [74], and can therefore be obtained directly from Equation (2.42) as:

$$E_f[TM]^0 = E_T[n_C, n_{TM}]^0 - E_T[n_C]^0 - n_{TM}\left(\mu_{TM}\right). \tag{2.43}$$

However, calculating the formation energy of charged defects requires knowledge of the electronic chemical potential which is not straightforward to compute. An approach which has been used in this Thesis is to compute the formation energy of transition metal impurities in diamond for different charge states relative to the neutral charge state. This method enables determination of the charge transition levels (i.e. donor/acceptor levels) within the diamond band gap, from which the relative stability of the respective charge states can be obtained with good accuracy.

From equation (2.42), the formation energy difference between any charge state q and the neutral charge state can be written as

$$E_f^{\pm q} - E_f^0 = E_T[D]^{\pm q} - E_T[D]^0 + q(\varepsilon_F + \varepsilon_V) \tag{2.44}$$

where $E_T[D]$ is the total energy of the supercell containing the transition metal impurity in a particular charge state q.

The maximum of the valence band energy ε_V corresponds to the negative of the first ionization potential (IP) [75,76] which, for a pure diamond supercell can be expressed as

$$\varepsilon_v = -(IP) = E_T\left[X\right]^0 - E_T\left[X\right]^{+1} \tag{2.45}$$

where $E_T\left[X\right]^{+1}$ is the total energy of the perfect supercell in the positive charge state and $E_T\left[X\right]^0$ is the total energy of an equivalent supercell in the neutral chare state. Substituting Equation (2.45) into Equation (2.44) for $q = +1$ gives

$$E_f^{+1} = E_f^0 + \left\{\left(E_T[D]^{+1} - E_T[D]^0\right) - \left(E_T[X]^{+1} - E_T[X]^0\right)\right\} + \varepsilon_F \tag{2.46}$$

which is the formation energy of a transition metal impurity in single positive charge state relative to the neutral charge state in the diamond supercell. Similarly, it can be shown that the formation energy for the double positive charge state relative to the neutral charge state is given by

$$E_f^{+2} = E_f^0 + \left\{\left(E_T[D]^{+2} - E_T[D]^0\right) - 2\left(E_T[X]^{+} - E_T[X]^0\right)\right\} + 2\varepsilon_F. \tag{2.47}$$

In the negative charge states, the inherent problem of band gap underestimation by the density functional theory leads to an underestimation of the calculated formation energy differences. An approach which has been used in this Thesis to correct this error is by making use of the experimental band gap of diamond (E_g = 5.49 eV) instead of the calculated value. Though not conclusive, this approach has previously been found to give results consistent with experimental values for a wide range of defects in semiconductor systems [76]. An alternative approach is to use Slater's transition state idea [77] in which the total energy difference between the different charge states is evaluated by the Kohn-Sham eigenvalues

with partial occupation. However, this treatment does not circumvent the band gap problem either, and we believe that substituting the theoretical band gap value with the experimental value is the best and practical approach at present. By using the theoretical band gap, we find that the formation energy for the negative charge states shift downwards by ~0.7 eV relative to those of the neutral charge states, but it should be noted that differences in formation energies between various (negative) charge states of a defect remains little affected due to cancellation of errors.

By definition, the band gap energy is the difference between the first ionization potential (Equation 2.45) and the Electron Affinity (EA):

$$EA = E_T[X]^- - E_T[X]^0 \tag{2.48}$$

where $E_T[X]^-$ is the total energy of the perfect supercell in the single negative charge state. Therefore,

$$E_g = IP - EA = \left(E_T[X]^0 - E_T[X]^-\right) - \varepsilon_V \tag{2.49}$$

or

$$E_g = \left(E_T[X]^{+1} - E_T[X]^0\right) - \left(E_T[X]^- - E_T[X]^0\right) \tag{2.50}$$

from which the theoretical band gap of diamond has been calculated to be 4.81 eV using the GGA approximation, which is in reasonable agreement with the experimental value of 5.49 eV, considering that DFT calculations are known to underestimate band gaps [26].

From Equations (2.44), (2.49) and (2.50), it can be shown that the formation energies of a transition metal impurity in the single negative and double negative charge states relative to the neutral charge state in the diamond supercell are, respectively, given by

$$E_f^{-1} = E_f^0 + \left\{\left(E_T[D]^- - E_T[X]^{-1}\right) - \left(E_T[D]^0 - E_T[X]^0\right) + \varepsilon_g\right\} - \varepsilon_F \tag{2.51}$$

and

$$E_f^{-2} = E_f^0 + \left\{\left(E_T[D]^{2-} - E_T[D]^-\right) - 2\left(E_T[X]^- - E_T[X]^0\right) + 2\varepsilon_g\right\} - 2\varepsilon_F. \tag{2.52}$$

It is important to note that the formation energies calculated from Equations (2.46), (2.47), (2.51) and (2.52) are obtained as functions of the Fermi energy, with the Fermi level referenced to the valence band maximum in the bulk (i.e. electrons are exchanged with the Fermi level such that $\varepsilon_F = 0$ at the top of the valence band in bulk diamond).

2.4.2 Charge transition levels

The position of the Fermi level where the formation energies of two charge states are equal, i.e. where the most stable state of a defect undergoes a transition from one charge state to another, is called thermodynamic transition level or ionization level, written as $\varepsilon_F(q_1/q_2)$, where q_1 and q_2 are the two charge states under consideration.

From Equations (2.46), (2.47), (2.51) and (2.52), it can be shown that the formation energy of a transition metal impurity in diamond for a particular charge state constitutes a sum of a constant quantum mechanical calculated energy corresponding to its respective formation energy at the valence band maximum, and a variable energy which is a function of the charge state and Fermi level. This relation can be written explicitly as

$$E_f(q, \varepsilon_F) = E_f^q\Big|_{\varepsilon_v} + q\varepsilon_F \tag{2.53}$$

from which the thermodynamic charge transition levels can be obtained by calculating the Fermi energy such that $E_f(q_1) = E_f(q_2)$. Equation (2.53) highlights the fact that a graph of the formation energy as a function of the position of the Fermi level will be a straight line graph whose slope is equal to the charge state under consideration, and the formation energy intercept is determined by the (quantum mechanical) total energy of the defect in that charge state. The thermodynamic transition levels therefore correspond to positions of the Fermi level where formation energy graphs of different charges (slopes) intersect.

For a given range of possible charge states in which a transition metal impurity may exist in diamond, many thermodynamic transitions could occur but the important ones are those which correspond to the most stable charge states with change in the position of the Fermi level. To obtain the most stable charge states, the atomic structure corresponding to each charge state should be relaxed to its equilibrium configuration. This is important since the atomic configuration of the transition metal ion may vary for different charge states and

lattice sites due to the different local electric potential associated with each charge or defect site. It is this difference in relaxation that leads to differences between thermodynamic versus optical transitions observed for a particular defect. In addition, each charge state may possess a different spin configuration of the defect impurity; with some having magnetic spin ground states while others not.

Experimentally, the most stable transitions would be observed where the final charge state can fully relax to its equilibrium configuration [72]. This type of level is therefore what could be observed in deep-level transient spectroscopy (DLTS) experiments for the case of deep centres[*], or corresponds to thermal ionization energy as derived from an analysis of temperature-dependent Hall-effect data in the case of shallow centres[†]. In cases where the final charge state cannot relax to its equilibrium configuration after undergoing a transition, an optical transition will be observed and this would correspond to an emission spectrum peak, for example in photoluminescence experiments.

However, comparison of calculated levels with experimentally observed levels needs to be carried out with caution due to the band gap problem and other inherent approximations in DFT calculations [78]. In particular, modelling of a periodic array of charged defects leads to errors in the calculated total energies due to electrostatic interaction of the defect and its periodic images in the supercell. These interactions represent a component in the calculated total energy that is purely an artefact of the supercell approach, shifting the total energy of the system relative to that of the neutral charge state, and thereby introducing a systematic error in the ionization energy. The methods which have previously been adopted to estimate and correct these errors, as well as other multi-polar terms present (even for neutral systems), have led to considerable debate [79-86], and there is no clear consensus on their accuracy as some of these "corrections" have been found to amount to a significant portion of the total band gap [72,84,87]. However, using large supercells has been found [79,88] to minimize interactions between charged defects and their periodic images. The thermodynamic transition levels reported in this Thesis have been obtained using a relatively large 64-atom diamond supercell containing one transition metal impurity at various lattice sites without

[*] An impurity defect level in a semiconductor material is defined as deep level if its energy state from the nearest band edge is much more than the average room temperature thermal energy (kT).

[†] An impurity defect level in a semiconductor material is termed as shallow if it is produced closer to the band gap edges at a depth on the order of the average room temperature thermal energy (kT) or less.

additional corrections, and therefore their location within the band gap may be used as an indication of the potential for a transition metal defect to yield deep donor or acceptor levels in diamond, as will be discussed in Chapter four.

2.4.3 Defect stability

The likelihood of an impurity in a given electronic charge state to form at a particular temperature depends on its formation energy. Therefore transition metal impurities with higher formation energies are less likely to form in diamond compared to those with lower formation energies (since a significant amount of energy needs to be expended in their creation). Quantitatively, this can be expressed in terms of the relative defect concentration (C) between two or more possible competing defect sites through a Boltzmann relation:

$$C = \frac{N_s}{N_c} \exp\left(-E_f / K_B T\right) \tag{2.54}$$

where N_s is the number of possible defect sites per unit volume in the crystal lattice in which the defect can be incorporated and N_c is the number of equivalent configurations in which the defect can be incorporated [72]. While this expression is only valid in equilibrium conditions, the formation energy is still informative even when defects are created in non equilibrium processes [8], such as ion implantation. Particularly, the magnitude of the formation energy provides an indication of which defects are likely to form and their relative proportions. Therefore, the relative defect concentration between two (or more) competing defect site configurations at a particular temperature is a function of their formation energies, and can be expressed as

$$\frac{C^a}{C^b} = \frac{N_s^a}{N_s^b} \exp\left(E_f^b - E_f^a\right) \tag{2.55}$$

where N_s^a and N_s^b are the number of possible defect configuration sites, a and b respectively. Thus the formation energies for the respective 3d transition metal impurities in diamond reported in this Thesis gives an indication of which transition metals may be most stable when incorporated into diamond at equilibrium conditions.

2.5 Computational methodology

The results reported in this Thesis have been performed using *ab initio* plane wave pseudopotential DFT methods for isolated 3*d* transition metals in diamond at the substitutional, divacancy and interstitial lattice sites. Calculations of formation energies and structural properties were carried out using a 64-atom diamond supercell constructed from $2 \times 2 \times 2$ conventional fcc diamond unit cells with an optimized lattice constant of a_0 = 3.569 Å (resulting in defect-image separation distance of $2a_0$), which is in close agreement with the experimental value of 3.567 Å [6]. To calculate magnetic interactions, larger 128-atom diamond supercells containing two transition metal impurities were used as will be discussed in Section 2.5.3. It should be noted that defect-image interactions become negligible, in principle, only in an infinitely large supercell limit (equivalent to the limit of an isolated defect). However, considering the computational cost associated with large supercell sizes, it has previously been shown that diamond supercell sizes of about 64 atoms [88] are relatively large enough for the periodic array of defects in the image supercells to have any significant contribution.

2.5.1 Structural configuration and optimization

Figure 3.1 shows models of an isolated transition metal impurity in a diamond lattice at the substitutional, divacancy and interstitial lattice sites as was used in the this study. In order to determine the most stable geometry corresponding to the total structural energy, full geometry optimization was performed without any symmetry or spin restrictions, with the transition metal atom (in different charge states: $q = +2, +1, 0, -1, -2$) placed at the various lattice sites. To ensure that the final symmetries were not dependent on the initial geometries, the transition metal (TM) impurity atoms were shifted away from high symmetry sites [23] in the initial geometries. For each geometry and charge state, various initial random positions and spins of the TM atom were considered in order to determine the most stable geometry and spin configurations corresponding to the lowest structural total energy. This treatment is necessary in magnetic calculations because spin-polarised Kohn-Sham equations often have manifold metastable self consistent solutions corresponding to different spin polarisations. Therefore, performing spin optimization by starting off at different initial solutions ascertains that a global energy minimum of the system, rather than a local minimum, is reached. An alternative method is to use the constrained spin moment

technique[‡] [32], but this approach is computationally intensive, since it requires further confirmation that a particular spin state obtained is the true minimum by continuing the calculation using unconstrained spin optimization. In addition, the constrained spin moment technique is limited by its inability to determine the type of magnetic ground state of a particular defect centre (i.e. whether it is ferromagnetic, ferrimagnetic, antiferromagnetic or non-magnetic). For this reason, the constrained spin moment technique was only used in selected cases to confirm the existence and stability limits of the magnetic states as calculated by spin optimization.

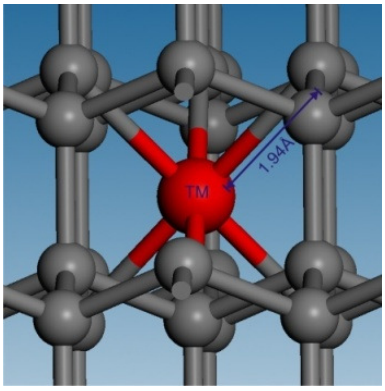

(a) Divacancy site: The transition metal atom occupies a midpoint between two missing carbon atoms. The ideal site has D_{3d} symmetry with six equidistant TM-C bonds

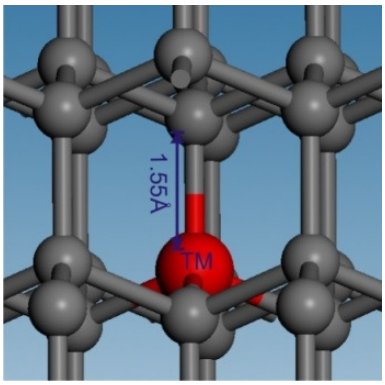

(b) Substitutional site: The transition metal replaces a carbon atom in the diamond lattice. The ideal substitutional site has *Td* symmetry with four equidistant TM-C bonds.

Figure 2.3 Illustration of a transition metal (TM) point defect at (a) divacancy (b) substitutional sites in a diamond lattice.

[‡] Constrained spin moment technique is also referred to as fixed spin moment technique.

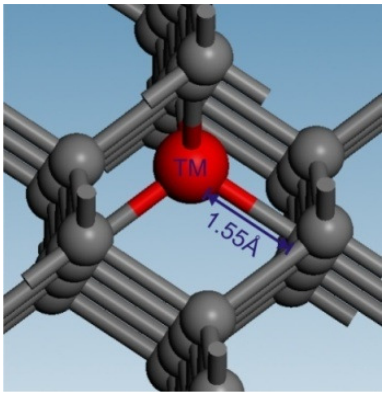

(c) Tetrahedral interstitial site: The transition metal atom is inserted at an interstitial lattice site. The ideal site has T_d symmetry with four equidistant TM-C bonds

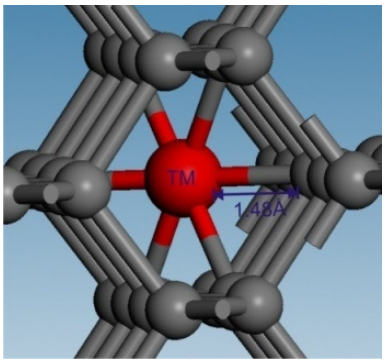

(d) Hexagonal interstitial site: The transition metal atom is inserted at a hexagonal interstitial lattice site. The ideal site has D_{3d} symmetry with sex equidistant TM-C bonds.

Figure 2.3 (Continued): Illustration of a transition metal (TM) point defect at (c) tetrahedral interstitial and (d) hexagonal interstitial sites in a diamond lattice.

2.5.2 Computational details

All calculations were performed using the Perdew-Burke-Ernzerhof (PBE) [89] generalized gradient approximation (GGA) to treat the exchange-correlation potential of electron-electron interactions, together with Ultrasoft Vanderbilt Pseudopotentials [53] in reciprocal space representation for valence-core interactions, and an optimized plane wave expansion cut-off energy of 310.0 eV, as discussed in Section 2.2. For all transition metal atoms at each lattice configuration and charge state, full geometry optimization was carried out, allowing complete relaxation of the structure using a well converged $4 \times 4 \times 4$ Monkhorst pack-grid [90] of *k*-points in the Brillouin zone (i.e. 32 *k*-points in the irreducible wedge of the Brillouin zone), together with a $48 \times 48 \times 48$ FFT grid for electron density representation [56] and SCF convergence tolerances of 1×10^{-6} eV/atom, 1×10^{-2} eV/Å and 1×10^{-4} Å for energy, force and atomic displacement, respectively. By increasing the *k*-point sampling or the plane wave cut-off energy, the optimized geometry and nearest neighbour bond lengths were found to differ by less than 0.001 Å and the total energy difference by less than 0.0001eV.

2.5.3 Spin calculations and magnetic interactions

In order to establish whether a given 3*d* transition metal ion may lead to collective magnetic ordering in diamond, the magnitude of the induced spin magnetic moments was first calculated using a 64-atom supercell containing one transition metal ion at the different lattice site configurations and charge states. The nature of magnetic interactions (i.e. ferromagnetic, ferrimagnetic, antiferromagnetic or non-magnetic) between the transition metal impurities was then determined by doubling the 64-atom diamond supercell, forming a 128-atom diamond supercell with two transition metal impurity atoms (corresponding to an impurity concentration of 1.56%) separated by twice the diamond lattice constant ($2a_0 = 7.138$ Å), as shown in Figure 2.4 (a detailed discussion of the theoretical approach used to calculate the magnetic ordering properties of transition metals in diamond is presented in section 6.2). Similar calculations in selected cases were also carried out at transition metal impurity separations of one lattice constant ($a_0 = 3.569$ Å) in order to determine the dependence of structural and magnetic stabilization energies on impurity separation. Further, different sets of symmetry orientations between the two transition metals were considered to determine the dependence of geometric orientation on the calculated spin polarisations and magnetic stabilization energies.

To determine the effect of the pseudopotential valence configuration on spin polarisation, similar calculations were performed with and without non-linear core corrections (NLCC) [45,55,56] of the transition metal atom pseudopotenetials as implemented in the CASTEP code (version 5.0.1) [41]. Table 2.2 shows the electronic configurations of 3*d* transition metals together with the corresponding standard (bare) and non-linear core corrected PBE pseudopotential configurations for each transition metal. To test the reliability of the pseudopotential approach in calculating the properties of magnetic systems, comparative calculations using FPLAPW/APW+LO/APPW+lo methods were performed for selected cases (as implemented in the WIEN2k [46] code) and the results in both techniques were found to be in good agreement.

For each charge state and lattice site, both parallel and anti-parallel spin alignments of the impurity atoms in different configurations (i.e. $\uparrow\uparrow, \downarrow\uparrow, 0\uparrow, 0\downarrow, 00, \downarrow\downarrow$) and magnitudes were allowed in order to evaluate magnetic stabilization energies and hence the ground state magnetic ordering of the system, with the implicit assumption that other mechanisms which

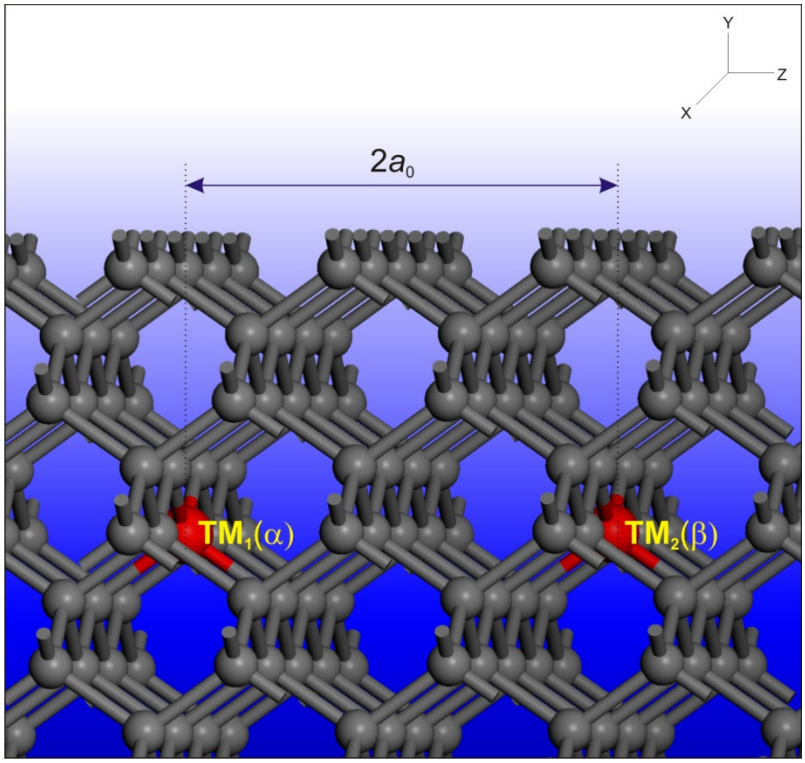

Figure 2.4: A section of the diamond supercell used to calculate magnetic interaction between two substitutional transition metal impurities TM_1 (α) and TM_2 (β), where α and β are the spin configurations of each transition metal ion. The separation between the two TM ions is two diamond lattice constants ($2a_0$ = 7.138 Å). For each lattice site and charge state, calculations were carried out for different spin configurations corresponding to ferromagnetic (α= β) , ferrimagnetic ($\alpha = \beta/n$, n = 1, 2, 3,...), antiferromagnetic α = -β and non-magnetic ($\alpha = \beta = 0$) interactions.

may contribute negatively to magnetic exchange interactions (e.g. disorder and thermal fluctuations) do not influence the magnetic ordering properties [91]. The accuracy of this method is such that small energy differences, of the order of meV, between the magnetic ground state and other metastable states can reliably be extracted from differences in quantum mechanical total energies of the different spin configurations [92,93], and such accuracy is crucial since magnetic states in magnetic materials are often separated by energies in the order of meV. Magnetic stabilization energies reported in this Thesis were well converged with respect to *k*-point sampling, plane wave cutoff energy, SCF cycles and geometry optimization, and energy differences between different spin states were found to be accurate up to 0.001 eV; therefore, magnetic states separated by an energy difference of this magnitude may be assumed to have similar spin configurations, particularly at higher temperatures where thermal effects are likely to play a major role.

It is noted that the total energy differences (between the ground spin state and other metastable spin states) obtained by the above approach describes only the nearest neighbour impurity magnetic interactions since magnetic exchange interaction between transition metal ions is often dominated by nearest neighbour interactions [94-97]. This two-defect impurity model gives a good first order approximation of the magnetic stabilization energies, and has previously been used to predict ferromagnetic ordering in other semiconductor materials and oxides [94-101] (from which the Curie temperature can be estimated [91] from first principles). An alternative model is the Green's function approach [91], where hybridization of the local moments with host electrons is included to all orders of perturbation, but this approach is computationally prohibitive.

TM	All electron orbital configuration			PBE USP configuration	
				Bare USP	USP with NLCC
Sc	[Ar] $3d^1\ 4s^2$	$3d$: ↑	$4s$: ↑↓	$3s^2\ 3p^6\ 3d^1\ 4s^2$	$3d^1\ 4s^2$
Ti	[Ar] $3d^2\ 4s^2$	$3d$: ↑↑	$4s$: ↑↓	$3s^2\ 3p^6\ 3d^2\ 4s^2$	$3d^2\ 4s^2$
V	[Ar] $3d^3\ 4s^2$	$3d$: ↑↑ ↑	$4s$: ↑↓	$3s^2\ 3p^6\ 3d^3\ 4\ s^2$	$3d^3\ 4s^2$
Cr	[Ar] $3d^5\ 4s^1$	$3d$: ↑↑ ↑↑ ↑	$4s$: ↑	$3s^2\ 3p^6\ 3d^5\ 4\ s^1$	$3d^5\ 4s^1$
Mn	[Ar] $3d^5\ 4s^2$	$3d$: ↑↑ ↑↑ ↑	$4s$: ↑↓	$3d^5\ 4s^2$	$3d^5\ 4s^2$
Fe	[Ar] $3d^6\ 4s^2$	3d: ↓↑ ↑↑ ↑↑	$4s$: ↑↓	$3d^6\ 4s^2$	$3d^6\ 4s^2$
Co	[Ar] $3d^7\ 4s^2$	$3d$: ↓↑ ↓↑ ↑↑ ↑	$4s$: ↑↓	$3d^7\ 4s^2$	$3d^7\ 4s^2$
Ni	[Ar] $3d^8\ 4s^2$	$3d$: ↓↑ ↓↑ ↓↑ ↑↑	$4s$: ↑↓	$3d^8\ 4s^2$	$3d^8\ 4s^2$
Cu	[Ar] $3d^{10}\ 4s^1$	$3d$: ↓↑ ↓↑ ↓↑ ↓↑	$4s$: ↑	$3d^{10}\ 4s^1$	-
Zn	[Ar] $3d^{10}\ 4s^2$	$3d$: ↓↑ ↓↑ ↓↑ ↓↑	$4s$: ↑↓	$3d^{10}\ 4s^2$	-

Table 2.2: All electron electronic structure of 3*d* transition metals and the Perdew-Burke- Ernzerhof (PBE) ultrasoft pseudopotential (USP) configuration without (bare) and with non linear core correction (NLCC) as implemented in the CASTEP code. Ultrasoft pseudopotentials with NLCC for Cu and Zn are not implemented in the current version of the CASTEP code.

2.5.4 Curie temperature calculations

The pair exchange interaction between magnetic ions in a diluted magnetic semiconductor is a characteristic of the nature of the magnetic ground state spin coupling. Therefore, the relative energetic stability of parallel spin ordering (ferromagnetic) versus anti-parallel spin

ordering (anti-ferromagnetic) allows determination of the properties of a diluted magnetic semiconductor, such as Curie temperature T_C, among others [91].

The most successful method [91] used to calculate the Curie temperature of a diluted magnetic semiconductor within the DFT formalism requires a statistical solution of the classical Heisenberg model (taking into account disorder and magnetic percolation effects):

$$H = -\sum_{i\neq} J_{ij}^{QQ'} \mathbf{e}_i \mathbf{e}_j \tag{2.56}$$

between two magnetic ions Q and Q', where $\mathbf{e}_i$ is a unit vector parallel to the local moment and J_{ij} are the exchange coupling constants between the local moments at sites i and j. The calculations of J_{ij} are based on a number of approximations [91], and the most common approximation is the Mean-Field Approximation (MFA). Improved and numerically exact methods that go beyond the MFA approximation include the Local Random Phase approximation (LRPA), which is semi analytical, and the Monte Carlo simulations, which is computationally intensive. Both of these methods require explicit knowledge of the distance dependence of the exchange coupling constant $J_{ij}^{QQ'}$ between the two magnetic atoms [102,103], while the MFA technique does not. Nevertheless, the MFA technique has been found to give reliable estimations of T_C for a wide range of diluted magnetic semiconductors [91], and thus has been used in this Thesis to estimate the Curie temperature of transition metal-doped diamond.

Within the MFA approximation, the T_C of a diluted magnetic semiconductor is given by

$$T_C^{MFA} = \frac{2}{3k_B} c \sum_{n\neq 0} J_{0...n} \tag{2.57}$$

where k_B is the Boltzmann constant and c is the concentration of magnetic impurities in the semiconductor matrix. It can be shown that $\sum_{n\neq 0} J_{0...n}$ is directly related to the ferromagnetic stabilization energy, defined as the difference of the total energies between the ferromagnetic and antiferromagnetic or non-magnetic moment states (ΔE), as [91]

$$\Delta E = c^2 \sum_{n\neq 0} J_{0...n} \,. \tag{2.58}$$

Therefore, in terms of the ferromagnetic stabilization energy, the critical temperature needed to create magnetic disorder can be evaluated as

$$T_C^{MFA} = \frac{2}{3k_B}\left(\frac{\Delta E}{c}\right). \tag{2.59}$$

Though this is a first order approximation, this technique has been found [104] to give reliable values of T_C for a wide range of homogeneous ferromagnetic and disordered ferromagnetic alloys containing small impurity concentrations (about less than 5%). In this Thesis, a constant transition metal impurity concentration of 1.56% (corresponding to two transition metal impurities in a 128-atom diamond supercell) was used for calculating the magnetic stabilization energies. It is important to note that this concentration will be above the expected thermodynamic solubility limit; however, it should also be noted that a sufficiently large impurity concentration in the semiconductor host needs to be achieved such that the magnetic interaction forms a percolation path through the lattice [105,106], that is, an uninterrupted, wall-to-wall chain of moments [107].

3. Diluted magnetic semiconductors and defects in diamond

3.1 Introduction

Magnetic ordering in metals has been the backbone of information processing and storage devices for many years. A key milestone in this area was the discovery of the Giant Magneto Resistance (GMR) effect [108], in which the resistance to the flow of charge in thin films consisting of alternating ferromagnetic and non-magnetic metal layers was found to be strongly dependent on the applied magnetic field. At present, this change in resistance (called magneto-resistance) with the direction of magnetization is used in high volume information storage (e.g. computer hard disk reading heads, and MRAM chips) to sense changes in magnetic fields; whereas switching and retrieval is achieved separately by controlled flow of charge carriers [109].

The emerging field of spin-based electronics, called spintronics, seeks to achieve the complementary functions of magnetism and electronics within same material devices by exploiting the spin property of an electron instead of, or in addition to, its charge. This prospect has successfully been demonstrated by use of Diluted Magnetic Semiconductor (DMS) materials as one of the methods through which magnetism can be integrated with electronics, by doping of semiconductor materials with suitable magnetic impurities, such as transition metal atoms. As opposed to the metal-based GMR technology devices, semiconductor-based spintronic devices could in principle provide conventional electronics functionalities (e.g. amplification) and serve, in general, as information storage devices, amongst others.

DMS materials are standard semiconductors in which a small fraction of their constituent atoms has been replaced by magnetically ordering impurities (e.g. transition metal atoms) capable of providing both magnetic moments and spin polarised charge carriers in the semiconductor matrix. This integration results in a strong spin-dependent coupling between band and localized states, thus potentially serving as a possible means of injecting, controlling and detecting spin properties. However, current challenges towards practical

implementation in spintronic devices include low Curie temperatures and lack of desirable spintronic properties [4] in the semiconductor materials which have so far been considered [3,104,110]. Although a lot of research efforts have been directed towards understanding and improving the mechanisms of spin transport in these semiconductor materials, there is still a need to find new DMS materials which may successfully be used in spintronic devices capable of operating at room temperature.

3.2 Progress on Diluted Magnetic Semiconductors

The incorporation of transition metal impurities into non-magnetic host semiconductors started in the 1960s [111] and was aimed at combining the complementary properties of semiconductivity and ferromagnetism in single material systems. Among the most extensively studied ferromagnetic semiconductors were Eu doped Chalcogenides (e.g. EuSe, EuS, EuO) and Cr doped Chalcogenides (e.g. $CdCr_2Se_4$, $CdCr2S_4$), but no practical application of these materials has been realized to date, mainly due to their low Curie temperatures and extreme difficulties in growing these crystals [112].

The next generation of DMSs began in the 1980s and focussed mainly on manganese doped II-VI and IV-VI heterostructures (e.g. $Cd_{1-x}Mn_xTe$, $Cd_{1-x}Mn_xSe$, $Hg_{1-x}Mn_xTe$) [112] due to their ternary nature which offers the possibility of tuning their band gap [113] by changing the concentration of the magnetic ions. In addition, the cation valency of these materials closely matches that of common magnetic dopant ions like Mn which made them relatively easy to grow. Although many fundamental studies in these systems have been carried out [114,115], useful magnetic ordering phenomena for various transition metals has not been achieved yet at room temperature due to antiferromagnetic coupling of the transition metal spins with those of the host semiconductors [112]. On the other hand, *p*- type and *n*-type doping in II-VI ternaries is not easy to achieve, which made it relatively difficult to study their transport properties [111,116]. In addition, the solubility limits of the magnetic ions in these DMSs was also found to be generally small, and varied markedly from alloy to alloy [117]. However, these materials can be grown with relatively high concentration of free band carriers, and it was later demonstrated that their magnetic properties can be controlled by modifying their charge concentration [2]. But, lack of appropriate material technologies that would allow a high concentration of the magnetic impurities made these materials less attractive for technological applications [116].

Rapid progress on the research of DMS started in the 1990s following the successful epitaxial growth of Mn doped InAs and GaAs using non-equilibrium low temperature Molecular Beam Epitaxial (MBE) growth conditions [118-120]. This method made it possible to increase the concentration of magnetic impurity ions and substantially increase their electrical activity beyond thermal equilibrium solubility limits. Subsequently, various other semiconductors were studied in an attempt to increase their ferromagnetic transition temperature to more practical limits. Although progress in synthesizing and controlling the magnetic properties of DMSs was remarkable, the reported Curie temperatures were still far too low below room temperature to have any significant practical impact [121].

Recent studies on spintronics has focused on achieving practical magnetic ordering temperatures in many semiconductors, and tremendous progress has been made both in realizations of high quality epitaxial layers and on theory of magnetic ordering in DMS. As a result, several materials have theoretically been predicted to order ferromagnetically above room temperatures, but the ferromagnetic ordering properties of diamond are yet to be studied in detail. Although ferromagnetism has experimentally been reported in some of these materials, particularly in oxides [104], the results are unfortunately experimentally irreproducible, and are often due to spurious effects [122].

An important step in the search for high T_C DMSs was the theoretical prediction of the relationship between the T_C of a DMS and the properties of the host semiconductor for hole mediated ferromagnetism [121,123]. This result follows from the Zener model [124] of ferromagnetic interactions from which the spin-spin coupling may be assumed to be long range, allowing use of a mean field approximation [121,123,125]. In the presence of carriers, T_C is determined by a competition between ferromagnetic (T_{AF}) and antiferromagnetic (T_{AF}) interactions, and can be expressed as [104]

$$T_C = \frac{N_O x_{eff} S(S+1)\beta^2 A_F \left(m^* k_F / h^2\right)}{12 k_B} - T_{AF} \tag{3.1}$$

where, $N_o x_{eff}$ is the effective spin concentration, S the localized spin state, β the p-d exchange integral, k_B the Boltzmann constant, A_F the Fermi liquid parameter and $m^* k_F / h^2$ describes the density of sates at the Fermi level (m^* being the effective mass of the density of states, and k_F the Fermi wave vector).

The most direct dependence of T_C on the host semiconductor's physical properties comes from the density per unit volume of cation sites N_0, which in turn has a reciprocal dependence on the host semiconductor's lattice constant as $1/a_0^3$. Refinements of the mean field solution of the Zener model for predicting T_C take into account the effects of positional disorder [102,103], indirect exchange interactions [126], spatial inhomogenities and free carrier spin polarisation [127,128], but still the mean field approach and its variants has been found to produce reliable estimates of T_C compared to experimental values for a wide range of materials [104]. Accordingly, semiconductor hosts with larger lattice constants have been predicted to have lowest T_C, while hosts with smaller lattice constants have been predicted to have largest T_C, well above room temperature, as illustrated in Figure 3.1 – which makes diamond one of the most suitable material candidates for high temperature ferromagnetic ordering because of its small lattice constant (a_0 = 3.567 Å [6]) compared to other semiconductors.

In addition, diamond is well known for its extreme properties (high electron and hole mobility, high breakdown field, excellent thermal conductivity, among others [19,20]). Thus achieving ferromagnetic ordering in diamond is expected to pave the way for spintronic devices with exceptional performance regarding high temperature, high power and high frequency applications.

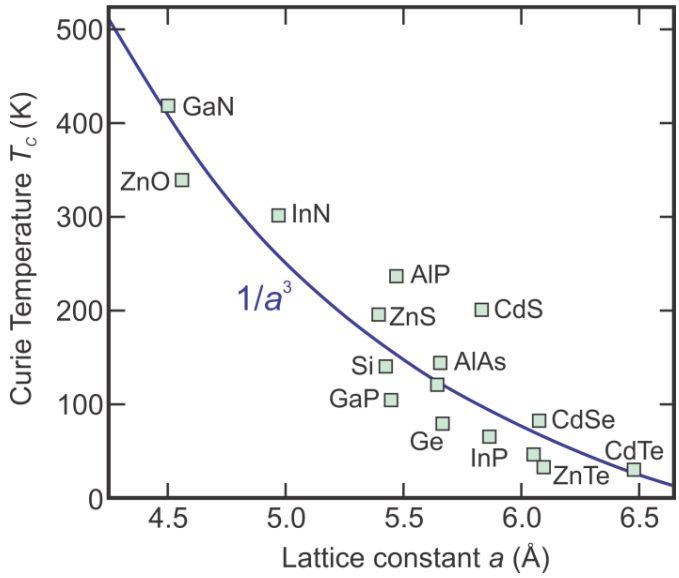

Figure 3.1: Calculated Curie temperatures for various diluted magnetic semiconductors as a function of lattice constant showing the reciprocal dependence of T_C on the host semiconductor's lattice constant as $1/a_0^3$ (adapted from reference [3]). The estimated *Tc* of diamond from this relationship is is ~700 K.

3.3 The potential of a diamond-based diluted magnetic semiconductor

Recent developments in techniques to grow high-purity single crystal synthetic diamonds have made diamond more attractive for solid state electronics [129]. Diamond, in its bulk as well as thin film forms, offers the opportunity not only to improve the operating performance of many existing technological systems, but also to develop a wide variety of new technologically advanced devices due to its combination of good optical, thermal, mechanical and electronic properties. Pure diamond is an electrical insulator, but when doped with suitable impurities can become an excellent semiconductor with superior performance regarding power efficiency, power density, and high frequency properties [130] – thus making it an ideal material for active spintronic device applications. This prospect has attracted a lot of research activities in diamond aimed at finding suitable defects or impurities which may give rise to desirable electronic and spintronic applications.

An important property of diamond's suitability for spintronic applications is its large band gap which may allow impurities to be excited without becoming ionized [129] at elevated temperatures (hence no "thermal run away" as in the case of Ge under laser irradiation [131]), thus allowing quantum spin states to retain their quantum coherence for usefully long times. Indeed, recent studies have shown that isotopically engineered CVD diamond has the longest room-temperature spin dephasing times ever observed in solid-state systems (T_2=1.8 ms) [11], and diamond's potential in quantum computing and spintronic applications has already been demonstrated at room temperature in the N-V centre [129], as well as in Cr [9] and Ni [10] related complexes in diamond.

3.4 Impurities and point defects in diamond

Defects in semiconductor materials not only influence their electrical and optical properties, but also exhibit other important properties (such as magnetic ordering) which can be beneficial in enhancing semiconductor functionalities. In either case, the identification and control of defects and impurities in diamond (such as transition metals, dopants, self vacancies and other impurity-related complexes) is important in realizing diamond-based applications in electronic and spintronic devices. Defects in diamond have been studied using a wide range of experimental techniques, including Electron Paramagnetic Resonance (EPR) spectroscopy [132-136], photoluminescence (PL) spectroscopy [137,138], Raman

spectroscopy [139] and Deep Level Transient spectroscopy (DLTS) [140,141], and a large number of impurities and defects have been found to exist in diamond; their type greatly depends on relative stability and concentration as determined by the history of diamond, in particular whether it is natural or synthetic [142]. A review of some important defects and impurities in diamond is given below.

3.4.1 Transition metal impurities

Most experimental and theoretical studies of transition metals in diamond are based on Ni and Co which are commonly used as 'solvent catalysts' during High Pressure-High Temperature (HPHT) growth of synthetic diamond. The precise form of these atoms in diamond has been under considerable discussion as initially it was thought that such ions were too large for inclusion into diamond. Although other transition metals such as Fe, Mn and Cu are also used during growth, only Ni [143,144] and Co [7,145] related defects have been identified positively as being incorporated into the diamond lattice. There is also unconfirmed evidence [146] for Cr, Mn, Cu and Fe, while incorporation of Ti and Zn has only been achieved by ion implantation, but not during crystal growth [147-149].

Theoretical studies have shown [146] that the electronic structure of transition metals in diamond is complicated by the presence of dangling bonds as well as the weak bonding between the 3*d* transition metal ion and carbon atoms in diamond – it has been found that the key electronic states originate from combinations of the transition metal's 3*d* electrons with the dangling bond states [7]. The resultant shift in energy due to interactions between the dangling bonds and the *d* orbitals determines the overall electronic structure and stability of a given charge state as well as the relative stabilities between different lattice sites in a particular charge state. In addition, the presence of other defects such as nitrogen and boron, which are the most dominant impurities in synthetic and natural diamonds (other fundamentaldefects in diamond include the vacancy and the self interstitial), have also been found to play a significant role in influencing the energetic stability of the different charge states [150].

3.4.1.1 Nickel

Nickel is the most commonly observed transition metal impurity in HP-HT diamond, and is mainly incorporated in the <111> growth sectors [151]. The observed properties of Ni-related centres are strongly affected by the presence of other impurities or defects (e.g. N, B or

vacancies) in diamond, and the lattice location or its charge state often depends on the concentration of these defects [152].

Experimentally, nickel related defects in diamond have been identified at various lattice sites and charge states, but there is less evidence for the presence of an interstitial species [152]. At the substitutional site, Ni-related defects have been identified in the negative charge sate (Ni_s^-) with a T_d symmetry and a spin of $S = 3/2$ (labelled W8 [153] which has been correlated to a donor level at $(E_C - 2.49)$ eV [154], and optical absorption peaks at 2.51 eV and 1.88 eV [154]) in diamonds containing nitrogen impurities. However, in cases where the nitrogen concentration is low (or where B is present), the W8 and its associated optical centres disappear, giving rise to other new EPR centres [152], such as NIRIM-1 (electrical levels at $E_C - 1.98$ eV) and NIRIM-2 (absorption and luminescence 1.404 eV doublet) which have been attributed to T_d interstitial nickel in the positive charge state (Ni_i^+) perturbed by a vacancy [155] or a boron acceptor [156]. Numerous other optical Ni-related centres have been identified, many of which have been found to occur after subsequent heat treatments, suggesting aggregation particularly in nitrogen containing samples [157]. A class of EPR centres labelled NE1-NE9 have also been identified and attributed to Ni at a divacancy site in diamond containing nitrogen impurities at various concentrations [151].

The majority of these experimental observations of nickel features have been confirmed by theoretical calculations [151], though the assignment of Ni_i^+ to NIRIM centres have been predicted to be energetically unstable; the formation energy and mobility of the interstitial species suggest that nickel will be predominantly of the substitutional form [151]. Although the aggregation of Ni with other defects has theoretically been confirmed [158,159], indications that the NE group of centres are negatively charged in N containing diamond presents a possibility of other forms of the centre in *p*-type diamond, for example the Ni-V complex at $(E_C - 4.3)$ eV which has been found to occur in B-doped diamond [159,160].

3.4.1.2 Cobalt

Other than nickel, cobalt is the only other transition metal that has also been identified positively in HP-HT diamond [152,161]. Although the physical and chemical properties of cobalt and nickel are somewhat similar, the concentration of cobalt in diamond has been found to be relatively lower than that of nickel – which explains why nickel is more readily detected in diamond compared to cobalt [161].

A number of photoluminescence (PL) peaks and EPR centres in HP-HT diamond grown with cobalt as a catalyst have been identified [152] in various charge states and lattice locations. As in the case of nickel, the observed properties of these centres are strongly affected by the presence of nitrogen in diamond samples. Among the EPR centres which have been linked to cobalt in diamond include a hyperfine structure attributed to interstitial cobalt in the double positive charge state Co_i^{+2} [162] and other centres with a spin of $S = 1/2$ (labelled O4, NLO2, and NWO1 [145]), whose microscopic models have theoretically been suggested [163] to be a cobalt atom at a divacancy site interacting with a nearby substitutional nitrogen atom in the negative charge state $(VCoVN_s)^-$. In addition, a PL peak at 2.367 eV with a level at 4.4 eV below the conduction band has been identified [152] and attributed to a complex of substitutional Co and nitrogen which, like in the case of nickel, indicates a likelihood of a family of cobalt-nitrogen defects forming after high temperature annealing.

3.4.1.3 Manganese

A large class of diluted magnetic semiconductors are based on manganese doping [73]. However, theoretical predictions of ferromagnetic ordering of neutrally charged Mn in diamond have been predicted to be unlikely [73]. Efforts to find alternative transition metals which may order ferromagnetically in diamond have predicted ferromagnetic ordering in Co-doped diamond with a resultant moment of 0.4 μ_B per an impurity atom and ferromagnetic stabilization energy of 22 meV in the neutral charge state [164]. However, the magnetic ordering properties of Mn and Co in other charge states remain to be understood. In addition, relatively large magnetic moments and ferromagnetic stabilization energies are required in order to support significant spin polarisation at high Curie temperatures. Hence, there is need to find alternative transition metal ions which may successfully be considered in the search of a diamond-based DMS.

3.4.1.4 Other transition metals

Several theoretical [146,148,165] studies have been carried out on the 3*d* transition metal series in diamond, and have suggested that other transition metals should be present in diamond. While most of these studies have been directed towards investigating the electronic, electrical and structural properties corresponding to specific experimentally observed centres, as in the case of cobalt and nickel, no systematic studies have been carried out on their magnetic ordering properties which are better understood in other group IV semiconductors such as silicon [148,166,167] and germanium [168].

3.4.2 Dopants in diamond

Despite diamond's potential in spin-based electronics, efficient *n*-type doping of diamond has remained a major challenge towards full utilization of diamond as a novel electronic material. The general factors that have been identified as possible limitations to successful doping in diamond include creation of energetically deep donor/acceptor levels, insufficient donor solubility and charge compensation [169]. While the issue of donor/acceptor levels and solubility may be circumvented by the choice of different dopant impurities or by changing growth conditions [79,170-173], charge compensation can be said to be the main factor limiting dopability in diamond [169]. However, continued research on alternative growth and doping approaches has shown promise in overcoming these difficulties.

3.4.2.1 *n*-type dopants

Trends in silicon suggest that potential *n*-type dopants in diamond are the group V elements of the periodic table (such as nitrogen and phosphorus). However, the only donor so far which is usually incorporated into diamond is phosphorus, but with a relatively deep donor level at $E_C - 0.6$ eV [174].

Although many examples of electronic devices employing P-doped diamond have been demonstrated at high temperatures [151], there is need to develop shallower *n*-type dopants; much of the research efforts in determining the likely candidates are based on quantum mechanical modelling [151]. In particular, phosphorus's high formation energy in diamond (~7 eV [175] in CVD diamond) leads to lower solubility and hence lower electron concentrations (up to 2×10^{19} cm^{-3} [176]) which make diffusion methods generally inappropriate. However, the use of plasma-enhanced CVD conditions has theoretically been predicted [169] (and validated by experiments [173]) as a successful method through which the solubility of phosphorus in diamond can be enhanced. An alternative approach which has also been considered is ion implantation, but implantation related complexes, e.g. vacancies and self interstitials have been found to act as compensation centres, resulting in deeper donor levels [177].

Nitrogen is abundant in natural diamonds and is easily incorporated into synthetic diamonds, but its deep donor level of $E_C - 1.7$ eV [178] makes it inapplicable for room temperature electronic applications. In most synthetic and some rare natural diamonds (type 1b), nitrogen

is incorporated in single substitutional form in the lattice, and both experimental and theoretical [23] data has shown that the nitrogen atom moves off-lattice along the <111> direction, resulting in a centre with C_{3v} symmetry. The origin of the distortion has been shown [23] to originate from preferential formation of a lone-pair orbital on nitrogen and a dangling bond orbital on the unique carbon neighbour which forms bonding and anti-bonding orbitals due to sp^3 hybridization.

3.4.2.2 *p*-type dopants

Unlike the difficulties experienced in *n*-type doping of diamond, *p*-type diamond is readily achieved by boron doping. Boron exists in natural type IIb diamond with an acceptor level of $E_V + 0.37$ eV and has therefore been widely studied [179] as a *p*-type dopant in diamond. It is the most commonly used impurity for *p*-type conductivity in diamond and the results obtained are of good quality, so that limited data on other possible *p*-type dopants are available.

Although natural type IIb diamond is *p*-type due to substitutional boron impurities, its electron mobility and compensation ratio cannot be controlled effectively. Controlled *p*-type conductivity can be obtained by artificially grown diamond with the same activation energy as that of natural diamond. For example, results of highly conducting *p*-type diamond with an activation of up to 30% of the implanted boron atoms have been reported using high dose ion implantation [180,181]. In general, however, the doping efficiency obtained by implantation [180,181] of boron into diamond is fairly low, with hole mobilities not as high as in natural or boron doped CVD diamond, even after high temperature (>1400 K [180,181]) annealing. On the other hand, B-doped CVD diamond films have been grown with boron concentrations of up to 1×10^{21} cm^{-3} [20,182], and even at low or medium concentrations the hole mobility can be as high as that of natural diamond, with a very high doping efficiency. It is worth noting that heavily B-doped diamond has a well-defined impurity band, but doping it more heavily makes it metallic, and this strongly B-doped material is a superconductor [183,184].

4. Energetic stability of isolated 3*d* transition metals in diamond

4.1 Introduction

Understanding of the energetic properties of defects in semiconductors is fundamental for the development of semiconductor-based technology. In particular, the magnetic properties of Diluted Magnetic Semiconductors (DMS) depend on the energetic positions of induced defect levels which arise from interactions between the impurity and the host semiconductor. The energy of the induced defect levels in the host semiconductor's band gap, together with the on-site correlation energy, determine the electrical activity of an impurity defect and the behaviour of its charge or spin states in the presence of other impurities within the semiconductor matrix [185].

Impurity defects in semiconductors usually introduce defect levels in the host band gap due to transitions between different charge states of the defect centre. The experimental detection of these levels often forms the basis for identification of the defect, and therefore prediction of defect levels for magnetically ordering impurities in diamond may help to shed light on some of the properties of diamond that are not yet fully understood [72].

Based on diamond's small lattice constant and excellent physical and electrical properties, diamond-based DMSs are expected to possess high Curie temperatures [3] with superior performance in high temperature, high power and high frequency applications. In particular, diamond's high intrinsic hole and electron mobilities (3800 $cm^2V^{-1}s^{-1}$ and 4500 $cm^2V^{-1}s^{-1}$, respectively [17]), thermal conductivity (22 $Wcm^{-1}K^{-1}$ [19]) and breakdown field (10000 $KVcm^{-1}$ [18]), compared to other semiconductors [19,20], make it an ideal material for fabrication of semiconducting devices with a wide range of applications. For example, diamond's potential in room temperature quantum computing applications, has already been demonstrated using the N-V defect centre [129], and it is therefore expected that other defects such as those related to transition metal impurities may potentially lead to room temperature ferromagnetic ordering in diamond, thus making it a candidate material which, in addition to its extreme properties, may successfully be considered for spintronic device applications.

However, one of the problems that require to be addressed is that of predicting the energetically most stable lattice configurations or charge states in which such dopants will remain electrically active, and at the same time induce magnetic moments when incorporated into diamond.

Previous studies on the energetic stability of transition metal defects in diamond have focused mostly on those transition metals (Mn, Fe, Ni, Co, Cr) which are commonly used as catalysts during High Pressure-High Temperature (HPHT) growth of synthetic diamond. However, no explicit explanation exists as to why some of these transition metals are experimentally found to be preferentially incorporated into diamond containing other impurities, such as nitrogen [152]. In addition, the failure to positively identify all active centres related to transition metal impurities in diamond remains an important challenge in understanding the properties of transition metal impurities in diamond. Therefore, a detailed assessment of the energetic properties of transition metal defects in diamond is fundamental for the development of a diamond-based DMS.

In this Chapter, the formation energies of isolated 3*d* transition metal defects in diamond at various lattice sites and charge states is discussed, and it is demonstrated that their energetic stability is critically dependent on the charge state, and the type of diamond doping (i.e. intrinsic, *p*-type or *n*-type).

4.2 Formation energy

4.2.1 Formation energy in intrinsic diamond

Figure 4.1 presents the calculated formation energies of isolated 3*d* transition metals in the neutral charge state at the divacancy, substitutional and interstitial lattice sites in diamond, obtained from a 64-atom diamond supercell using a well converged $4 \times 4 \times 4$ Monkhorst-Pack grid of *k*-points and a plane wave cut-off energy of 310 eV, as discussed in Sections 2.4 and 2.5. A distinctive trend of the calculated formation energies is seen across the 3*d* series, whereby transition metals in the middle of the series are predicted to be energetically more stable compared to those early or late in the series, with Mn having the lowest formation energy at any lattice site – a result which can be explained by the electron filling of the *d* orbital [185] and the relatively large free atomic radius of transition metal atoms compared to diamond's lattice constant. This trend is qualitatively similar to what has been obtained in

previous calculations [186,187], except with some quantitative differences which may be attributed to the relatively small number of *k*-points used for integration over the Brillouin zone (in reference [187]), and the low plane wave cut off energy or small cluster size (in reference [186]).

We find the majority of transition metals in the neutral charge state to be more stable at the divacancy site compared to the substitutional or interstitial sites, with the interstitial sites being highly unfavourable (by ~8 – 10 eV relative to the divacancy site), thus making it unlikely for the interstitial species to be observed in significant concentrations at any charge state (Figure 4.2) under equilibrium conditions. In a divacancy configuration, the transition metal occupies the mid-point between two neighbouring carbon vacancies but it is thought that the transition metal atom initially enters the diamond lattice at either an interstitial or a substitutional site during growth [186]. This causes a lot of strain to the diamond lattice (with a proportional increase in the crystal's total energy) due to the large atomic radius of the transition metal atom compared to diamond's lattice constant. At high temperatures, for example during post-growth high temperature annealing treatment, neighbouring carbon atoms are ejected, thus forming divacancy centres which then relieves the crystal stress, therefore reducing the crystal energy.

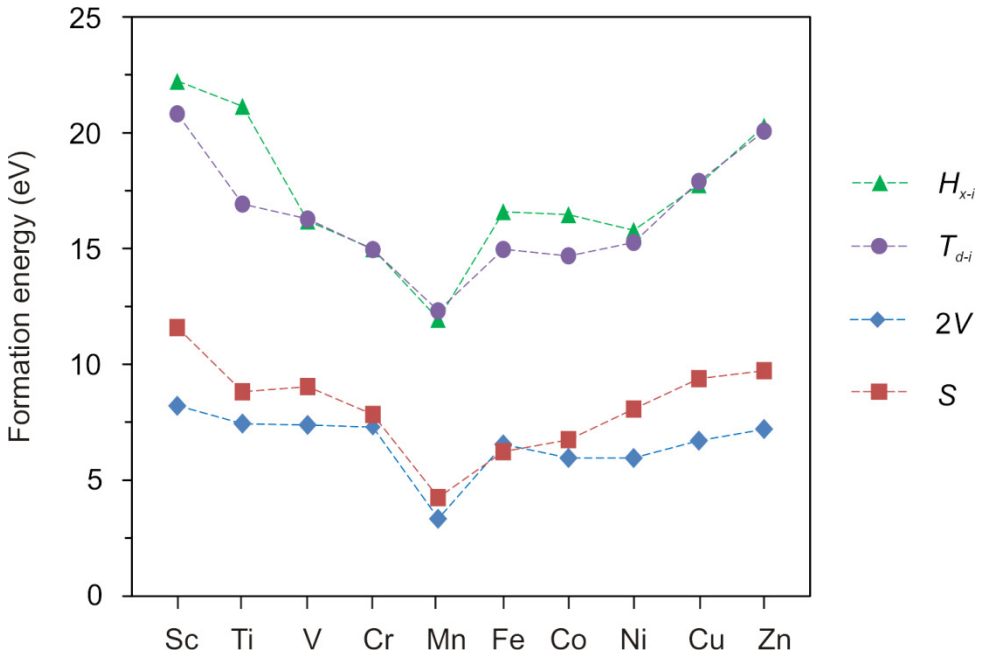

Figure 4.1: Trends in formation energies of neutral 3*d* transition metals in intrinsic diamond at substitutional (*S*), divacancy (2*V*), hexagonal interstitial ($H_{x\text{-}i}$) and tetrahedral interstitial ($T_{d\text{-}i}$) lattice sites. Data points correspond to the calculated formation energies; lines show the trend.

4.2.2 Formation energy in doped diamond

Figure 4.2 presents the formation energies of 3*d* transition metals as a function of Fermi energy, calculated within the experimental band gap of diamond (E_g = 5.49 eV) at substitutional, divacancy and interstitial lattice sites. For each transition metal, only the charge state with the lowest formation energy for a given value of the Fermi level is shown. It is clear that the stability of a particular charge state is dependent on Fermi energy, and each of the 3*d* transition metal defects in diamond are stable in the +2, +1, 0, -1, and -2 charge states, each for different ranges of the Fermi level. The formation energies for each of these charge states is summarized in Table 4.1 for *n*-type and *p*-type diamond determined at Fermi levels corresponding to *p*-type B-doped ($E_V + 0.37$ eV) and *n*-type N-doped ($E_C - 1.6$ eV) or P-doped ($E_C - 0.6$ eV) diamond, respectively. Although transition metal complexes with these dopants may form, it has previously been noted [160,188] that their role is to shift the Fermi level of the system, therefore influencing the observed charge states of isolated transition metal defects in the diamond crystal.

Importantly, we find that the most stable charge states and site configuration are strongly dependent on the position of the Fermi level or the type of diamond doping (intrinsic, *n*-type or *p*-type) with reference to the pinning of the Fermi level by co-doping with B, N or P, and it is evident that the neutral charge state is not the most stable charge state for a significant portion of the band gap. This study therefore considers, for the first time, all possible charge states of 3*d* transition metals in diamond to establish a decisive picture of their impurity formation energy, donor/acceptor levels and magnetic ordering as a function of charge state and lattice site as discussed in the subsequent Chapters.

In general, we find that the formation energies of transition metals in any charge state or lattice site are considerably lower both in *p*-type or *n*-type diamond compared to intrinsic diamond, suggesting that co-doping with boron, nitrogen or phosphorus will considerably enhance their energetic stability in diamond. In particular, the formation energies of transition metals in the negative charge states in *n*-type diamond are predicted to be considerably lower than the neutral charge state, consistent with experimental results where transition metal ions are often observed in diamond containing nitrogen impurities [152].

Across the 3*d* series of transition metals, the majority of charge states at any position of the Fermi energy are energetically favourable at the divacancy site, in agreement with previous results for Co and Ni which are known [175,189] to be incorporated into synthetic diamond during HPHT growth. However, we find that Fe^{+2}, Fe^{+1}, Co^{+2}, Co^{+1}, and Ni^{+1} are energetically more stable at the substitutional site in *p*-type diamond by $0.4 - 1.5$ eV compared to the divacancy site, while in V^{+2}, Cr^{+2}, and Cu^{+2}, the formation energy difference between the divacancy and substitutional sites is only 0.05 eV, 0.25 eV and 0.64 eV, respectively. This relatively small energy differences between the substitutional and divacancy sites implies that these charge states may be observed at both of these site configurations, in agreement with ion implantation data for Fe doped diamond [190] where 65 % of Fe ions were found to be located at the substitutional site.

The formation energies of the most stable charge states at the substitutional and divacancy sites (in both *n*-type and *p*-type diamond are comparable to that of phosphorus in diamond (~7 eV [175]), which is routinely incorporated into diamond by CVD methods in concentrations of up to 2×10^{19} cm^{-3} [176]. This suggests that incorporation of transition metals into diamond may also be achieved using similar non equilibrium techniques, or ion implantation.

Indeed, in addition to Ni and Co which are also known [175,189] to be incorporated into HPHT diamond as contaminants during growth, Cr related single photon emitters with a short radiative lifetime have been observed [9,191,192] in single crystal CVD diamond grown on sapphire substrates, and the Cr incorporation was ascribed to the likely diffusion of Cr from the sapphire substrate during CVD diamond growth [193]. Similar bright Cr related single photon emitters were observed in ion implanted [193] CVD diamond with a small N concentration. Co-implantation with S or O increased the yield of the Cr related single photon emitters; this was ascribed to S and O likely acting as deep donors in the diamond band gap [193,194], suggesting that the properties of transition metals in diamond will be strongly affected by the presence and concentration of shallow impurities (intentional or unintentional), particularly nitrogen and boron, which are the most common impurities in natural and synthetic diamonds. Therefore, it follows that any charge state-specific or lattice site-specific magnetic ordering properties of transition metals in diamond will similarly depend on the concentration of these dopants and other intrinsic defects in diamond, such as self interstitials or vacancies, which may shift the Fermi level of the system.

Further, it is noted that the formation energy of 3*d* transition metals in diamond is strongly dependent on the type of precursors used for their incorporation into diamond. For example, we find that the formation energy of divacancy Cr^0 in intrinsic diamond relative to bcc Cr metal is 7.29 eV, while relative to organo-metallic sources, such as bis-benzene chromium $Cr(C_6H_6)_2$ and hexacarbonlyl chromium $Cr(CO)_6$, we find formation energies of 6.65 eV and 13.51 eV, respectively[§]. In contrast, the formation energy of divacancy Cr in intrinsic diamond, relative to that in sapphire (Al_2O_3) is predicted to be substantially lower[**] (5.11 eV), while for incorporation from sapphire into *n*-type diamond, we find this formation to be further reduced to $1 - 3$ eV. This demonstrates a strong dependence of the formation energy of transition metal related defects in diamond on the type of precursor used for their incorporation, in addition to the type of doping of diamond.

[§] The chemical potential of chromium μ_{Cr} from bis-benzene chromium $Cr(C_6H_6)_2$ was determined relative to that of benzene C_6H_6, as $\mu_{Cr} = E_{tot}[Cr(C_6H_6)_2] - 2E_{tot}[C_6H_6]$, while for hexacarbonyl chromium $Cr(CO)_6$, the Cr chemical potential was taken relative to carbon monoxide CO as $\mu_{Cr} = E_{tot}[Cr(CO)_6] - 6E_{tot}[CO]$.

[**] The chemical potential of Cr from sapphire, μ_{Cr} was determined from Cr substituting Al in an $Al_{32}O_{48}$ sapphire crystal, relative to a similar pure sapphire crystal and fcc Al metal, using $\mu_{Cr} = E_{tot}[CrAl_{31}O_{48}] - E_{tot}[Al_{32}O_{48}] + E_{tot}[Al_{fcc}]$.

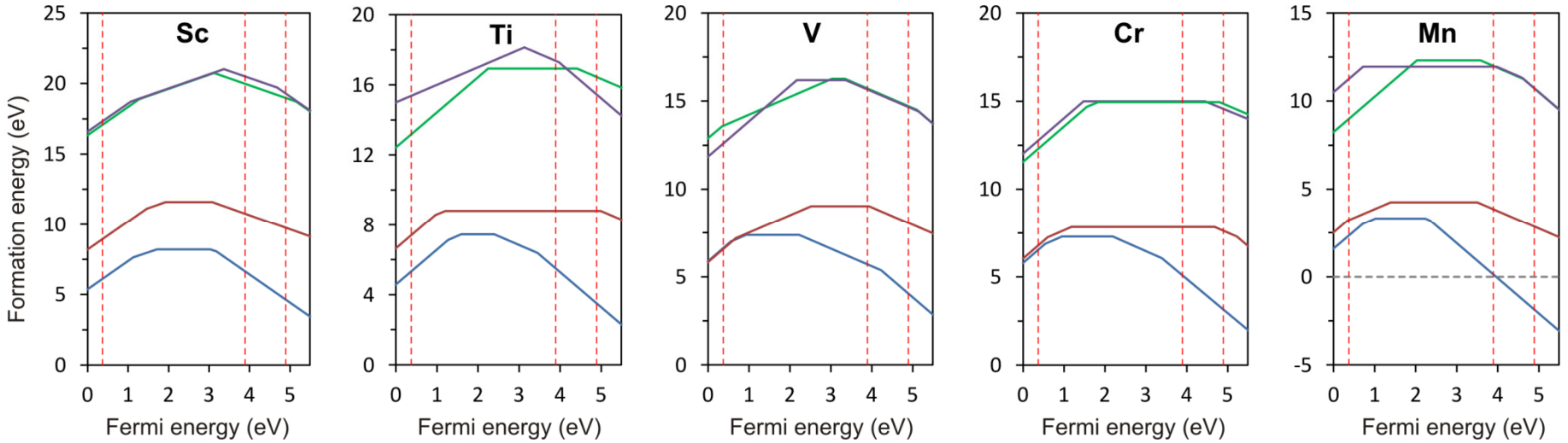

Figure 4.2: Formation energies as a function of Fermi level for isolated 3*d* transition metals (Sc, Ti, V, Cr and Mn) at divacancy (blue line segments), substitutional (dark red line segments), hexagonal interstitial (green line segments) and tetrahedral interstitial (purple line segments) lattice sites in diamond. The Fermi level is given relative to the valence band maximum and corresponds to a Fermi energy of 0 eV, while the conduction band maximum corresponds to the band gap energy of diamond (5.49 eV). Only segments corresponding to the lowest-energy charge states are shown; the slope of these segments corresponds to the charge state ($q = +2, +1,\ 0, -1, -2$), and bends in the curves indicate transitions between different charge states as detailed in Figure 4.4 and 4.5 for the divacancy and substitutional lattice sites, respectively.

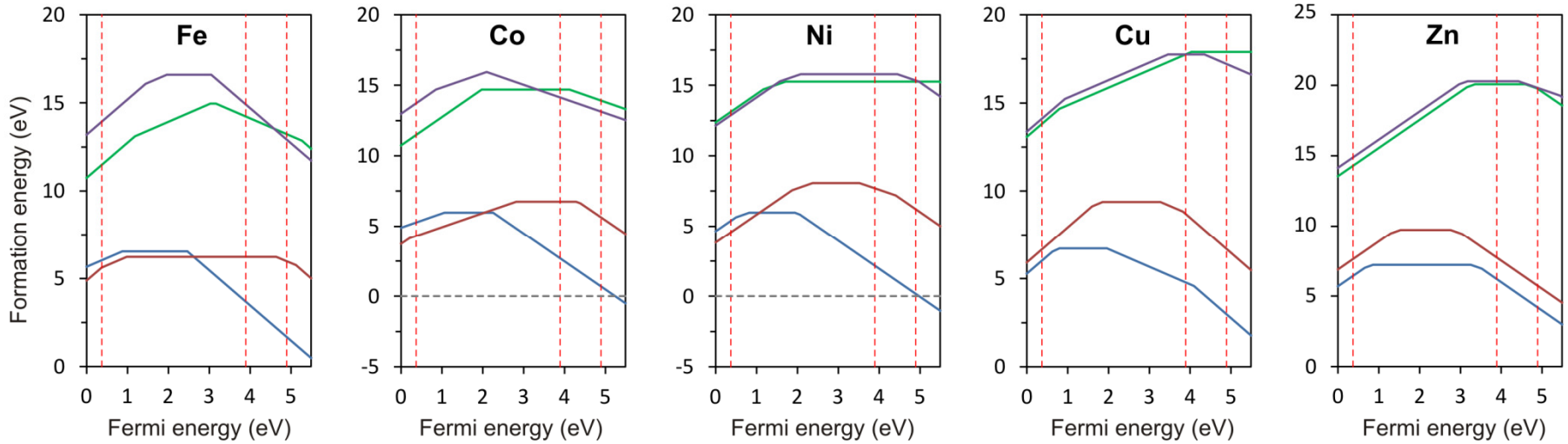

Figure 4.2 (continued): Formation energies as a function of Fermi level for isolated 3*d* transition metals (Fe, Co, Ni, Cu, and Zn) at divacancy (blue line segments), substitutional (dark red line segments), hexagonal interstitial (green line segments) and tetrahedral interstitial (purple line segments) lattice sites in diamond. The Fermi level is given relative to the valence band maximum and corresponds to a Fermi energy of 0 eV, while the conduction band maximum corresponds to the band gap energy of diamond (5.49 eV). Only segments corresponding to the lowest-energy charge states are shown; the slope of these segments corresponds to the charge state ($q = +2, +1,\ 0, -1, -2$), and bends in the curves indicate transitions between different charge states as detailed in Figure 4.4 and 4.5 for the divacancy and substitutional lattice sites, respectively.

	DIVACANCY			SUBSTITUTIONAL			HEXAGONAL INTERSTITIAL			TETRAHEDRAL INTERSTITIAL		
	B-doped	N-doped	P-doped	B-doped	N-doped	P-doped	B-doped	N-doped	P-doped	B-doped	N-doped	P-doped
Sc^{+2}	**6.11**	13.15	15.15	**8.95**	15.99	17.99	**17.33**	24.37	26.37	**17.08**	24.12	26.12
Sc^{+1}	6.87	10.39	11.39	10.04	13.56	14.56	18.03	21.55	22.55	17.99	21.51	22.51
Sc^{0}	8.21	8.21	8.21	11.59	11.59	11.59	22.22	22.22	22.22	20.82	20.82	20.82
Sc^{-1}	10.87	7.35	6.35	14.25	**10.73**	**9.73**	24.02	**20.50**	19.50	23.50	**19.98**	**18.98**
Sc^{-2}	13.68	**6.64**	**4.64**	19.87	12.83	10.83	28.33	21.29	**19.29**	28.28	21.24	19.24
Ti^{+2}	**5.32**	12.36	14.36	**7.39**	14.43	16.43	16.11	23.15	25.15	**13.17**	20.21	22.21
Ti^{+1}	6.22	9.74	10.74	7.98	11.50	12.50	**15.37**	18.89	19.89	15.22	18.74	19.74
Ti^{0}	7.44	7.44	7.44	8.81	**8.81**	8.81	21.14	21.14	21.14	16.92	**16.92**	16.92
Ti^{-1}	9.46	5.94	4.94	13.43	9.91	**8.91**	20.89	**17.37**	16.37	20.96	17.44	**16.44**
Ti^{-2}	12.54	**5.50**	**3.50**	19.59	12.55	10.55	24.49	17.45	**15.45**	29.43	22.39	20.39

Table 4.1: Formation energies of isolated 3*d* transition metal impurities (Sc and Ti) at divacancy, substitutional, hexagonal interstitial and tetrahedral interstitial lattice sites in diamond calculated for different charge states ($q = +2, +1, 0, -1, -2$). The formation energies are calculated in *p*-type and *n*-type diamond at different Fermi levels pinned to acceptor/donor levels of B ($E_V + 0.37$ eV), and N ($E_C - 1.6$ eV) or P ($E_C - 0.6$ eV) doping, respectively. Lowest formation energies in each type of diamond doping are indicated in bold.

	DIVACANCY			SUBSTITUTIONAL			HEXAGONAL INTERSTITIAL			TETRAHEDRAL INTERSTITIAL		
	B-doped	N-doped	P-doped	B-doped	N-doped	P-doped	B-doped	N-doped	P-doped	B-doped	N-doped	P-doped
V^{+2}	**6.63**	13.67	15.67	**6.58**	13.62	15.62	12.60	19.64	21.64	13.64	20.68	22.68
V^{+1}	6.82	10.34	11.34	6.89	10.41	11.41	17.71	21.23	22.23	**13.61**	17.13	18.13
V^{0}	7.38	7.38	7.38	9.04	**9.04**	9.04	**16.20**	16.20	16.20	16.27	16.27	16.27
V^{-1}	9.23	**5.71**	4.71	12.60	9.08	**8.08**	19.19	**15.67**	**14.67**	19.24	**15.72**	**14.72**
V^{-2}	13.09	6.05	**4.05**	18.10	11.06	9.06	23.97	16.93	14.93	23.97	16.93	14.93
Cr^{+2}	**6.54**	13.58	15.58	**6.79**	13.83	15.83	**12.77**	19.81	21.81	**12.30**	19.34	21.34
Cr^{+1}	6.71	10.23	11.23	7.02	10.54	11.54	16.30	19.82	20.82	13.49	17.01	18.01
Cr^{0}	7.29	7.29	7.29	7.84	**7.84**	7.84	14.99	**14.99**	14.99	14.95	**14.95**	14.95
Cr^{-1}	9.11	5.59	4.59	12.15	8.63	**7.63**	19.06	15.54	**14.54**	19.38	15.86	**14.86**
Cr^{-2}	12.13	**5.09**	**3.09**	17.00	9.96	7.96	29.32	22.28	20.28	24.88	17.84	15.84

Table 4.1 (Continued): Formation energies of isolated 3*d* transition metal impurities (V and Cr) at divacancy, substitutional, hexagonal interstitial and tetrahedral interstitial lattice sites in diamond calculated for different charge states ($q = +2, +1, 0, -1, -2$). The formation energies are calculated in *p*-type and *n*-type diamond at different Fermi levels pinned to acceptor/donor levels of B ($E_V + 0.37$ eV), and N ($E_C - 1.6$ eV) or P ($E_C - 0.6$ eV) doping, respectively. Lowest formation energies in each type of diamond doping are indicated in bold.

	DIVACANCY			SUBSTITUTIONAL			HEXAGONAL INTERSTITIAL			TETRAHEDRAL INTERSTITIAL		
	B-doped	N-doped	P-doped	B-doped	N-doped	P-doped	B-doped	N-doped	P-doped	B-doped	N-doped	P-doped
Mn^{+2}	**2.34**	9.38	11.38	6.72	13.76	15.76	**11.25**	18.29	20.29	**8.98**	16.02	18.02
Mn^{+1}	2.68	6.20	7.20	**3.23**	6.75	7.75	12.76	16.28	17.28	10.87	14.39	15.39
Mn^{0}	3.33	3.33	3.33	4.25	4.25	4.25	11.95	**11.95**	11.95	12.31	12.31	12.31
Mn^{-1}	5.19	1.67	0.67	7.38	**3.86**	**2.86**	15.55	12.03	11.03	15.52	**12.00**	11.00
Mn^{-2}	7.17	**0.13**	**-1.87**	12.60	5.56	3.56	19.77	12.73	**10.73**	19.78	12.74	**10.74**
Fe^{+2}	6.42	13.46	15.46	**5.62**	12.66	14.66	**13.94**	20.98	22.98	**11.49**	18.53	20.53
Fe^{+1}	**6.04**	9.56	10.56	**5.62**	9.14	10.14	15.01	18.53	19.53	12.30	15.82	16.82
Fe^{0}	6.54	6.54	6.54	6.23	**6.23**	6.23	16.60	16.60	16.60	14.96	14.96	14.96
Fe^{-1}	8.90	5.38	4.38	10.50	6.98	**5.98**	20.63	17.11	16.11	17.75	**14.23**	**13.23**
Fe^{-2}	10.72	**3.68**	**1.68**	15.25	8.21	6.21	21.97	**14.93**	**12.93**	22.65	15.61	13.61

Table 4.1 (Continued): Formation energies of isolated 3*d* transition metal impurities (Mn and Fe) at divacancy, substitutional, hexagonal interstitial and tetrahedral interstitial lattice sites in diamond calculated for different charge states ($q = +2, +1, 0, -1, -2$). The formation energies are calculated in *p*-type and *n*-type diamond at different Fermi levels pinned to acceptor/donor levels of B ($E_V + 0.37$ eV), and N ($E_C - 1.6$ eV) or P ($E_C - 0.6$ eV) doping, respectively. Lowest formation energies in each type of diamond doping are indicated in bold.

	DIVACANCY			SUBSTITUTIONAL			HEXAGONAL INTERSTITIAL			TETRAHEDRAL INTERSTITIAL		
	B-doped	N-doped	P-doped	B-doped	N-doped	P-doped	B-doped	N-doped	P-doped	B-doped	N-doped	P-doped
Co^{+2}	5.81	12.85	14.85	4.46	11.50	13.50	**13.73**	20.77	22.77	**12.30**	19.34	21.34
Co^{+1}	**5.27**	8.79	9.79	**4.30**	7.82	8.82	14.21	17.73	18.73	13.22	16.74	17.74
Co^{0}	5.96	5.96	5.96	6.75	**6.75**	6.75	16.47	16.47	16.47	14.69	**14.69**	14.69
Co^{-1}	7.84	4.32	3.32	10.66	7.14	6.14	17.66	**14.14**	**13.14**	18.44	14.92	**13.92**
Co^{-2}	9.73	**2.69**	**0.69**	14.68	7.64	**5.64**	22.91	15.87	13.87	24.16	17.12	15.12
Ni^{+2}	**5.38**	12.42	14.42	**4.57**	11.61	13.61	**12.88**	19.92	21.92	**13.12**	20.16	22.16
Ni^{+1}	5.51	9.03	10.03	6.07	9.59	10.59	14.08	17.60	18.60	13.92	17.44	18.44
Ni^{0}	5.96	5.96	5.96	8.07	8.07	8.07	15.79	**15.79**	15.79	15.26	**15.26**	**15.26**
Ni^{-1}	7.53	4.01	3.01	11.22	**7.70**	6.70	19.86	16.34	**15.34**	20.46	16.94	15.94
Ni^{-2}	9.22	**2.18**	**0.18**	15.25	8.21	**6.21**	24.46	17.42	15.42	25.47	18.43	16.43

Table 4.1 (Continued): Formation energies of isolated 3*d* transition metal impurities (Co and Ni) at divacancy, substitutional, hexagonal interstitial and tetrahedral interstitial lattice sites in diamond calculated for different charge states ($q = +2, +1, 0, -1, -2$). The formation energies are calculated in *p*-type and *n*-type diamond at different Fermi levels pinned to acceptor/donor levels of B ($E_V + 0.37$ eV), and N ($E_C - 1.6$ eV) or P ($E_C - 0.6$ eV) doping, respectively. Lowest formation energies in each type of diamond doping are indicated in bold.

	DIVACANCY			SUBSTITUTIONAL			HEXAGONAL INTERSTITIAL			TETRAHEDRAL INTERSTITIAL		
	B-doped	N-doped	P-doped	B-doped	N-doped	P-doped	B-doped	N-doped	P-doped	B-doped	N-doped	P-doped
Cu^{+2}	**6.03**	13.07	15.07	**6.67**	13.71	15.71	**14.11**	21.15	23.15	**13.81**	20.85	22.85
Cu^{+1}	6.28	9.80	10.80	7.90	11.42	12.42	14.67	18.19	19.19	14.24	**17.76**	18.76
Cu^{0}	6.71	6.71	6.71	9.38	9.38	9.38	17.76	**17.76**	17.76	17.90	17.90	**17.90**
Cu^{-1}	8.30	**4.78**	3.78	12.28	8.76	7.76	21.74	18.22	**17.22**	24.53	21.01	20.01
Cu^{-2}	12.02	4.98	**2.98**	15.73	**8.69**	**6.69**	27.04	20.00	18.00	30.21	23.17	21.17
Zn^{+2}	**6.43**	13.47	15.47	**7.64**	14.68	16.68	**14.88**	21.92	23.92	**14.09**	21.13	23.13
Zn^{+1}	6.72	10.24	11.24	8.56	12.08	13.08	17.48	21.00	22.00	17.08	20.60	21.60
Zn^{0}	7.21	7.21	7.21	9.72	9.72	9.72	20.28	**20.28**	20.28	20.07	**20.07**	20.07
Zn^{-1}	10.09	6.57	5.57	12.11	8.59	7.59	24.33	20.81	**19.81**	24.29	20.77	19.77
Zn^{-2}	13.24	**6.20**	**4.20**	14.78	**7.74**	**5.74**	29.40	22.36	20.36	28.80	21.76	**19.76**

Table 4.1 (Continued): Formation energies of isolated 3*d* transition metal impurities (Cu and Zn) at divacancy, substitutional, hexagonal interstitial and tetrahedral interstitial lattice sites in diamond calculated for different charge states ($q = +2, +1, 0, -1, -2$). The formation energies are calculated in *p*-type and *n*-type diamond at different Fermi levels pinned to acceptor/donor levels of B ($E_V + 0.37$ eV), and N ($E_C - 1.6$ eV) or P ($E_C - 0.6$ eV) doping, respectively. Lowest formation energies in each type of diamond doping are indicated in bold.

4.3 Charge transition levels

The Fermi energy at which a defect changes from one charge state (q_1) to another (q_2) represents a thermodynamic charge transition (or ionization) level, denoted as $\varepsilon_F(q_1/q_2)$, and the transition occurs at the position of the Fermi level at which the two charge states have equal formation energies, as discussed in Section 2.4.2.

Experimentally, defect ionization levels created by transition metals and their complexes in semiconductors have been studied using a wide range of techniques, including DLTS, EPR and diffusion measurements. On the other hand, theoretical predictions using DFT methods have been used to provide a detailed understanding of transition metal defects in a number of semiconductors, and agreement of predicted donor/acceptor levels with experimental results is often achieved. In some cases, however, agreement between DFT and experimental results has been found to be weaker, mainly due to the inherent problem of band gap underestimation by DFT methods − an underestimation often marked by the conduction band minimum set lower than the actual value (calculated in the present study to be 12.4% lower compared to the experimental value of 5.49 eV). In addition, discrepancies between theoretical and experimental results may be attributed the fact that DFT calculations are carried out at 0 K. For example in silicon, acceptor ionization energies, which track the temperature variation of the conduction band minimum have been found to move from their 0 K positions by at least 0.4 eV at 1200 K [195]. Nevertheless, theoretical results have been found to provide a reliable qualitative illustration of chemical trends (and in some cases, quantitative estimates) in defect ionization energy levels for many technologically useful semiconducting materials [195].

4.3.1 Trends in ionization levels across the 3*d* series

Figure 4.4 illustrates the calculated thermodynamic charge transition levels of 3*d* transition metals in diamond (with respect to the valence band maximum and conduction band minimum) at divacancy and substitutional lattice sites, for the charge states q = +2, +1, 0, -1, -2. It is important to note that these transition levels are for the most stable symmetries of the lowest energy charge states in the diamond band gap, and therefore the Kohn-Sham single particle trend across the series will be altered since different charge states attains different symmetries after geometry optimization, as will be shown in Chapter five. It is seen that all the 3*d* series transition metals induce both donor and acceptor levels in the diamond band

gap, and their positions in the band gap reveal a characteristic trend with the number of *d* electrons across the series – a pattern known from atomic spectra but considerably flattened out in solids due to screening and hybridization effects [196]. Consequently, the majority of defect levels for substitutional transition metals are generally found to exhibit relatively large energy splitting compared to the divacancy site. In addition, acceptor ionization levels for early substitutional transition metals are seen to occur closer to the conduction band (or as resonances inside the conduction band) compared to divacancy transition metals. This result is indicative of the large outward carbon nearest neighbour relaxations at the substitutional site as evidenced by the respective higher formation energies compared to the divacancy site.

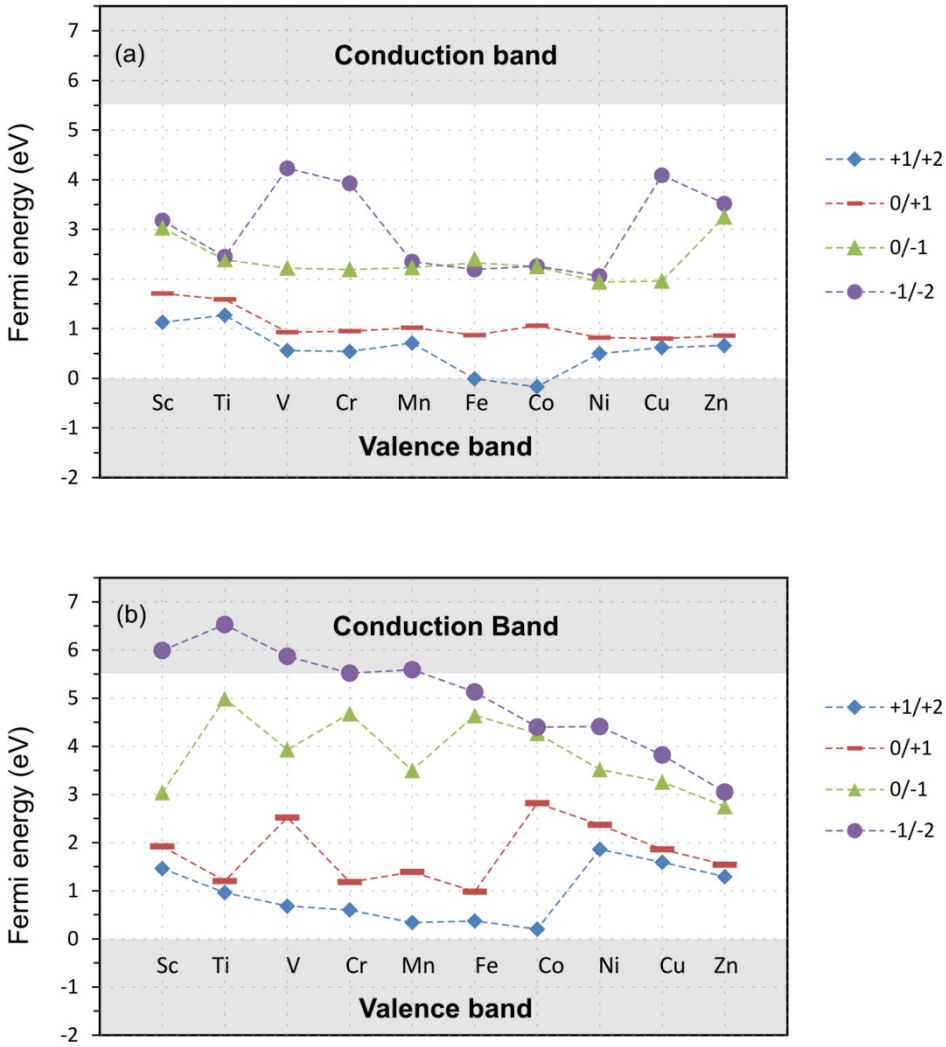

Figure 4.4: Trends of thermodynamic charge transition levels for the most stable symmetries of 3*d* transition metals at (a) divacancy and (b) substitutional lattice site sites in diamond, relative to the valence band maximum and conduction band minimum. Data points correspond to transition energies, while the line shows trends across the series.

4.3.2 Band gap levels

It is well known that doping semiconductor crystals creates defect levels in the band gap, thus shifting the Fermi level from the intrinsic position. However, this is true in general for narrow band gap semiconductors such as Si. For diamond and other wide band gap semiconductors, however, the Fermi level is often not well defined. Therefore, not only are the defect levels of transition metal impurities are being considered here, but also the impact of Fermi level pinning by other majority dopants (such as boron, phosphorus or nitrogen) and the effect of this on the energetic stability of different charge states and other properties of the 3*d* transition metal dopants in diamond.

From Figure 4.4, it is evident that the majority of 3*d* transition metals induce deep donor and acceptor impurity levels in the diamond band gap, thus highlighting the fact that their electronic and magnetic properties in diamond will be strongly dependent on their charge state, and hence on the position of the Fermi level in the diamond band gap. Hence, the electronic or magnetic properties of these defects may be activated (or deactivated) by co-doping with shallow donors (e.g. phosphorus) or acceptors (e.g. boron), thereby fixing the Fermi level of the system to a particular charge state. It should be noted that the ensuing Fermi level and the type of conductivity will be determined by the majority dopant, and the thermodynamic Fermi level in turn will determine the electronic configuration of the transition metal defect, related to a nominal oxidation state [197]. Considering spintronic applications, the different oxidation states of the 3*d* impurities may correspond to different spin configurations, which may at the same time advantageously give rise to collective ferromagnetism in diamond upon 3*d*-3*d* spin coupling interactions, as will be discussed in Chapter six.

The deep nature of the band gap levels induced by the transition metal defects in diamond is particularly important in achieving highly localized and controllable quantum states well isolated from decoherence sources (which often arises from strong coupling to the bulk valence and conduction band sates [8,129]), similar to the well-known $(N\text{-}V)^{-1}$ centre in diamond which is currently among the leading candidates being considered for spintronic and quantum computing applications [129]. However, since most of calculated transition metal donor/acceptor levels are deep within the diamond band gap, ionizing them may not occur thermally, but will require, extrinsic electron/hole doping from shallower donors or acceptors, respectively. Considering the “killer effect” [198] of such dopants, it is noted from Figure 4.4

that the acceptor transitions (0/+1 and +1/+2) occur in the lower part of the diamond band gap, while donor transitions (0/-1 and -/-2) occur in the upper part of the band gap, and therefore such additional impurities will not act as compensation centres, but will rather result in an increase of carrier concentration, which has been demonstrated to play a key role in mediating ferromagnetic spin interactions in other semiconductors [199-201].

4.3.3 Band resonance levels

A characteristic feature of shallow impurities when calculated using the supercell approach is that localized defect states may not occur inside the band gap, but rather as resonances inside the conduction bands [197,202] due to the well known problem of band gap underestimation by DFT methods. We find this to be the case in (-1/-2) acceptor transitions for Sc ($E_C + 0.5$ eV), Ti ($E_C + 1.04$ eV), V ($E_C + 0.38$ eV), Cr ($E_C + 0.08$ eV) and Mn ($E_C + 0.1$ eV) at the substitutional site, and (+1/+2) donor transition for Co ($E_V - 0.01$ eV) and Fe ($E_V - 0.17$ eV) at the divacancy site, as shown in Figure 4.4.

These results are generally similar to what has previously been obtained for transition metal-doped ZnO [197], and can be attributed to the Moss-Burstein effect [203,204] arising from high transition metal impurity concentration. Thus, donor or acceptor transitions of shallow impurities are calculated just above the conduction band or below the valence band, respectively, due to band filling-effects. While such effects may be corrected (by use of large supercells) to give better estimates of the actual transition levels for the dilute doping limit, it should be noted that DMS in general require relatively high impurity concentrations to instigate ferromagnetic exchange [91]. Therefore, defect levels located inside the conduction or valence bands are indicators for shallow donor or accepter levels; their experimentally observed transitions will likely correspond to hydrogenic like donor ($d^{N-1} + e$) or acceptor ($d^{N-1} + h$) levels located just below the conduction band or above the valence band, respectively, similar to recent observations in CdSe: Sc [205]. Whether the impurity bands associated with these donor or acceptor levels will be merged with the respective bands or decoupled from them is still a subject of controversy in Zener's model of hole meditated ferromagnetism [199,200].

Although many of the shallow donor/acceptor levels may not be occupied (depending on the position of the Fermi level), we note that the electronic bands associated with resonant donor

levels at the substitutional site, especially for V, Cr or Mn, whose resonant states are located just above the conduction band, may become partially occupied by additional shallow co-donor states (such as phosphorus) at high concentration [197,206], thus creating the required partial occupancy essential for carrier mediated ferromagnetism. At very high levels of donor co-dopant concentrations, the Fermi level in these cases will be pushed toward the empty *d* resonance inside the conduction band (due to Moss-Burstein shift [203,204]), thus creating partial occupation of the transition metal resonant states.

An important outcome of this result is that ferromagnetism in some transition metal-doped diamond may be mediated by electrons rather than holes, in contrast to manganese doped GaAs – which is generally considered the archetype diluted magnetic semiconductor – in which ferromagnetic order among the spins of isolated Mn atoms is widely believed to be mediated by holes.

Indeed, the possibility of electron mediated ferromagnetism has previously been explored in 3*d* transition metal-doped oxides (ZnO and In_2O_3) [197,201,207-209] with promising results of electron mediated ferromagnetism in Cr-doped ZnO [201]. However, it should be noted that for significant ferromagnetism to be observed, the individual 3*d* ions need to be close enough so as to interact, which in practice implies large concentrations of the impurity defects (well above the typical thermodynamic limits) and the presence of free charge carriers to facilitate ferromagnetic exchange interactions between the parent spins.

5. Electronic structure, spin and symmetry of 3*d* transition metals in diamond

5.1 Introduction

While there have been significant experimental and some theoretical efforts in the study of transition metal impurities in diamond, no systematic studies have been carried out to elucidate their electronic structure and spin properties for different charge states and lattice sites in diamond. We have shown in Chapter four that 3*d* transition metal impurities in diamond can generally assume different charge states, depending on the Fermi level position, and their properties when incorporated into diamond will depend on the charge state of the impurity defect.

In this Chapter, we therefore report *ab initio* DFT calculations on the symmetries, electronic structure and spin properties of 3*d* transition metals at various lattice sites and charge states in diamond, in order to establish a systematic insight of their magnetic ordering properties. A comparison of the present results with previous theoretical models on transition metal impurities will also discussed so as to establish reliable theoretical models for calculating the magnetic properties of these impurities in diamond.

The spin and symmetry models of 3*d* transition metals (Sc, Ti, V , Cr, Mn, Fe, Co, Ni, Cu, Zn) in diamond in the present study have been determined using a 64-atom fcc diamond supercell containing one transition metal impurity in various charge states $(+2,\ +1, 0, -1, -2)$ placed at the substitutional, divacancy or interstitial lattice sites, as discussed in Section 2.5. By symmetry, these structures will be ordered ferromagnetically if there exists a non-vanishing spin polarisation, since each cell contains a single transition metal impurity with an infinite number of identical periodic images. While such magnetic ordering may not necessarily correspond to the equilibrium magnetic ground state of the system, its existence generally indicates a possibility of collective magnetic ordering upon impurity-impurity interactions in the system.

5.2 Results and discussions

In order to find the most stable spin state corresponding to the structural energy minimum of transition metal-doped diamond, various initial spins of the transition metal atom (for each charge state and lattice site) were considered. We find that most transition metal impurities in diamond have more than one metastable magnetic solution; in order to find all such metastble states corresponding to all possible magnetic solutions, it is essential to systematically vary both the initial geometries and initial spins for each charge estate and lattice site.

As an example, Figure 5.1 shows the dependence of the total energy on the initial spin input for neutral vanadium calculated at the substitutional lattice site in diamond. The calculated magnetic moment and the optimized structural energy are seen to be strongly dependent on the metastable state found. Therefore, in order to find all such metastable states, a wide range of initial spins should be considered, since the final spin state of a system attained after spin optimization does not necessarily correspond to the initial spin state.

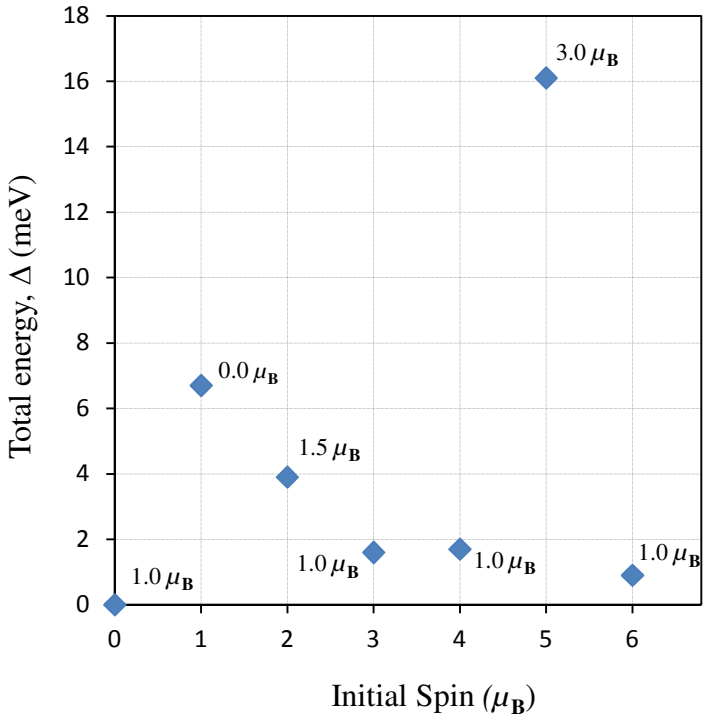

Figure 5.1: Optimized spin values as a function of initial spin per supercell for substitutional vanadium (q = 0) in diamond. The energy axis is given relative to the lowest energy structure, while data point labels are the optimized final spin states corresponding to the respective initial spins.

5.2.1 Effects of Non-Linear Core Correction

When using pseudopotential approximations, the application of Non–Linear Core Correction (NLCC) to the exchange and correlation potential (in some atomic systems [210]) is necessary for accurate determination of magnetic properties in spin-polarised systems [211], as discussed in Section 2.2.4. In order to ensure that the calculated magnetic moments were not dependent on the pseudopotential valence configuration, we performed similar calculations with and without NLCC, but differences on the results of the calculated spin densities were found to be negligible (less than 0.01 μ_B), while energy differences and geometries remained unchanged. However, we found that incorporation of NLCC to the pseudopotential valence configuration in Sc, Ti, V and Cr (as implemented in the CASTEP code [41]) resulted in a lower total energy per supercell (in the order of 1 eV) compared to bare pseudopotentials without non-linear core corrections, though energy differences between similar calculations remained the same.

Therefore, to ensure that the correct ground state magnetic moment was obtained, geometry optimization was first carried out using ultrasoft pseudopotentials without core corrections, after which the optimized structures were used to optimize the spin density by using non-linear core corrections to the valence configurations, except for Cu and Zn where NLCC pseudopotentials were not available in the CASTEP computational code (version 5.0.1) [41] used in the present study. In order to confirm the reliability of this pseudopotential approach, and to verify the calculated magnetic moments obtained from the pseudopotential technique, comparative calculations using all electron full-potential methods as implemented in the WIEN2k code [46] were performed for selected cases (Cr^0, Ni^0, and Co^0) and the results of both the full-potential reference calculations and the corresponding pseudopotential calculations were found to be in good agreement, thus validating the reliability of the pseudopotential technique in calculating the properties of magnetic systems.

5.2.2 Geometry relaxation effects

Geometry relaxation in electronic structure calculations ensures that accurate descriptions of the system's electronic structure, including all other properties which are dependent on the total energy of the system (e.g. forces and lattice constants) are obtained. As illustrated in Figure 5.5, we find that early (Sc, Ti) and late (Ni, Cu, Zn) transition metals in various charge states at the divacancy site introduce larger outward relaxations to the carbon neighbours,

resulting in low or zero spin states, whereas transition metals in the middle of the series (V, Cr, Mn, Fe, Co) introduce smaller relaxations resulting in high spin states, similar to previous calculations in transition metal-doped GaAs [212]. These results relate qualitatively to the formation energy trends discussed in Chapter four, as well as to trends in atomic radii across the 3*d* series. The atomic radii in relation to the carbon-carbon bond length for the early and late transition metals are relatively larger compared to middle transition metals, and therefore for transition metals in the middle of the 3*d* series, the exchange splitting dominates over the hexagonal crystal field of the divacancy, while the situation is reversed for early and late transition metals. On the other hand, the strong tetrahedral crystal field dominates over the exchange splitting at the substitutional site due to large carbon neighbour relaxations compared to the divacancy site.

Table 5.1 summarizes the quantitative effect of geometry relaxation on the calculated magnetic moment and the corresponding relaxation energies for 3*d* transition metals in diamond at the substitutional and divacancy sites. In each case, the magnetic moments are given, both with and without, geometry relaxation. At the divacancy site, we find that geometry optimization reduces the magnetic moment, while it has no effect on the magnetic moment at the substitutional site, except for Zn in which the magnetic moment of the relaxed structure is $2.0\mu_B$ compared to 1.5 μ_B when unrelaxed. Further, we find that the relaxation energy, which is the energy difference between the relaxed and unrelaxed structures, leads to

	(a) Divacancy site			**(b) Substitutional site**		
TM	Relaxed MM (μ_B)	Unrelaxed MM (μ_B)	ΔE (eV)	Relaxed MM (μ_B)	Unrelaxed MM (μ_B)	ΔE (eV)
Sc	0.44	0.69	-2.84	1.00	1.00	-12.21
Ti	1.44	1.50	-1.69	0.00	0.00	-10.69
V	1.50	1.69	-1.38	1.00	1.00	-8.10
Cr	2.50	2.50	-1.12	2.00	2.00	-6.62
Mn	3.31	3.69	-1.08	1.00	1.00	-3.33
Fe	1.26	1.12	-0.72	0.00	0.00	-4.39
Ni	1.25	1.25	-0.70	2.00	2.00	-5.56
Cu	0.13	0.37	-0.85	3.00	3.00	-6.34
Zn	0.00	0.00	-1.14	2.00	1.50	-7.45

Table 5.1: Magnetic moments (MM) of 3*d* transition metals (TM) in diamond at (a) divacancy and (b) substitutional lattice sites calculated with and without geometry relaxation using a 64-atom diamond supercell. ΔE is the respective relaxation energy, i.e. the energy difference between relaxed and unrelaxed supercells.

significant structural stabilization at both lattice sites, with the elongation of the carbon neighbours being significant only up to the second nearest neighbours. The relaxation energy trend depicted across the 3*d* series is consistent with the trend in the atomic radius, and can be explained by considering that as the transition metal decreases in size, it fits better in the respective lattice site which results in a corresponding decrease in the overall crystal strain of the lattice.

5.2.3 Structural properties

The optimized lattice constant of diamond was found to be 3.569Å, which is in close agreement with the experimental value of 3.567 Å [6] – considering that the commonly used exchange-correlation approximations (LDA and GGA) often introduce errors of up to a few percent to structural properties, including the lattice constant of semiconductors. In the present calculations, the GGA approximation was used, and it should be noted that GGA is known to give the correct natural phase stability [213,214], and considerably reduces the error on lattice constants compared to L(S)DA [215].

To ensure that the final optimized geometries were not dependent on the initial symmetry, the transition metal atom for each of the lattice sites and charge states was initially displaced randomly from the ideal high symmetry point. After complete geometry optimization, the carbon neighbours of the transition metal impurities at each lattice site were found to relax outwards because of the large atomic radius of the transition metal atom compared to a carbon atom, with the unique transition metal-carbon bond lengths across the series elongating by $1-14$ Å and $5-40$ Å at the divacancy and substitutional lattice sites, respectively.

Table 5.2 presents a summary of the local point symmetries and nearest carbon neighbour relaxations, together with the induced magnetic moments at the substitutional and divacancy sites. For symmetry-preserving relaxations, the trend across the 3*d* transition metal series closely follows that of the calculated formation energies discussed in Chapter four, with the transition metal-carbon bond length elongation being larger for elements earlier or later in the 3*d* series, compared to those in the middle of the series for any charge state or lattice site. At the substitutional site, a transition metal atom replaces one carbon atom so that each transition metal impurity is surrounded by four nearest carbon neighbours. The majority of

substitutional transition metals in the various charge states were found to relax back to the lattice site after geometry optimization, with the four carbon neighbours equidistantly positioned to form tetrahedral symmetry (T_d). In addition, other lower symmetry distortions, including C_{2v} (a two-fold axis and vertical mirror plane distortion) for Sc^{+2} and $Mn^{+2,}$ C_s (a distortion with a mirror plane as the only symmetry element) for Sc^{+}, Sc^{0} and Ti^{+2} and C_{3v} in Ti^{+}, Ti^{0}, V^{+2}, V^{+}, Cr^{+2}, Fe^{-} and Co^{0} were found, and can be explained as arising from symmetry breaking distortions of the crystal field. Figure 5.2 illustrates a schematic representation of the displacement of the four nearest carbon neighbour atoms around the transition metal impurity decomposed into two parts: a symmetric radial relaxation component for the T_d symmetry relaxation and a symmetry breaking component for C_{2v} and C_{3v} symmetry relaxations.

In contrast to the substitutional site, a transition metal atom at the divacancy site occupies the mid-point between two neighbouring carbon vacancies, and each transition metal impurity is surrounded by six nearest carbon neighbours. The two missing carbon atoms at the divacancy increases the atomic volume around the transition metal atom, thus causing much less crystal strain compared to a substitutional site. After geometry optimization, we found that the majority of transition metals in the various charge states relax back to the centre of the divacancy, resulting in D_{3d} symmetry. In addition to this high symmetry geometry, other lower symmetry distortions, including C_2 (a two-fold axis symmetry distortion) for V^{+}, V^{-}, Fe^{+}, Co^{0}, Co^{-2} , C_{2h} (a two-fold axis and a horizontal mirror plane symmetry distortion) for T^{+}, Ti^{0}, V^{+2} and C_s for V^{0}, Cr^{+}, Cr^{0}, Co^{+}, Co^{-} were also found.

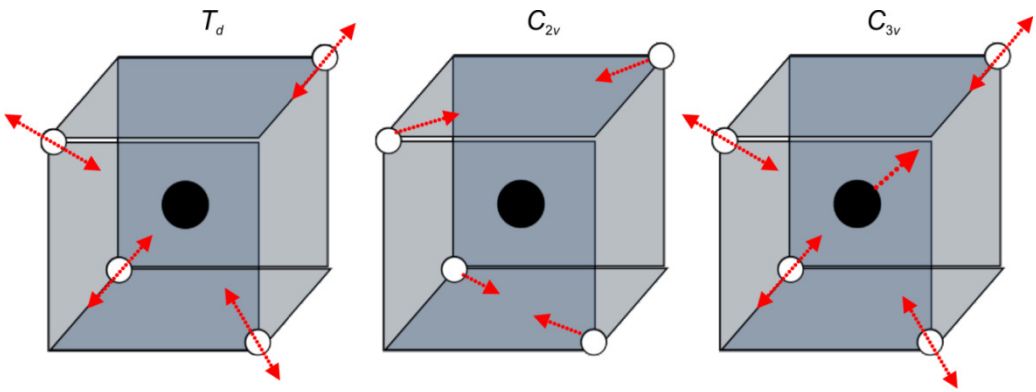

Figure 5.2: Schematic representation of the formation of T_d symmetry distortion, together with C_{2v} and C_{3v} distortions for transition metals at a substitutional lattice site in diamond. The arrows indicate the direction of displacement of the four nearest neighbour carbon atoms (white balls) with respect to the transition metal atoms (black balls).

(a) DIVACANCY SITE

TM ion	MM (Total)	Point symmetry	NN-distortions (Å)	Unique NN-relaxation (%)
Sc^{+2}	0.1	D_{3d}	0.18(6)	9.3
Sc^{+1}	0.0	D_{3d}	0.18(6)	9.2
Sc^{0}	0.4	D_{3d}	0.16(6)	8.2
Sc^{-1}	1.4	D_{3d}	0.16(6)	8.4
Sc^{-2}	0.6	D_{3d}	0.15(6)	7.6
Ti^{+2}	0.0	D_{3d}	0.14(6)	7.4
Ti^{+1}	0.4	C_{2h}	0.14(6)	7.2
Ti^{0}	1.4	C_{2h}	0.12(6)	6.2
Ti^{-1}	0.2	D_{3d}	0.12(6)	6.3
Ti^{-2}	0.0	D_{3d}	0.10(6)	5.4
V^{+2}	1.0	C_{2h}	0.13(6)	7.0
V^{+1}	1.9	C_2	0.24(2), 0.12(2), 0.02(2)	12.5
V^{0}	1.0	C_S	-0.75,0.25, 0.23, -0.04 (3)	13.0
V^{-1}	0.0	C_2	0.24(2), 0.10(2), -0.02(2)	12.3
V^{-2}	1.2	D_{3d}	0.09(6)	04.6
Cr^{+2}	2.5	D_{3d}	0.12(6)	06.6
Cr^{+1}	3.0	Cs	0.27, 0.16(2), 0.06(2), -0.03	14.0
Cr^{0}	2.0	C_S	0.23, 0.22(2), -0.05, -0.01(2)	11.2
Cr^{-1}	1.0	D_{3d}	0.10(6)	5.0
Cr^{-2}	2.5	D_{3d}	0.08 (6)	4.0
Mn^{+2}	3.0	D_{3d}	0.12(6)	6.3
Mn^{+1}	2.5	D_{3d}	0.11(6)	5.5
Mn^{0}	3.0	D_{3d}	0.09(6)	4.7
Mn^{-1}	3.2	D_{3d}	0.08(6)	4.0
Mn^{-2}	3.0	D_{3d}	0.06(6)	3.3

(b) SUBSTITUTIONAL SITE

TM ion	MM (Total)	Point symmetry	NN-distortions (Å)	Unique NN-relaxation (%)
Sc^{+2}	1.0	C_{2v}		33.4
Sc^{+1}	0.0	C_s	0.46(2), 0.34(2)	29.9
Sc^{0}	1.0	C_s	0.48, 0.36, 0.31(2)	31.1
Sc^{-1}	0.0	T_d	0.38(4)	24.1
Sc^{-2}	0.3	T_d	0.35(4)	22.5
Ti^{+2}	0.0	C_s	0.49, 0.32, 0.28(2)	31.4
Ti^{+1}	1.0	C_{3v}	0.50, 0.30(3)	32.5
Ti^{0}	0.0	C_{3v}	0.248(3)	35.0
Ti^{-1}	1.0	T_d	0.322(3)	20.9
Ti^{-2}	0.0	C_s	0.56, 0.31(2), 0.13	36.2
V^{+2}	0.1	C_{3v}	0.57, 0.22(3)	36.9
V^{+1}	0.0	C_{3v}	0.53, 0.25(3)	34.4
V^{0}	1.0	T_d	0.26(4)	16.8
V^{-1}	2.0	T_d	0.29(4)	19.0
V^{-2}	1.8	T_d	0.27(4)	17.3
Cr^{+2}	0.5	C_{3v}	0.24(3), 0.23	15.4
Cr^{+1}	1.0	T_d	0.26(4)	16.9
Cr^{0}	2.0	T_d	0.24(4)	15.5
Cr^{-1}	1.0	T_d	0.25(4)	16.4
Cr^{-2}	0.0	T_d	0.22(4)	14.4
Mn^{+2}	1.0	C_{2v}	0.55(2), 0.16(2)	35.8
Mn^{+1}	0.0	T_d	0.24(4)	15.5
Mn^{0}	1.0	T_d	0.23(4)	4.9
Mn^{-1}	0.0	T_d	0.22(4)	14.3
Mn^{-2}	0.3	T_d	0.23(4)	14.8

Table 5.2: A summary of the optimized local point symmetries and nearest carbon neighbour (NN)-distortions, together with the induced magnetic moments (MM) for Sc to Mn at (a) divacancy and (b) substitutional sites in diamond. Numbers in brackets after NN-distortions values indicates the multiplicity of each bondlength.

(a) DIVACANCY SITE

TM ion	MM (Total)	Point symmetry	NN-distortions (Å)	Unique NN-relaxation (%)
Fe^{+2}	2.0	D_{3d}	0.10(6)	5.4
Fe^{+1}	1.0	C_2	0.24(2), 0.09(2), -0.05(2)	12.1
Fe^{0}	0.0	C_1	0.20(2), 0.07, 0.06, -0.050(2)	10.0
Fe^{-1}	1.8	D_{3d}	0.05(6)	02.7
Fe^{-2}	2.0	D_{3d}	0.04(6)	1.9
Co^{+2}	1.0	D_{3d}	0.10(6)	05.1
Co^{+1}	0.0	C_s	0.26, 0.16(2), 0.01(2), -0.07	13.3
Co^{0}	0.5	C_2	0.17(2), 0.07(2), -0.04(2)	08.9
Co^{-1}	1.5	C_s	0.13, 0.08(2), 0.02(2), -0.03	06.4
Co^{-2}	1.0	C_2	0.07(2), 0.03(2), -0.00 (2)	03.4
Ni^{+2}	0.0	D_{3d}	0.10(6)	5.1
Ni^{+1}	0.3	-	-	-
Ni^{0}	0.0	D_{3d}	0.06(6)	3.1
Ni^{-1}	0.5	-	-	-
Ni^{-2}	0.0	D_{3d}	0.02(6)	1.0
Cu^{+2}	0.3	D_{3d}	0.11(6)	5.6
Cu^{+1}	0.3	-	-	-
Cu^{0}	0.0	D_{3d}	0.06(6)	3.3
Cu^{-1}	0.0	-	-	-
Cu^{-2}	1.0	D_{3d}	0.05(6)	2.0
Zn^{+2}	0.1	D_{3d}	0.13(6)	6.5
Zn^{+1}	0.1	-	-	-
Zn^{0}	0.0	D_{3d}	0.08(6)	4.0
Zn^{-1}	1.0	-	-	-
Zn^{-2}	1.8	D_{3d}	0.08(6)	4.3

(b) SUBSTITUTIONAL SITE

TM ion	MM (Total)	Point symmetry	NN-distortions (Å)	Unique NN-relaxation (%)
Fe^{+2}	1.8	T_d	0.22(4)	14.3
Fe^{+1}	1.0	T_d	0.21(4)	13.5
Fe^{0}	0.0	T_d	0.19(4)	12.3
Fe^{-1}	1.0	C_{3v}	0.20(3), 0.94	13.1
Fe^{-2}	2.0	T_d	0.21(4)	13.7
Co^{+2}	0.3	T_d	0.21(4)	13.7
Co^{+1}	0.0	T_d	0.21(4)	13.6
Co^{0}	1.0	C_{3v}	0.22(3), 0.21	14.2
Co^{-1}	0.0	T_d	0.22(4)	14.1
Co^{-2}	3.0	T_d	0.23(4)	14.8
Ni^{+2}	0.0	T_d	0.23(4)	15.0
Ni^{+1}	0.5	T_d	0.23(4)	14.8
Ni^{0}	2.0	T_d	0.23(4)	14.9
Ni^{-1}	3.0	T_d	0.27(4)	14.7
Ni^{-2}	2.0	T_d	0.23(4)	15.0
Cu^{+2}	0.5	T_d	0.26(4)	16.9
Cu^{+1}	0.4	T_d	0.25(4)	16.4
Cu^{0}	3.0	T_d	0.24(4)	15.5
Cu^{-1}	2.0	T_d	0.24(4)	15.4
Cu^{-2}	1.0	T_d	0.24(4)	15.4
Zn^{+2}	0.0	T_d	0.29(4)	18.5
Zn^{+1}	1.5	T_d	0.27(4)	17.8
Zn^{0}	2.0	T_d	0.26(4)	16.8
Zn^{-1}	1.0	T_d	0.25(4)	16.2
Zn^{-2}	1.8	T_d	0.24(4)	15.8

Table 5.2: (continued): A summary of the optimized local point symmetries and nearest carbon neighbour (NN)-distortions, together with the induced magnetic moments (MM) for Sc to Mn at (a) divacancy and (b) substitutional sites in diamond. Numbers in brackets after NN-distortions values indicates the multiplicity of each bondlength.

5.2.4 Electronic structure

5.2.4.1 Density of states

Figure 5.3 illustrates spin-up and spin-down density of states (DOS) at the divacancy and substitutional lattice sites for each of the 3*d* transition metals in the neutral charge state in a 64-atom diamond supercell. The corresponding spin polarised band structures are shown in Figure 5.4. To enhance ferromagnetic exchange, practical diluted magnetic semiconductors often require high impurity concentrations beyond the thermodynamic limit and thus band broadening of the impurity band, together with hybridization between defects and image interactions may result in both qualitative and quantitative differences between the calculated DOS and the Kohn-Sham quasi-particle level splitting [91].

As discussed in Chapter four, incorporation of 3*d* transition metals into diamond induces impurity levels corresponding to different thermodynamic charge transitions in the diamond band gap due to perturbation of the crystal field. However, because of finite impurity concentrations, these impurity levels are broadened to form impurity bands (as opposed to what would be expected based on a one-electron model of non-interacting impurities) whose electronic structures can be predicted from interactions between the atomic orbitals of the transition metal and carbon atoms in diamond.

An empirical model by Ludwig and Woodbury (L-W) [216] predicts that the metallic 3*d* electrons of the transition metals are accommodated in a manner dictated by the symmetry and the lattice site occupied by the transition metal. An alternative model called the vacancy model [147] predicts that the transition metal's orbitals will be found deep inside the valence band and can be represented by vacancy-like bands, as the metal does not interact with the host. However, our results show that most 3*d* transition metals at both the divacancy and substitutional lattice sites in diamond effectively interact with the carbon atoms as demonstrated by the hybridization between the transition metal orbitals with carbon orbitals in the diamond band gap, in contradiction to the vacancy model. Although the L-W and vacancy models are extremes that are not encountered in practice (due to the presence of dangling bonds which arise when the transition metal disrupts the crystal structure), we find that most early and middle transition metals approach the L-W model (based on the energetic positions of the 3*d* peaks), while the late transition metals to a greater extent conform to the vacancy model, in agreement with previous results [186].

Across the $3d$ series, from Sc to Zn, we find that incorporation of transition metal impurities induces impurity bands into the diamond band gap while maintaining the semiconducting property of diamond, with band gaps in both spin channels. From the respective partial density of states (PDOS) shown in Figure 5.3, these impurity bands are seen to originate mainly from $s, p-d$ hybridization between carbon sp^3 orbitals with the $3d$ orbitals of the transition metal. In addition, we find that the $4p$ orbitals also contribute to hybridization for substitutional transition metals, but not at the divacancy site. Although the contribution of the $4p$ orbitals is relatively small compared to that of the $3d$ orbitals, their presence in the band gap is found to significantly affect the bonding interactions and thus the induced magnetic moments, as will be discussed in Section 5.2.5.

A comparison of the transition metal PDOS across the series (Figure 5.3) shows that the $3d$ main peaks are shifted gradually to lower energies with increasing $3d$ character, an observation that can be attributed to incomplete screening of the additional nuclear charge [186]; for example in Sc: [Ar] $3d^1 4s^2$ the d orbital is located closer to the conduction band at about 3.0 eV above the Fermi level, while in Cu: [Ar]$3d^{10}4s^1$ the d orbital is located deep inside the valence band at about 4.0 eV below the Fermi level, at both the substitutional and divacancy sites. For transition metals in the middle of the series (V, Cr, Mn, Co, Ni), the $3d$ impurity bands hybridize strongly with the diamond valence band edge and the majority appear as broad peaks inside the valence band. This result is particularly significant in carrier mediated ferromagnetism since these orbitals may hybridize with shallow acceptors (such as boron in diamond) to increase carrier concentration, and potentially enhance mediation of ferromagnetic exchange [124].

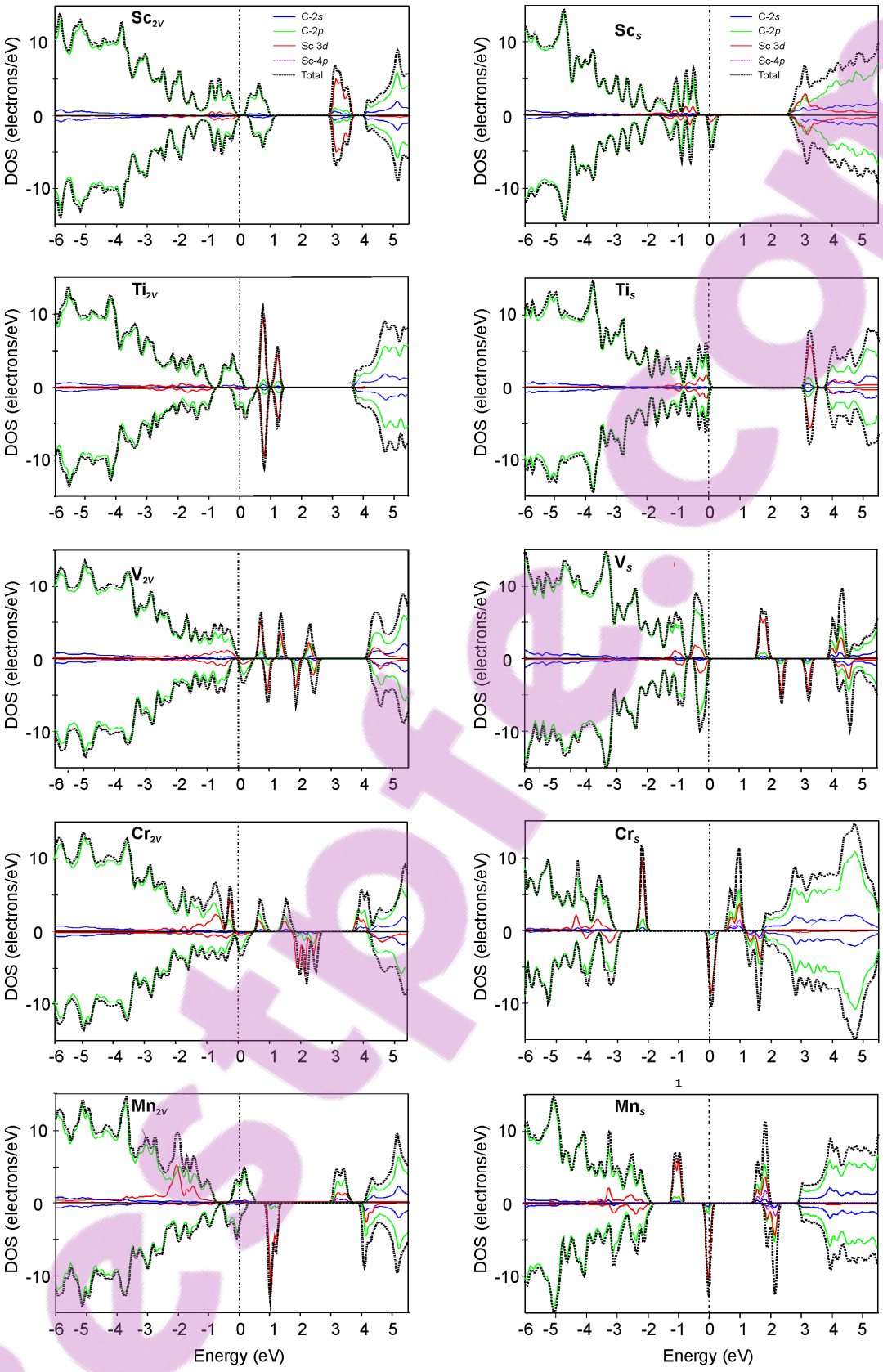

Figure 5.3 (a): Calculated total and partial spin polarised density of states (DOS) of 3*d* transition metals (Sc to Mn) in the neutral charge state in diamond at divacancy (2*V*) and substitutional (*S*) lattice sites. All energies are relative to the Fermi level indicated by the vertical dashed lines.

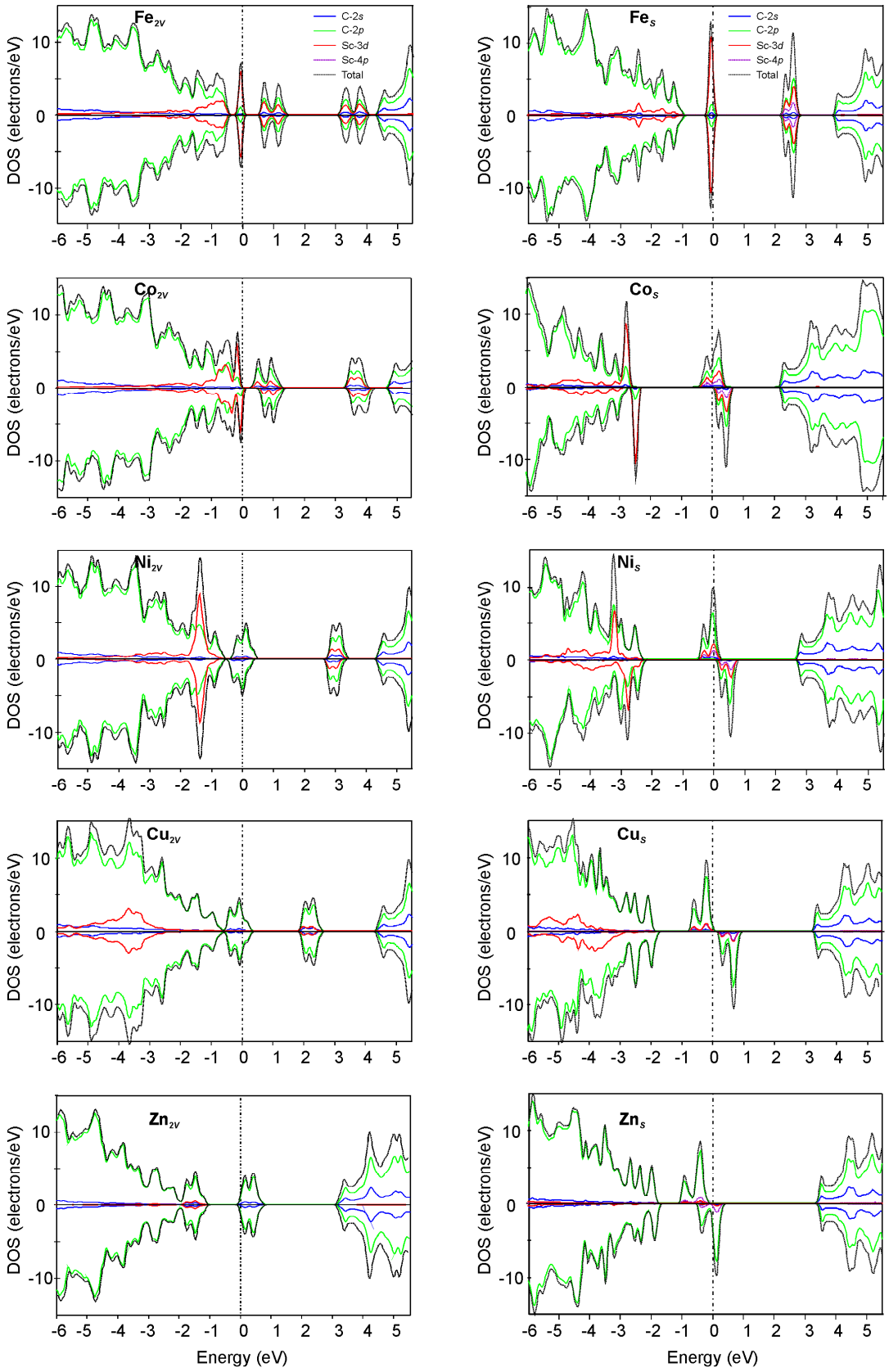

Figure 5.3 (b): Calculated total and partial spin polarised density of states (DOS) of 3*d* transition metals (Fe to Zn) in the neutral charge state in diamond at divacancy (2*V*) and substitutional (*S*) lattice sites. All energies are relative to the Fermi level indicated by the vertical dashed lines.

5.2.4.2 Band structure

The presence of spin polarised bands crossing the Fermi level implies that charge carriers travelling through these bands will be spin polarised in the ratio of spin-up to spin-down density of states at the Fermi level. However, the presence of spin polarised bands in itself is not a sufficient condition for efficient transport and injection of spin polarised charge carriers in device applications. An additional and necessary requirement is that charge carriers within the spin-polarised band should be sufficiently mobile [92]. To assess this requirement, we calculated the band structures of transition metal-doped diamond, as shown in Figure 5.4 where the bands are plotted for various high symmetry directions in the Brillouin zone at both the divacancy and substitutional lattice sites for the neutral charge state.

In Sc, Ti, Mn, Ni and Co at a divacancy site, a spin polarised impurity band is found to be present for both the spin-up and spin-down bands, and the Fermi level passes through this band in both spin directions. Therefore a Fermi surface exists for each of them, indicating that the systems are *metallic*, which may be a disadvantage for some spintronic applications since both spin components are present. However, for divacancy V and Cr, the Fermi level is close to the valence band, but passes neither through the spin-up nor spin-down bands, thus indicating that these systems may be *p*-type *semiconductors*, depending on thermal excitation.

On the other hand, the Fermi level passes through only one spin component of the impurity band for most of the substitutional transition metals (except for Ti, V and Fe). This indicates that these systems would be *half-metallic* – which is particularly significant for efficient spin injection of spin polarised current in spintronic device applications, since charge carriers travelling at the Fermi surface will undergo 100% spin polarisation by simple effective mass transport in the impurity band. In these cases, half-metallicity occurs since the exchange splitting is greater than the width of the occupied impurity band, so that all valence electrons are only in one spin direction [21].

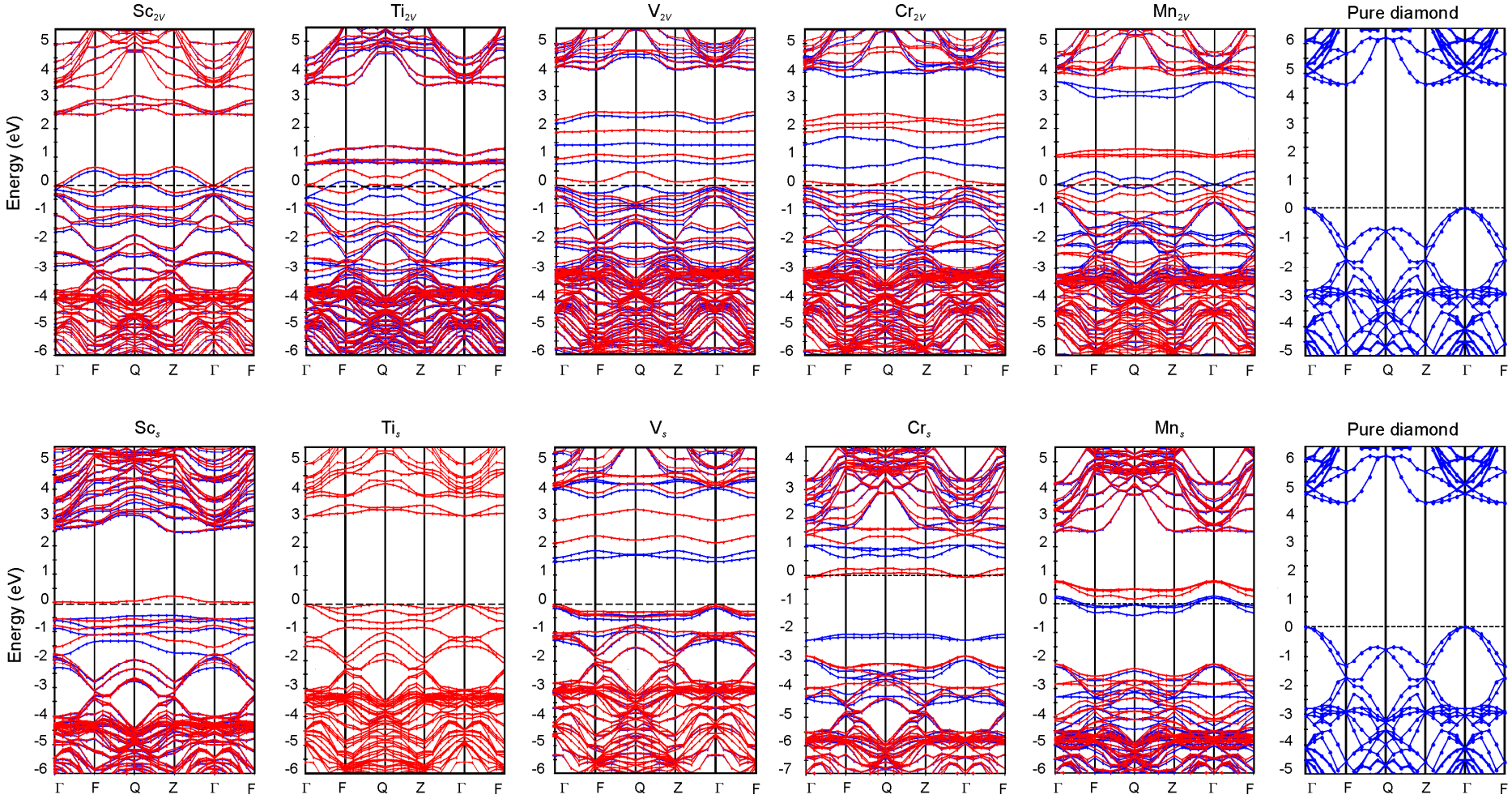

Figure 5.4: Spin-up (red curves) and spin-down (blue curves) band structures of neutral divacancy (TM_{2V}) and substitutional (TM_S) 3*d* transition metals (Sc to Mn) in a 64-atom diamond supercell. The band structure of a similar pure diamond supercell is also shown for comparison (Spin-up and spin-down band structures of pure diamond are identical). Dots correspond to data points; lines guide the eye. The energies are relative to the respective Fermi energies shown with horizontal dashed lines; levels below the Fermi level are filled, while those above are empty.

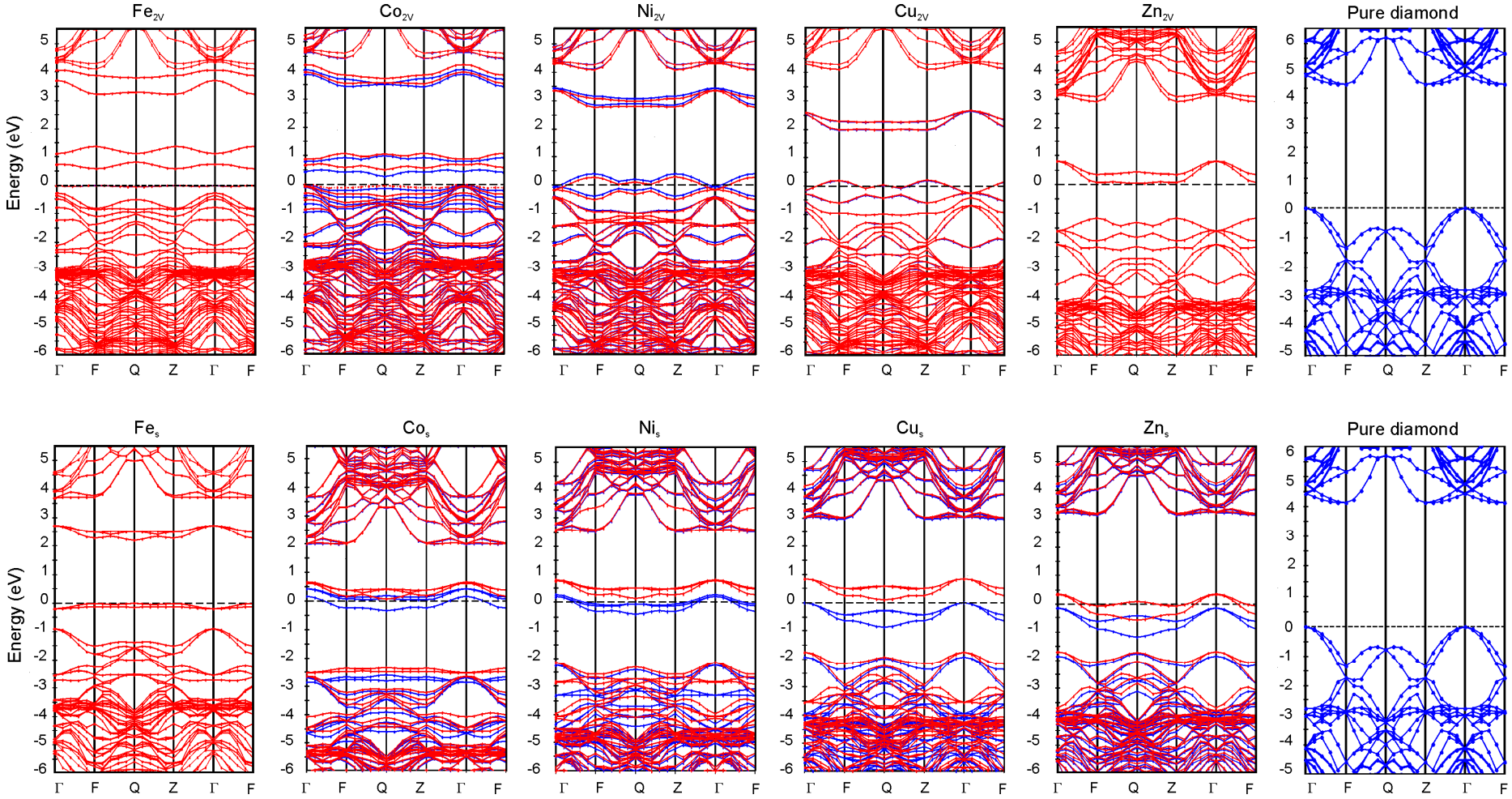

Figure 5.4 (continued): Spin-up (red curves) and spin-down (blue curves) band structures of neutral divacancy (TM_{2V}) and substitutional (TM_S) 3*d* transition metals (Fe to Zn) in a 64-atom diamond supercell. The band structure of a similar pure diamond supercell is also shown for comparison (Spin-up and spin down band structures of pure diamond are identical). Dots correspond to data points; lines guide the eye. The energies are relative to the respective Fermi energies shown with horizontal dashed lines; levels below the Fermi level are filled, while those above are empty.

5.2.5 Induced magnetic moments

Figure 5.5 presents trends of the calculated magnetic moments of transition metals in diamond across the 3*d* series for different charge states $(-2, -1, 0, -1, +2)$ at the divacancy, substitutional and interstitial lattice sites. We find that the magnitudes of the induced magnetic moments are generally dependent on the doping site and charge state. Importantly, the majority of 3*d* transition metals at any lattice site induce non-vanishing magnetic moments in the diamond supercell − an indication that incorporation of these impurities into diamond may lead to collective magnetic ordering upon impurity-impurity interactions [107], as will be discussed in Chapter six.

At the divacancy site, the variation of the induced magnetic moments across the 3*d* series in most charge states approximately tracks the trend of free atomic values (Sc: $1\mu_B$, Ti: $2\mu_B$, V: $3\mu_B$, Cr: $6\mu_B$, Fe: $5\mu_B$, Co: $4\mu_B$, and Ni: $2\mu_B$) [217], with Mn^{+2} inducing the highest magnetic moment of 3.2 μ_B. However, at the substitutional or interstitial sites, the free atomic trend is significantly changed due to the strong crystal field experienced by the transition metal atom at these sites.

In contrast to the substitutional site, a transition metal atom at a divacancy site behaves more like a free atom because of the relatively large atomic volume created by the two missing carbon atoms, thus causing little strain to the crystal lattice (hence small carbon nearest neighbour relaxation). This leads to weaker interaction with the carbon neighbours, thus resulting in weaker perturbation of the spin states. On the other hand, the strong interactions between the transition metal atom and its carbon neighbours at the substitutional and interstitial sites may significantly alter the atomic spin states, suggesting that the character of bulk magnetic properties in 3*d* transition metal-doped diamond will depend on the nature of interactions between the transition metal dopant with its carbon neighbours.

The origin of the calculated magnetic moments in transition metal-doped diamond can be explained as resulting from both the atomic interactions and orbital hybridization effects derived from spin splitting of the band gap orbitals in relation to the crystal field due to Stoner's model of magnetism [218]. For example, in the density of states (DOS) shown in Figure 5.3 for divacancy Fe, Ni, Cu, Zn as well as substitutional Fe in the neutral charge states, the DOS in both spin directions are identical in energy and therefore the spin splitting

energy is zero, thus yielding a zero magnetic moment in all of these cases (Table 5.2), in agreement with Stoner's criterion for ferromagnetism [218]. On the other hand, the weak spin splitting of the carbon 2*p* orbitals (~ 0.1 eV) compared to a large crystal splitting of ~3.0 eV in divacancy Sc^0 yields a low spin state of 0.4 μ_B. In contrast, the small *p-d* hybridization leads to a zero spin state in divacancy Ni^0, Cu^0 and Zn^0, while the contribution of the 4*p* orbitals to hybridization in the band gap for Cr^0, Ni^0, Cu^0 and Zn^0, together with a large spin splitting over the crystal field, leads to larger calculated magnetic moments of 2.0 μ_B, 2.0 μ_B, 3.0 μ_B and 2.0 μ_B, respectively.

Further, we find that the highest spin densities in transition metal-doped diamond reside on the transition metal atom, similar to previous studies on cobalt-doped diamond [164]. As a result, the total calculated magnetic moment is localized around the transition metal atom, with small contributions arising mainly from the carbon nearest neighbours, thus providing evidence of a strong localized character of the spin density distribution, as shown in Figure 5.6 for both high and lower symmetry distortions in Cr-doped diamond.

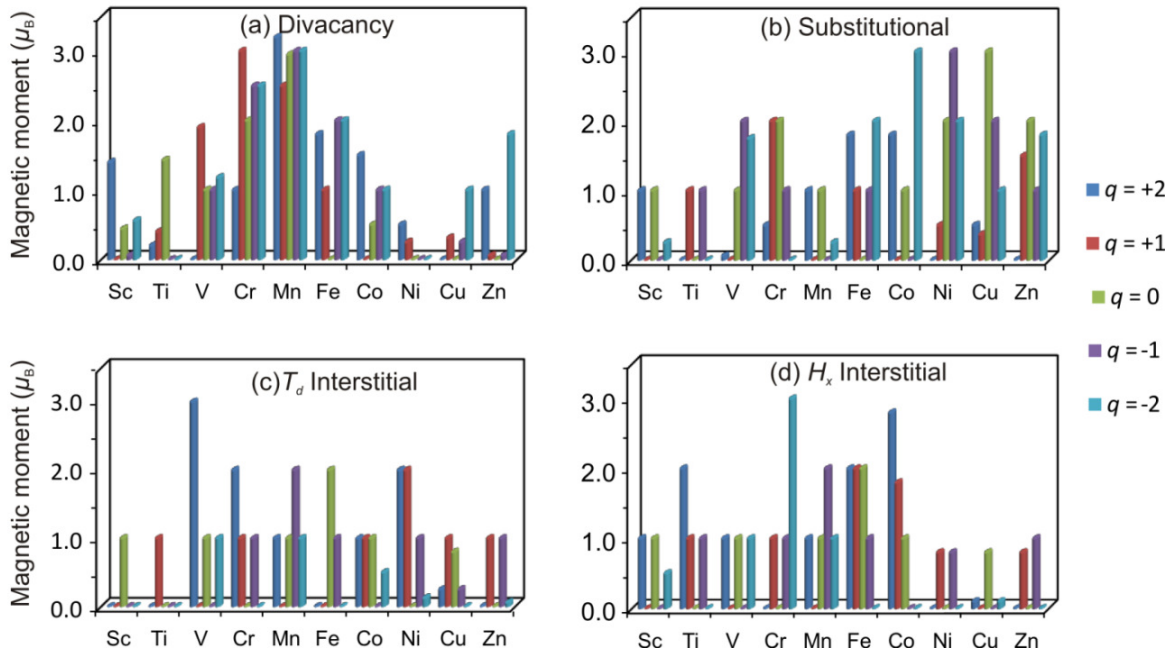

Figure 5.5: Calculated magnetic moments of 3*d* transition metals in different charge states (q = +2, =1, 0, -1, -2) at (a) divacancy (b) substitutional (c) tetrahedral (T_d) interstitial and (d) Hexagonal (H_x) interstitial lattice sites in diamond.

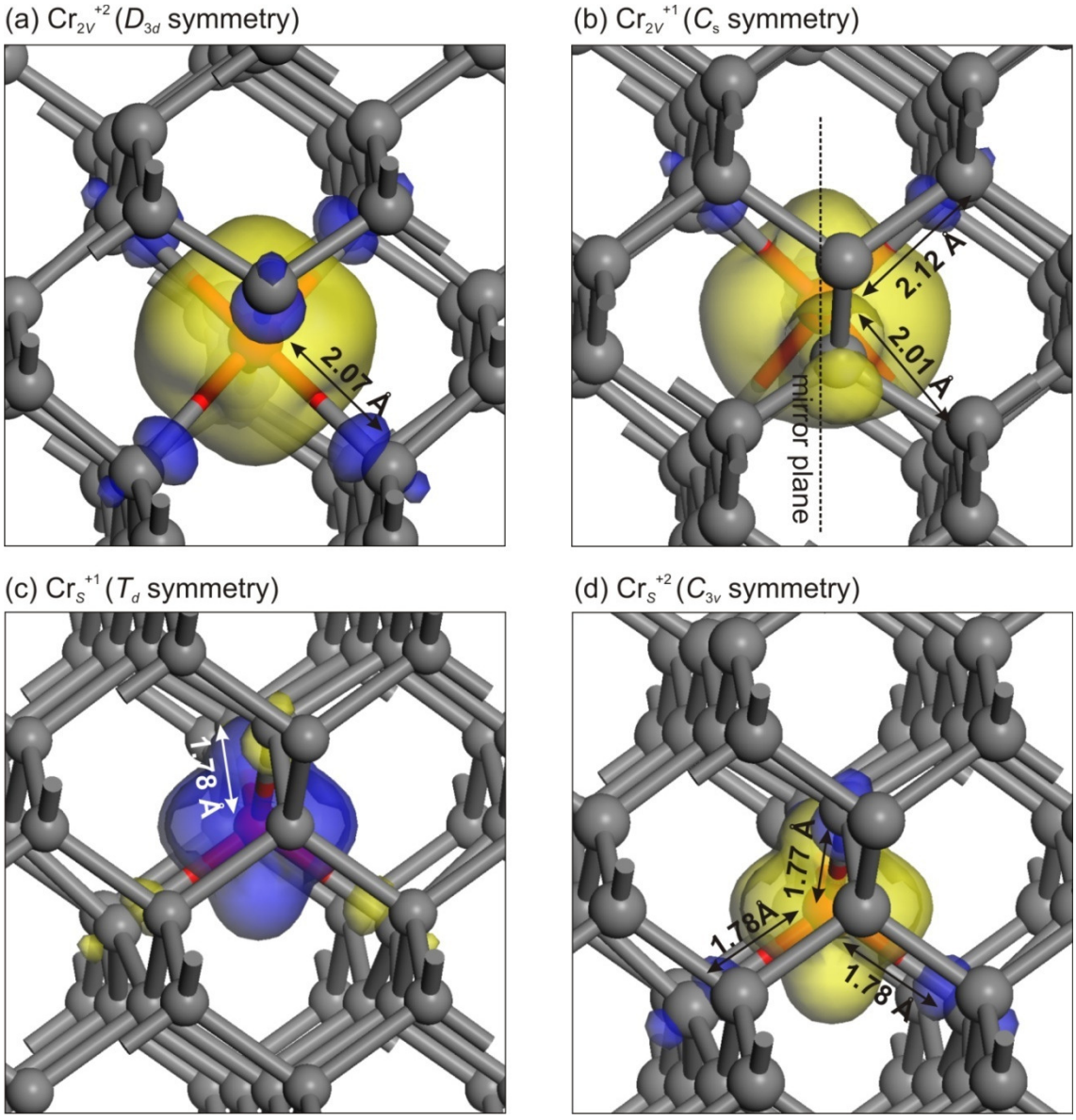

Figure 5.6: Illustration of geometries and isodensity surfaces of the spin density distributions of divacancy ($Cr^{+2}{}_{2V}$, $Cr^{+1}{}_{2V}$) and substitutional ($Cr^{+2}{}_{S}$, $Cr^{+1}{}_{S}$), with D_{3d}, C_s, C_{3v}, and T_d, symmetry, respectively. Blue surfaces correspond to spin up, yellow to spin down. Mirror plane in (b) is perpendicular to the plane of the page. The isosurface for both spin up and spin down densities correspond to a spin density of 0.05 electrons/Å^3. Illustrations are slightly rotated from a (110) plane

5.3 Comparison with previous models

The structural and electronic properties of transition metals in diamond in the neutral charge state, particularly those which are commonly used in High Pressure-High Temperature (HPHT) growth of synthetic diamond, have been modelled by a variety of computational models, many of which differ with each other on the relative energetic stability, symmetry

and magnetic moment. Here, we compare our results of the energetic stability, electronic structure and structural properties with those of previous computational models and discuss any discrepancies and their possible sources in order to establish a reliable and systematic understanding of the theoretical magnetic ordering properties of these defects in diamond.

Experimentally, most of the well established transition metal-related optical and EPR centres in diamond are based on nickel and cobalt. There is also unconfirmed evidence for Mn, Cu and Fe [186], while incorporation of Ti and Zn has only been achieved by ion implantation, but not during crystal growth [186,219]. In agreement with these results, previous theoretical findings [186,187] have shown that Ni has a lower formation energy in diamond compared to Co. However, no explanation exists as to why they these transition metals are preferentially incorporated into diamond containing other impurities (e.g. nitrogen) [152]. Our results show that the presence of donors, such as nitrogen and phosphorus may significantly lower the formation energy of 3*d* transition metals in diamond, thereby explaining why these transition metals are often detected in diamond grown with nitrogen [152].

The present results qualitatively agree with the findings of Watkins *et al.* [186] and Assali *et al.* [187] that transition metals in the middle of the 3*d* series are energetically more stable in diamond than those earlier or later in the series. In contrast, finite cluster results [148,149] predict that the energetic stability of transition metals in diamond increases with increasing 3*d* character, thus predicting transition metals later in the 3*d* series to be energetically more stable than those in the middle or earlier in the series. This discrepancy can possibly be attributed to the use of the finite atomic cluster model in which quantum confinement effects due to surface termination and defect-surface interaction play a significant role. However, finite cluster results may be relevant to nano-diamond applications.

Most of the earlier theoretical studies reported in literature for transition metal defects in diamond have been performed using the cluster or semi-empirical approaches [146,220]. Although many of these studies agree on the electronic models, there is no general agreement on the stability of the transition metals across the series 3*d* at various lattice sites. For example, the results of Alves *et al.* [220] using a molecular cluster model indicate that transition metals are more stable at tetrahedral interstitial lattice sites compared to the substitutional site, whereas the findings of Watkins *et al.* [146], also using the cluster model approach, contradict this result by predicting the substitutional site to be most favourable.

Our results using the pseudopotential GGA approximation on a 64-atom diamond supercell shows that most transition metals are energetically stable at a divacancy site, while the interstitial site is energetically highly metastable, which are in qualitative agreement with previous FP-LAPW results by Assali *et al.* [187,221] using a 54-atom supercell, except for V, Cr, and Mn which they predict to be more stable at a substitutional site compared to a divacancy site. To explain the origin of these discrepancies, we note that our calculations are in larger supercells (64-atoms compared to 54-atoms) and a higher $4 \times 4 \times 4$ optimized *k*-point sampling compared to a $2 \times 2 \times 2$ *k*-point sampling. To confirm this, we performed test calculations using a 32-atom supercell and fewer *k*-points ($1 \times 1 \times 1$, $2 \times 2 \times 2$ and $3 \times 3 \times 3$) and reproduced similar results as in references [187,221]. In particular, we found that results of the induced magnetic moment are significantly dependent on the quality of *k*-point sampling, therefore indicating that a good convergence with respect to the number of *k*-points must be attained if accurate results are to be achieved – however at a substantially increased computational cost. It is also noted that the gamma point was explicitly included in the Brillouin zone sampling as part of the Monkhorst-Pack mesh in references [187,221]. Since, in general, the full degeneracy of the gap states is only observed at the gamma point, such a sampling might be important in obtaining Jahn-Teller and other small distortions [151], although this is not needed if the *k*-mesh is well converged. In order to establish whether the explicit inclusion of the gamma point in the *k*-point sampling of the reciprocal space (by incorporation of a 'shift' of the *k*-mesh) has any effect on the calculated magnetic moments or the stable symmetries, we performed further calculations on selected cases using all electron LAPW methods as implemented in the state-of-the-art WIEN2k code, but we found it to have no effect on the results.

In conclusion, the above comparison of results for the various computational models which have so far been used to model transition metals and other defects in diamond show that discrepancies amongst them can be minimized by the following:

(i) In order to find the most stable geometry, it is necessary to also perform geometry optimizations with the transition metal atom initially displaced from the lattice site in a random direction at the beginning of the calculation. In addition, the initial spins must also be varied systematically in order to find the lowest energy corresponding to the most stable geometry. In cases where this is not done, a

calculation may only find a metastable structure. Some previous calculations may not have done this or the models used were not able to do this [222,223].

(ii) In order to ensure that the final spin density or magnetic state does not depend on the initial spin input during spin optimization, several initial spins must be considered. Some previous calculations may have used a single initial spin for geometry optimization which may not necessarily correspond to the lowest energy of the system as discussed in Section 5.2.

(iii) For accurate results to be obtained, a relatively large cluster or supercell size should be used, in addition to attaining good convergence with respect to the number of *k*-points, especially when calculating magnetic properties. However, it should be noted that the computational cost increases with the number of atoms or electrons (in a cluster or supercell) and number *k*-points used in sampling of the reciprocal space. Some earlier calculations may have been limited by the number of *k*-points, supercell or cluster size; hence results reported may not be as precise.

6. Magnetic ordering of 3*d* transition metals in diamond

6.1 Introduction

Magnetic ordering properties of various transition metals have been reported in many semiconductors, mainly in compound semiconductors (such as GaN, GaAs, and ZnO, among others [121,123]), but implementation in practical spintronic devices has largely been hindered by low Curie temperatures (T_C), as well as lack of other fundamental material properties [4]. Although some experimental observations of ferromagnetic response persisting up to room temperature have been reported in literature [224,225], many of the results have not been reproducible, and in most cases have been shown to be due to spurious effects [122] such as large magnetic clusters and inhomogeneous phases with high impurity concentrations [91]. Therefore, the search for other semiconductors which may exhibit room temperature ferromagnetic ordering continues unabated [199].

Previous theoretical studies in the search for ferromagnetically ordering transition metal dopants in diamond have predicted that ferromagnetic ordering of Mn in diamond is unlikely [73] (in the sense of the Zener model of ferromagnetism [111,124,199]), while neutral Co has been predicted [164] to order ferromagnetically with a relatively small magnetic moment of 0.4 μ_B per Co atom. However, in order to support significant spin polarisation current at high T_C, larger magnetic moments and ferromagnetic stabilization energies are required. Hence, there is a need to find alternative transition metal ions which may successfully be considered in the search for a diamond-based diluted magnetic semiconductor (DMS).

In Chapter five, results of the electronic structure, induced magnetic moments and hybridization of 3*d* transition metal defects with the host atom wave functions were discussed, based on the results of 64-atom diamond supercells containing one transition metal impurity at various lattice sites. However, by symmetry, a single transition metal impurity in a diamond supercell will correspond to ferromagnetic ordering if it induces a non-zero magnetic moment in the supercell, but, such magnetic ordering may not necessarily correspond to the ground state magnetic ordering of the defect-containing supercell.

Therefore, in this Chapter, we consider the nature of magnetic ordering arising from defect-defect interactions using a two-defect impurity model in larger supercells containing two transition metal impurities, allowing ferromagnetic, antiferromagnetic, ferrimagnetic and non-magnetic spin configurations. In particular, attention will be focussed in determining: (i) which 3*d* transition metal impurities induce significant non-vanishing magnetic moments when incorporated into diamond, and (ii) which charge states of these impurities, based on their magnetic stabilization energies and energetic stabilities relative to other possible charge states and lattice sites, may successfully be considered for fabricating a diamond-based DMS.

6.2 Theoretical approach

The magnetic ordering properties of substitutional and divacancy 3*d* transition metals (TM) impurities: Cr, Mn, Fe, Co and Ni, which have been demonstrated in the present study (Chapter four) to be energetically more favourable in diamond, were modelled using the computational details sumarized in Section 2.5.2. Magnetic interactions were calculated by doubling the respective fcc $2 \times 2 \times 2$ optimized 64-atom diamond supercells along the z direction, thus forming larger fcc $2 \times 2 \times 4$ 128-atom periodic diamond supercells containing two transition metal atoms ($C_{126}TM_2$ at the substitutional site; $C_{124}TM_2$ at the divacancy site) separated by twice diamond's optimized lattice constant ($2a_0 = 7.138$ Å).

The magnetic stabilization energies of the magnetic ground state, as well as other metastable magnetic states were determined by considering different configurations and magnitudes of parallel and antiparallel spin alignments of the two transition metal impurity atoms in various charge states $q = +2, +1, 0, -1, -2$ as described in Section 2.5.3. This approach has previously been used to successfully predict ferromagnetic ordering in other semiconductor materials and oxides [93,98-101]. However, it is noted that paramagnetic states and spin-glasses cannot be considered from the standard DFT approach; however ferromagnetism is likely to persist to higher temperatures in cases where other states (e.g. non-magnetic or antiferromagnetic) are relatively higher in energy.

Calculations of the induced magnetic moment, as well as the energy differences between different spin configurations, were done using the respective final geometries of the optimized 64-atom diamond supercells, without further geometry optimization of the 128-atom diamond supercells. Full geometry optimization of the 128-atom diamond supercells in

selected cases resulted in no changes to geometries and induced magnetic moments per impurity ion, and negligible changes in energy differences between different magnetic states (less than $0.01\,\mathrm{meV}$), similar to previous calculations in Mn-doped diamond [73]. It is important to note that small energy differences in the meV range are typical of magnetic materials, and are correctly described by Density Functional theory [92,93]. Stabilization energies between different magnetic states reported in this Thesis which differ by ~1 meV can be assumed to be negligible, in particular when compared to thermal effects which are likely to be much larger, particularly at room temperatures or higher.

To test the convergence of the total magnetic moments and the magnetic stabilization energies of different magnetic states with respect to the *k*-mesh density, different Monkhorst-Pack *k*-points sampling were used by considering various systematically sampled initial spin configurations. Convergence was achieved at $4 \times 2 \times 2$ *k*-points, below which the magnetic moments and magnetic stabilization energies were found to be significantly dependent on the number of *k*-points used for integration over the Brillioun zone; an increase in the number of *k*-points resulted in insignificant changes in the results. This underlines the importance of good *k*-point convergence with respect to the energy differences between different magnetic ordering states in order to reliably predict magnetic moments, ground state spin coupling and metastable magnetic moments. This is illustrated in Figure 6.1, showing the convergence of magnetic stabilization energy (ΔE) for different *k*-points in substitutional Cr^{-2}. For low *k*-point sampling ($\mathrm{i.e.}\, 1 \times 1 \times 1$ and $2 \times 2 \times 2$), we find that metastable states and the energy difference between different metastable magnetic states cannot be reliably predicted.

In order to evaluate the effect of TM-TM separations on structural and magnetic stabilization energies, we carried out representative calculations with a reduced separation of one lattice constant ($a_0 = 3.569$ Å), in addition to the two lattice constant separation discussed in this Chapter. Further, to ensure that results of the calculated spin polarisations or energy differences between different magnetic states were not dependent on relative defect symmetry orientation between the two transition metal impurities, different sets of relative geometric orientations between two transition metal centres were considered in selected cases, but this was found to have no effect on the results.

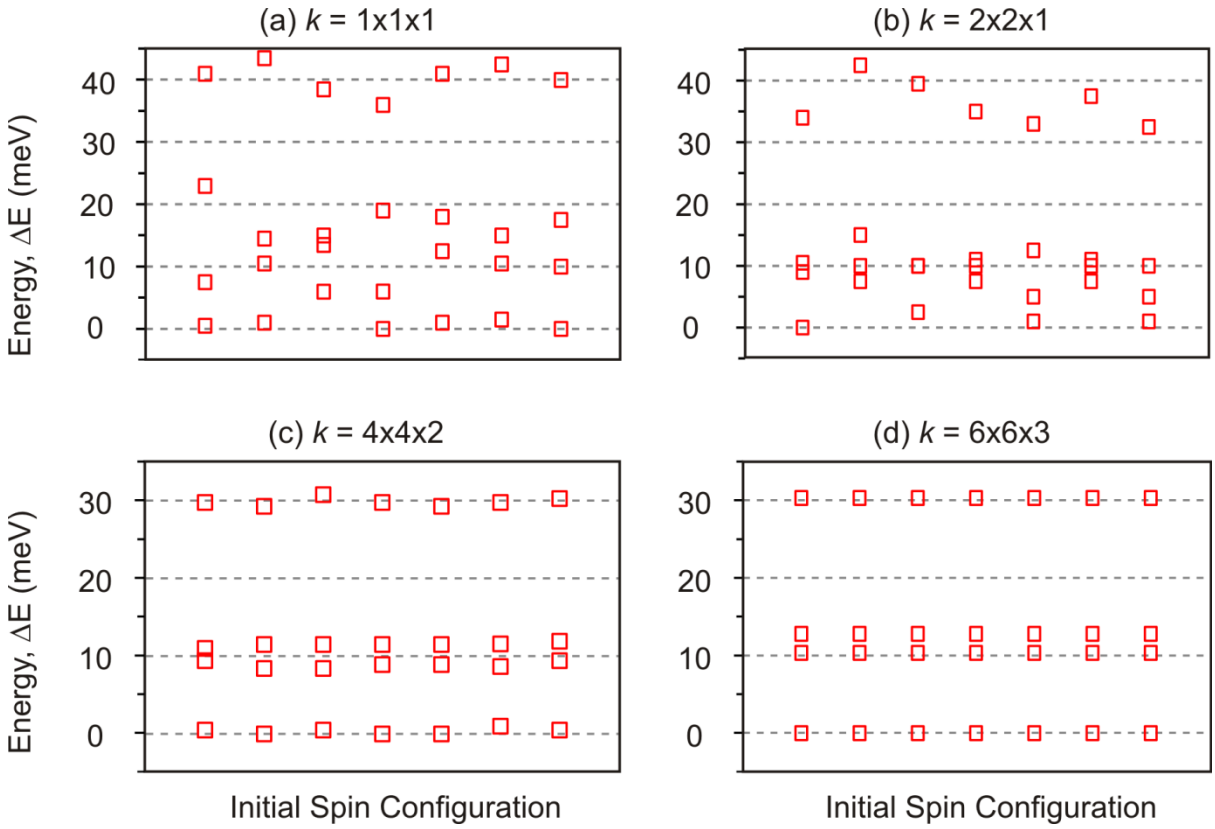

Figure 6.1: Convergence of magnetic stabilization energy (ΔE) with the *k*-point sampling density for different initial configurations in substitutional Cr^{-2} doped diamond showing four distinct magnetic ordering states. The spin configuration (x-axis) represents different initial magnitudes of parallel/antiparallel spin alignments of the two Cr atoms in the supercell. Data points represent the final total energy of the supercell with specific final magnetic moment and spin configuration. The energies are relative to the lowest total energy of each initial spin configuration.

6.3 Spin population and spin density distribution

Tables 6.1 (i) to (v) present a summary of the Mulliken spin populations for the 3*d* transition metal ions and their nearest carbon neighbour (C_{NN}) atoms for the magnetic ground state and other metastable magnetic states. In each case, the corresponding magnetic stabilization energies relative to the ground state and the induced magnetic moments per transition metal ion are also given. We find the spin contribution of the carbon atoms further out from the TM centres (not shown) to be insignificant, thus providing evidence of the strong localized character of the spin density distribution. As a result, the total magnetic moment is localized around the transition metal impurities and its immediate carbon atom neighbours, suggesting that magnetic interactions in 3*d* transition metal-doped is dominated by nearest neighbour interactions, similar to other diluted magnetic semiconductors [94-97]. We find the individual spin contributions of the nearest carbon neighbours to be strongly dependent on the symmetry

around the transition metal impurity, with the highest spin densities amongst the carbon neighbours residing on those carbon atoms forming shorter TM-C bonds, due to stronger atomic interactions.

These results can be explained by the manner in which the unpaired electrons of the transition metal ions introduce a spin density on the neighbouring carbon atoms. From the partial density of states illustrated in Figure 5.3 (showing the contribution of each atomic orbital to the total density of states), incorporation of transition metals into diamond introduces spin polarised impurity bands into the diamond band gap, due to hybridization between 2*s*, 2*p* carbon orbitals and the transition metal 3*d* orbitals, as well as the 4*p* orbitals for transition metals occupying substitutional sites). Therefore the distribution of spin density in transition metal-doped diamond can be thought as resulting from a *spin delocalization* or *spin polarisation mechanism* [226], whereby the transition metal ion either transfers or induces a spin moment to those carbon atoms directly bonded to it.

The spin delocalization mechanism requires that a spin of the same direction (i.e. either spin-up or spin-down) must be transferred to those carbon atoms directly bonded to the transition metal atom [226]. This is illustrated in Figure 6.2 (a) by the isodensity surfaces of the spin density distribution in substitutional Fe^{-2}. We find this requirement of spin transfer to hold only for divacancy Cr^{-1} and substitutional Fe^{-2}, but the majority of transition metal ions considered here [Tables 6.1 (a) to (e)] are found transfer a spin of the opposite direction to their neighbouring carbon atoms, as illustrated in Figure 6.2 (b), indicating that spins of the bonding electron pairs are polarised.

As opposed to the spin delocalization mechanism, the spin polarisation mechanism results from Pauli's exclusion principle which prohibits two electrons from occupying exactly the same state (including spin − *n, l, m* quantum numbers). Therefore electrons occupying exactly the same orbital must have opposite spins, which in practice makes it unfavourable for electrons of equal orbital and spin to be in the same region of space. As a consequence, the spins of bonding electrons are polarised in such a way that the spin direction around the transition metal ions is different from that of the carbon atoms bonded to it, which is the case for most of the transition metal ions considered in the present study.

(a) Fe^{-2}_{S}: Spin delocalization

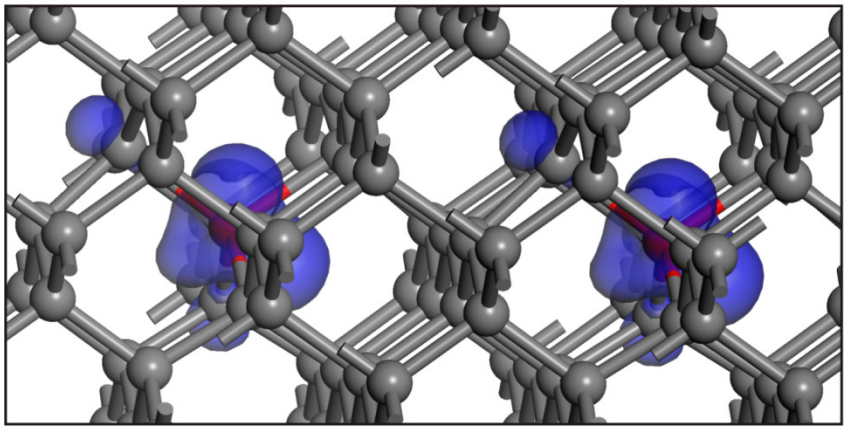

(b) Fe^{+2}_{S}: Spin polarisation

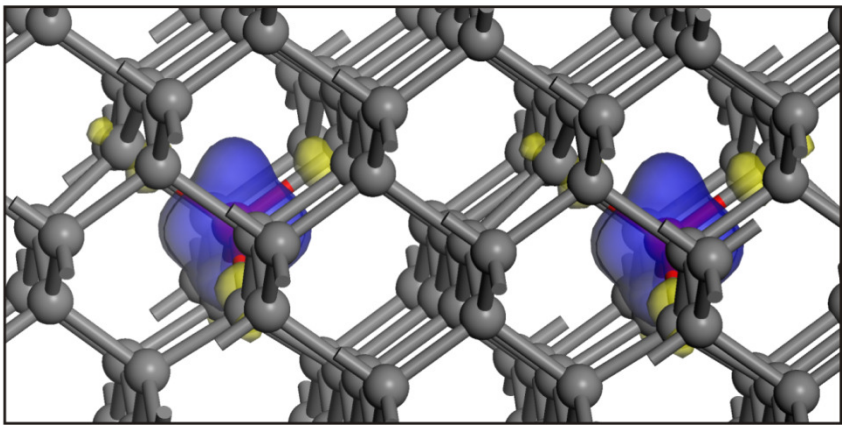

Figure 6.2: Illustration of isodensity surfaces of the spin density distribution in optimized (a) substitutional Fe^{-2}_{S} showing *spin delocalization* and (b) substitutional Fe^{+2}_{s} showing *spin polarisation* upon magnetic interaction. The carbon neighbours in each case acquire a spin of the same or opposite direction as that of iron, respectively. Blue surfaces correspond to spin-up, yellow to spin- down. The highest spin density resides on the Fe atoms (red balls). The isosurface for both spin up and spin down densities correspond to a spin density of 0.05 electrons/$Å^3$. Illustrations are slightly rotated from a (110) plane.

Chromium

(a) Divacancy Cr

Charge state	Magnetic ground state $+\Delta E$ metastable states	Spin population (μ_B) TM_1 (C_{NN})	Spin population (μ_B) TM_2 (C_{NN})	Total magnetic moment (μ_B)
Cr^{+2}	FM, 2.5 μ_B	+2.64 (-0.36)	+2.64 (-0.36)	5.0 [6.0]
	+16.9 meV, AF, 2.5 μ_B	+2.58 (-0.36)	-2.58 (0.36)	0.0 [5.7]
Cr^{+1}	AF, 3.0 μ_B	+2.66 (-0.08)	-2.66 (0.08)	0.0 [6.3]
	+6.6 meV, FM, 3.0 μ_B	+2.70 (-0.04)	+2.70 (-0.04)	6.0 [6.6]
Cr^{0}	FM, 2.0 μ_B	+2.06 (-0.24)	+2.06 (-0.24)	4.0 [5.2]
	+0.6 meV, AF, 2.0 μ_B	+2.02 (-0.24)	-2.02 (+0.24)	0.0 [5.1]
	+170.5 meV, FI, 1.0 μ_B	+2.02 (-0.22)	0.00 (0.00)	2.0 [3.6]
	+327.3 meV, NM, 0.0 μ_B	0.00 (0.00)	0.00 (0.00)	0.0 [1.9]
Cr^{-1}	AF, 4.0 μ_B	+3.06 (+0.92)	-3.04 (-0.92)	0.0 [8.6]
	+14.7 meV, FM, 2.6 μ_B	+3.08 (+0.32)	+3.06 (-1.48)	5.3 [7.9]
Cr^{-2}	AF, 3.3 μ_B	+3.08 (-0.08)	-3.06 (+0.08)	0.0 [6.6]
	+10.5 meV, FI, 0.5 μ_B	+3.10 (+0.16)	-3.06 (+0.60)	1.0 [7.0]
	+11.3 meV, FM, 2.3 μ_B	+3.06 (-0.84)	+3.08 (-0.84)	4.6 [7.3]
	+30.5 meV, FM, 3.3 μ_B	+3.10 (0.00)	+3.08 (0.00)	6.7 [6.8]

(b) Substitutional Cr

Cr^{+2}	FM, 0.5 μ_B	+0.78 (-0.16)	+0.78 (-0.16)	1.0 [2.0]
	+23.6 meV, AF, 0.5 μ_B	+0.80 (-0.16)	-0.78 (0.16)	0.0 [1.9]
Cr^{+1}	FI, 1.0 μ_B	+1.20 (-0.24)	+1.28 (-0.24)	2.0 [3.0]
	+40.5 meV, AF, 1.0 μ_B	+1.24 (-0.36)	-1.24 (0.36)	0.0 [2.8]
Cr^{0}	AF, 2.0 μ_B	+2.16 (-0.40)	-2.16 (+0.40)	0.0 [5.0]
	+1.1 meV, FM, 2.0 μ_B	+2.16 (-0.40)	+2.16 (-0.40)	4.0 [5.1]
Cr^{-1}	FM, 1.0 μ_B	+1.12 (-0.16)	+1.10 (-0.16)	2.0 [2.7]
	+49.2 meV, AF, 1.0 μ_B	+1.12 (-0.16)	-1.10 (0.16)	0.0 [2.6]
	+63.1 meV, FI, 0.1 μ_B	+1.18 (-0.24)	-0.96 (0.16)	0.2 [2.4]
Cr^{-2}	NM, 0.0 μ_B	0.00 (0.00)	0.00 (0.00)	0.0 [0.0]

Table 6.1(i): Spin populations and induced magnetic moments of the magnetic ground state and metastable magnetic states (FM: Ferromagnetic, AF: Antiferromagnetic, FI: Ferrimagnetic, NM: Non-magnetic) in Cr-doped diamond for (a) divacancy and (b) substitutional sites in the charge states +2, +1, 0, -1, -2. For metastable states, $+\Delta E$ is the corresponding stabilization energy relative to the most stable magnetic ordering state for that charge state. TM_n is the spin population on each of the two Cr atoms in the 128-atom diamond supercell, while C_{NN} is the total contribution of the respective carbon nearest neighbour atoms. MM Total denotes the total integrated magnetic moment of the whole (128-atom) supercell (including both Cr atoms), while the square brackets indicate the respective total integrated absolute magnetic moment $|\mu_B|$ in the 128-atom diamond supercell.

Manganese

(a) Divacancy Mn

Charge state	Magnetic ground state $+\Delta E$ metastable states	Spin population (μ_B) TM_1 (C_{NN})	 TM_2 (C_{NN})	Total magnetic moment (μ_B)
Mn^{+2}	FM, 3.0 μ_B	+3.34 (-0.48)	+3.34 (-0.48)	6.0 [7.5]
	+2.9 meV, AF, 3.0 μ_B	+3.32 (-0.48)	-3.32 (+0.48)	0.0 [7.3]
	+1138.9 meV, FI, 2.0 μ_B	+3.32 (-0.48)	+1.20 (-0.24)	4.0 [5.7]
	+1141.2 meV, FI, 1.0 μ_B	+3.32 (-0.48)	-1.20 (+0.24)	2.0 [5.6]
Mn^{+1}	FM, 2.5 μ_B	+3.32 (-0.84)	+3.32 (-0.84)	5.1 [7.9]
	+4.2 meV, AF, 0.2 μ_B	+3.32 (-0.40)	-3.32 (+0.88)	0.5 [7.6]
Mn^{0}	AF, 5.0 μ_B	+3.32 (-1.80)	-3.32 (+1.80)	0.0 [10.0]
	+40.3 meV, FI, 2.6 μ_B	-3.30 (-0.08)	-3.32 (+1.60)	5.2 [8.4]
Mn^{-1}	AF, 2.5 μ_B	+3.32 (-0.80)	-3.32 (0.88)	0.1 [7.9]
	+2.3 meV, FM, 2.5 μ_B	+3.30 (-0.84)	+3.30 (-0.84)	5.0 [7.9]
	+4.5 meV, FI, 0.3 μ_B	+3.32 (-0.40)	-3.30 (+1.20)	0.6 [7.7]
	+4.9 meV, FM, 2.6 μ_B	+3.30 (-0.72)	+3.30 (-0.72)	5.3 [7.6]
	+6.9 meV, FI, 0.5 μ_B	+3.30 (-1.14)	-3.32 (+0.32)	0.9 [7.8]
Mn^{-2}	AF, 3.0 μ_B	+3.32 (-0.48)	-3.32 (0.48)	0.0 [7.3]
	+2.4 meV, FM, 3.0 μ_B	+3.32 (-0.48)	+3.32 (-0.48)	6.0 [7.3]

(b) Substitutional Mn

Mn^{+2}	AF, 1.0 μ_B	+1.40 (-0.22)	-1.40 (0.22)	0.0 [3.8]
	+7.6 meV, FM, 1.0 μ_B	+1.34 (-0.28)	+1.34 (-0.32)	2.0 [3.5]
	+14.6 meV, FM, 1.2 μ_B	+1.48 (-0.36)	+1.48 (-0.36)	2.3 [3.9]
Mn^{+1}	AF, 2.0 μ_B	+2.28 (-0.48)	-2.28 (+0.48)	0.0 [5.4]
	+1.1 meV, FM, 2.0 μ_B	+2.28 (-0.48)	+2.28 (-0.48)	4.0 [5.4]
	+590.4 meV, FI, 1.0 μ_B	+2.28 (-0.48)	0.00 (0.00)	2.0 [4.0]
	+1 179.3 meV, AF, 0.5 μ_B	0.00 (0.00)	0.00 (0.00)	0.0 [2.3]
Mn^{0}	FM, 1.0 μ_B	+1.20 (-0.10)	+1.20 (-0.10)	2.0 [2.7]
Mn^{-1}	NM, 0.0 μ_B	0.00 (0.00)	0.00 (0.00)	0.0 [0.0]
Mn^{-2}	FM, 0.3 μ_B	+0.20 (0.00)	+0.18 (0.00)	0.5 [0.6]

Table 6.1 (ii): Spin populations and the induced magnetic moment of the magnetic ground state and metastable magnetic states in Mn-doped diamond for (a) divacancy and (b) substitutional sites in the charge states +2, +1, 0, -1, -2, similar to Table 6.1 (i) for chromium.

Iron

(a) Divacancy Fe

Charge state	Magnetic ground state $+\Delta E$ metastable states	Spin population (μ_B) TM_1 (C_{NN})	Spin population (μ_B) TM_2 (C_{NN})	Total magnetic moment (μ_B)
Fe^{+2}	FM, 2.0 μ_B	+2.52 (-0.60)	+2.48 (-0.64)	4.0 [6.0]
	+33.7 meV, AF, 2.0 μ_B	+2.50 (-0.28)	-2.48 (+0.28)	0.0 [5.4]
Fe^{+1}	AF, 2.5 μ_B	+1.76 (-0.88)	-1.76 (+0.86)	0.0 [4.9]
Fe^{0}	NM, 0.0 μ_B	0.00 (0.00)	0.00 (0.00)	0.0 [0.0]
Fe^{-1}	FI, 0.2 μ_B	+2.24 (-0.72)	-2.26 (+0.52)	0.3 [5.6]
	+2.5 meV, FI, 0.3 μ_B	+2.28 (-0.40)	-2.22 (+0.84)	0.6 [5.6]
	+3.9 meV, FI, 1.8 μ_B	+2.24 (-0.56)	+2.26 (-0.48)	3.6 [5.3]
	+12.9 meV, FI, 2.3 μ_B	+2.28 (-0.24)	+2.26 (0.00)	4.6 [5.0]
Fe^{-2}	AF, 2.0 μ_B	+2.18 (-0.36)	-2.18 (+0.36)	0.0 [4.9]
	+1.7 meV, FM, 2.0 μ_B	+2.20 (-0.24)	+2.20 (-0.24)	4.0 [4.9]

(b) Substitutional Fe

Fe^{+2}	FI, 1.8 μ_B	+1.66 (-0.32)	+1.70 (-0.32)	3.6 [4.4]
	+7.5 meV, AF, 1.8 μ_B	+1.66 (-0.32)	-1.64 (+0.32)	0.0 [4.0]
Fe^{+1}	FI, 1.0 μ_B	+1.04 (-0.24)	+1.12 (-0.24)	2.0 [2.6]
	+33.3 meV, AF, 1.0 μ_B	+1.04 (-0.24)	-1.12 (+0.24)	0.0 [2.6]
Fe^{0}	NM, 0.0 μ_B	0.00 (0.00)	0.00 (0.00)	0.0 [0.0]
Fe^{-1}	AF, 1.0 μ_B	+0.64 (+0.12)	-0.64 (-0.12)	0.0 [2.1]
	+9.8 meV, FM, 1.0 μ_B	+0.70 (+0.12)	+0.70 (+0.12)	2.0 [2.2]
Fe^{-2}	AF, 2.0 μ_B	+1.30 (+0.22)	-1.32 (-0.22)	0.0 [3.7]
	+1.0 meV, FM, 2.0 μ_B	+1.40 (+0.26)	+1.40 (+0.26)	4.0 [4.1]
	+116.4 meV, FI, 1.0 μ_B	+1.40 (+0.22)	0.00 (0.00)	2.0 [3.1]

Table 6.1 (iii): Spin populations and the induced magnetic moment of the magnetic ground state and metastable magnetic states in Fe-doped diamond for (a) divacancy and (b) substitutional sites in the charge states +2, +1, 0, -1, -2, similar to Table 6.1 (i) for chromium.

Cobalt

(a) Divacancy Co

Charge state	Magnetic ground state $+\Delta E$ metastable states	Spin population (μ_B) TM_1 (C_{NN})	 TM_2 (C_{NN})	Total magnetic moment (μ_B)
Co^{+2}	FM, 1.0 μ_B	+0.96 (-0.12)	+0.96 (-0.12)	2.0 [2.5]
	+18.6 meV, AF, 1.0 μ_B	+0.94 (-0.12)	-0.92 (+0.12)	0.0 [2.2]
Co^{+1}	NM, 0.0 μ_B	0.00 (0.00)	0.00 (0.00)	0.0 [0.0]
Co^{0}	FM, 0.5μ_B	+0.16 (+0.34)	+0.16 (+0.34)	1.1 [1.2]
	+13.8 meV, AF, 0.5 μ_B	+0.20 (+0.54)	-0.20 (-0.54)	0.0 [1.8]
	+36.4 meV, NM, 0.0 μ_B	0.00 (0.00)	0.00 (0.00)	0.0 [0.0]
Co^{-1}	AF, 1.5 μ_B	+0.62 (+0.86)	-0.62 (-0.86)	0.0 [3.6]
	+34.8 meV, FM, 1.5 μ_B	+0.58 (+0.68)	+0.58 (+0.68)	2.9 [3.0]
	+55.6 meV, FI, 0.8 μ_B	+0.60 (0.80)	+0.12 (-0.12)	1.6 [2.4]
Co^{-2}	AF, 1.0 μ_B	+0.46 (+0.28)	-0.46 (-0.28)	0.0 [1.7]
	+15.2 meV, FM, 1.0 μ_B	+0.50 (+0.40)	+0.50 (+0.40)	2.0 [2.1]

(b) Substitutional Co

Co^{+2}	FM, 0.2 μ_B	+0.02 (0.00)	+0.02 (0.00)	0.3 [0.3]
	+0.4 meV, NM, 0.0	0.00 (0.00)	0.00 (0.00)	0.0 [0.1]
Co^{+1}	NM, 0.0 μ_B	0.00 (0.00)	0.00 (0.00)	0.0 [0.0]
Co^{0}	FM, 1.0 μ_B	+0.58 (+0.30)	+0.58 (+0.30)	2.0 [2.1]
	+14.2 meV, AF, 1.0 μ_B	+0.58 (+0.30)	-0.58 (-0.30)	0.0 [2.0]
	+48.2 meV, FI, 0.5 μ_B	0.00 (+0.04)	-0.54 (-0.30)	1.0 [1.2]
	+80.2 meV, NM, 0.0μ_B	0.00 (0.00)	0.00 (0.00)	0.0 [0.0]
Co^{-1}	FM, 2.0 μ_B	+1.24 (+0.52)	+1.24 (+0.52)	4.0 [4.1]
	+13.9 meV, AF, 2.0 μ_B	+1.16 (+0.48)	-1.16 (-0.48)	0.0 [3.8]
	+132.0 meV, FI, 1.0 μ_B	+0.02 (-0.02)	+1.26 (+0.52)	2.0 [3.2]
Co^{-2}	AF, 3.0 μ_B	+1.88 (+0.64)	-1.88 (-0.64)	0.0 [5.9]
	+46.4 meV, FM, 3.0 μ_B	+1.92 (+0.64)	+1.92 (+0.64)	6.0 [6.1]
	+362.3 meV, FI, 2.0 μ_B	+1.90 (+0.64)	+0.68 (+0.24)	4.0 [5.1]
	+444.2 meV, FI, 1.5 μ_B	+1.88 (+0.64)	+0.04 (+0.02)	3.0 [4.4]

Table 6.1 (iv): Spin populations and the induced magnetic moment of the magnetic ground state and metastable magnetic states in Co-doped diamond for (a) divacancy and (b) substitutional sites in the charge states +2, +1, 0, -1, -2, similar to Table 6.1 (i) for chromium.

Nickel

(a) Divacancy Ni

Charge state	Magnetic ground state $+\Delta E$ metastable states	Spin population (μ_B) TM_1 (C_{NN})	Spin population (μ_B) TM_2 (C_{NN})	Total magnetic moment (μ_B)
Ni^{+2}	NM, 0.0 μ_B	0.00 (0.00)	0.00 (0.00)	0.0 [0.0]
Ni^{+1}	FM, 0.3 μ_B	0.00 (+0.16)	0.00 (+0.16)	0.5 [0.6]
	+1.6 meV, AF, 0.1 μ_B	0.00 (-0.04)	0.00 (-0.04)	0.0 [2.5]
Ni^{0}	AF, 1.5 μ_B	0.00 (+1.04)	0.00 (-1.12)	0.1 [3.0]
	+29.8 meV, FI, 0.4 μ_B	0.00 (-0.36)	+0.06 (-0.36)	0.8 [1.0]
	+31.0 meV, FI, 0.8 μ_B	0.00 (-0.72)	+ 0.12 (-0.72)	1.6 [1.9]
Ni^{-1}	NM, 0.0 μ_B	0.00 (0.00)	0.00 (0.00)	0.0 [0.2]
	+0.3 meV, FM, 0.5 μ_B	0.00 (+0.36)	0.00 (+0.36)	1.0 [1.0]
Ni^{-2}	NM, 0.0 μ_B	0.00 (0.00)	0.00 (0.00)	0.0 [0.0]

(b) Substitutional Ni

Ni^{+2}	NM, 0.0 μ_B	0.00 (0.00)	0.00 (0.00)	0.0 [0.0]
Ni^{+1}	FM, 0.5 μ_B	+0.22 (+0.26)	+0.20 (+0.24)	1.0 [1.1]
	+17.1 meV, FI, 0.5 μ_B	+0.08 (+0.12)	-0.04 (-0.02)	0.1 [0.6]
Ni^{0}	AF, 1.7 μ_B	-0.74 (+0.80)	+0.74 (+0.82)	0.0 [3.5]
	+36.8 meV, FM, 2.0 μ_B	+0.86 (+0.94)	+0.86 (+0.94)	4.0 [4.1]
Ni^{-1}	AF, 3.0 μ_B	+1.34 (+1.20)	-1.34 (-1.20)	0.0 [5.8]
	+81.5 meV, FM , 3.0 μ_B	+1.40 (+1.28)	+1.40 (+1.28)	6.0 [6.2]
	+257.0 meV, FI, 1.0 μ_B	+1.36 (+1.20)	-0.42 (-0.42)	2.0 [5.1]
	+281.1 meV, FI, 2.0 μ_B	+1.36 (+1.22)	+0.50 (+0.46)	4.0 [5.2]
Ni^{-2}	FM, 2.0 μ_B	+1.04 (+0.70)	+1.04 (+0.70)	4.0 [4.2]
	+63.0 meV, AF, 2.0 μ_B	+1.00 (+0.66)	-1.00 (-0.66)	0.0 [3.9]

Table 6.1 (v): Spin populations and the induced magnetic moment of the magnetic ground state and metastable magnetic states in Mn-doped diamond for (a) divacancy and (b) substitutional sites in the charge states +2, +1, 0, -1, -2, similar to Table 6.1 (i) for chromium.

6.4 Magnetic states and magnetic stabilization

Figures 6.3 (i) to (v) illustrate spin optimized magnetic ground states and metastable states of 3*d* transition metal-doped diamond and the respective magnetic moments per impurity atom for various charge states $(+2, +1, 0, -1, -2)$ at the substitutional and divacancy lattice sites, calculated with an effective TM-TM impurity separation of two lattice constants (7.138 Å). The corresponding details of the total magnetic moment for the whole supercell and spin populations on the transition metal atom, as well as on the neighbouring carbon atoms are summarized in Tables 6.1 (i) to (v) above. We find the magnetic stabilization energies for most of the transition metals at the substitutional site for the various charge states to be relatively larger compared to the divacancy site, a result that may be ascribed to the additional contribution of the 4*p* orbitals to hybridization over and above the 3*d* orbitals for transition metals at the substitutional site (Figure 5.3). This result is consistent with the stronger interaction between the transition metal atom and its carbon neighbours at the substitutional site compared to the divacancy site, thus confirming that interactions between spins of the individual defect centres in transition metal-doped diamond are sensitive to the host environment.

We find that the majority of 3*d* transition metal impurities in the various charge states possess two or more magnetic states with different spin coupling configurations, thus presenting a possibility of achieving magnetic metastability in transition metal-doped diamond. The possibility of transitions between different magnetic spin states represents a Spin-Cross-Over (SCO) phenomenon which is of technological importance in memory and data storage devices [227]. Potential manipulation of the SCO phenomenon by external perturbations (light irradiation [228-231], or electric field [232,233]) in transition metal-doped diamond could correspond to a magnetic phase change, and therefore will be related to the stabilization energy barrier between the different magnetic states (Figure 6.3).

It is emphasized that the magnetic states illustrated in Figures 6.3 (i) to (v) were obtained by considering spin interactions between two transition metal impurities in diamond by performing spin optimization using a wide range of systematically sampled initial spins, allowing ferromagnetic, antiferromagnetic, ferrimagnetic and non-magnetic interactions as described in Section 6.2. This was necessary to ensure that true magnetic ground states, as well as all possible metastable states were found.

To confirm the stability limits of these magnetic states, we carried out Fixed Spin Moment (FSM) self consistent calculations [34] in selected cases to obtain the energy hypersurface as a function of magnetic moment. The spin optimized magnetic moments were found to correspond to FSM energy minimums, thus confirming the stability of the spin optimized magnetic states reported here. However, it is noted that the FSM method does not allow flexibility in determining the magnetic nature of spin interactions (i.e. whether ferromagnetic, antiferromagnetic, ferrimagnetic or non-magnetic) other than giving the magnetic moment corresponding to a particular minimum of the energy hypersurface [34]. Therefore when the FSM technique is used, it is necessary to continue the calculation by performing spin optimization in order to determine the type of magnetic ordering corresponding to a given energy minimum from a FSM calculation.

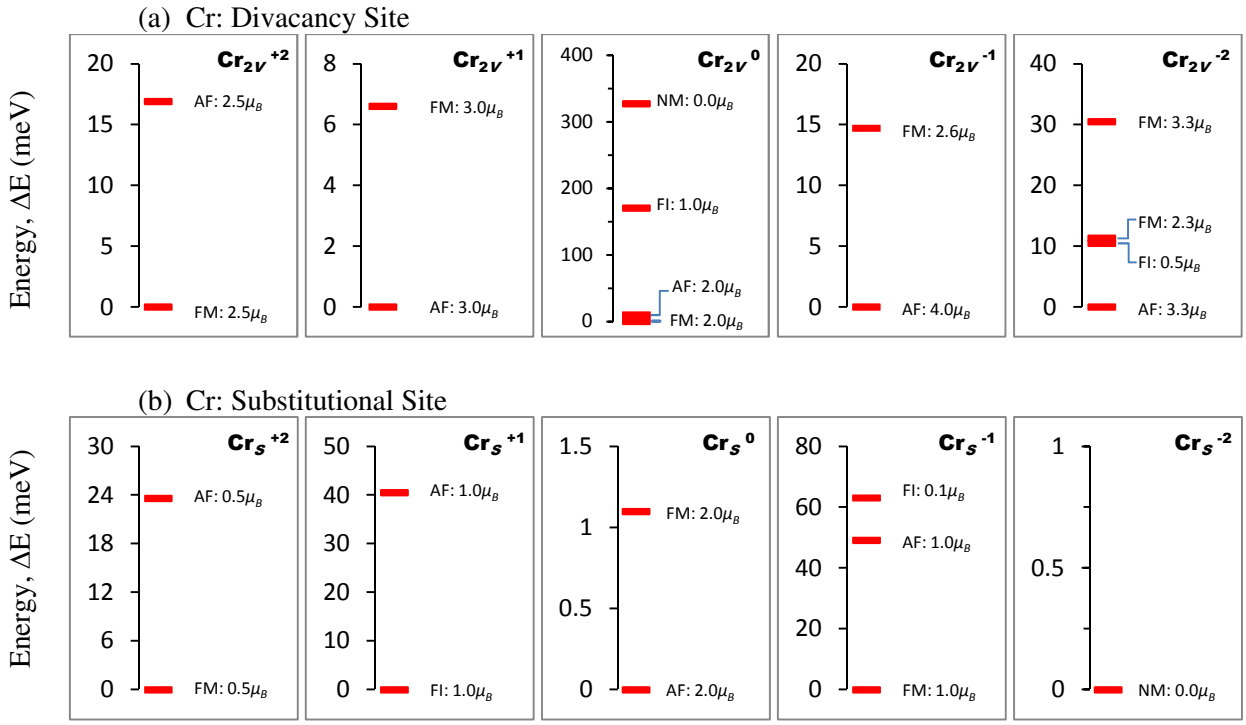

Figure 6.3 (i): Magnetic states of Cr-doped diamond (FM: Ferromagnetic, AF: Antiferromagnetic, FI: Ferrimagnetic, NM: Non-magnetic) for Cr at (a) divacancy and (b) substitutional lattice sites, in charge states +2, +1, 0, -1, -2. The energies are relative to the respective most stable magnetic state. Note the different energy scales for each charge state. Details of each state are summarized in Table 6.1 (i).

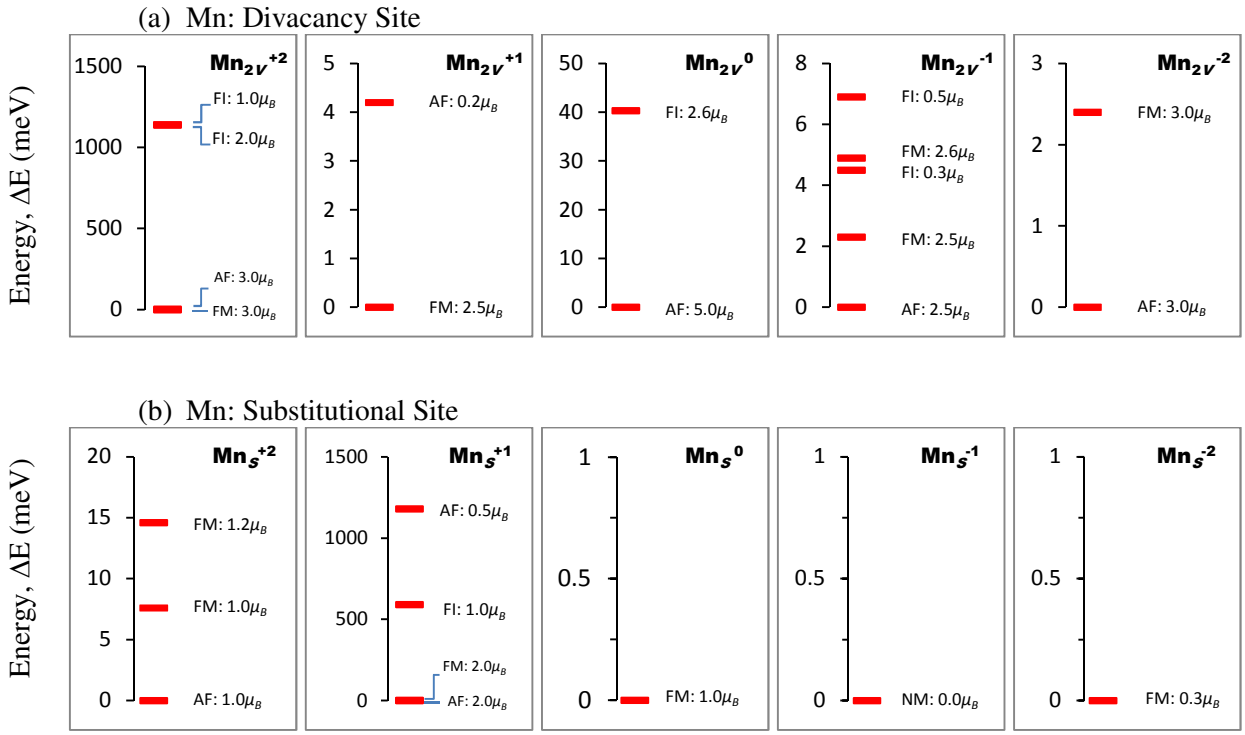

Figure 6.3 (ii): Magnetic states of Mn-doped diamond for Mn at (a) divacancy and (b) substitutional lattice sites, similar to Table 6.3 (i) for chromium. Details of each state are summarized in Table 6.1 (ii).

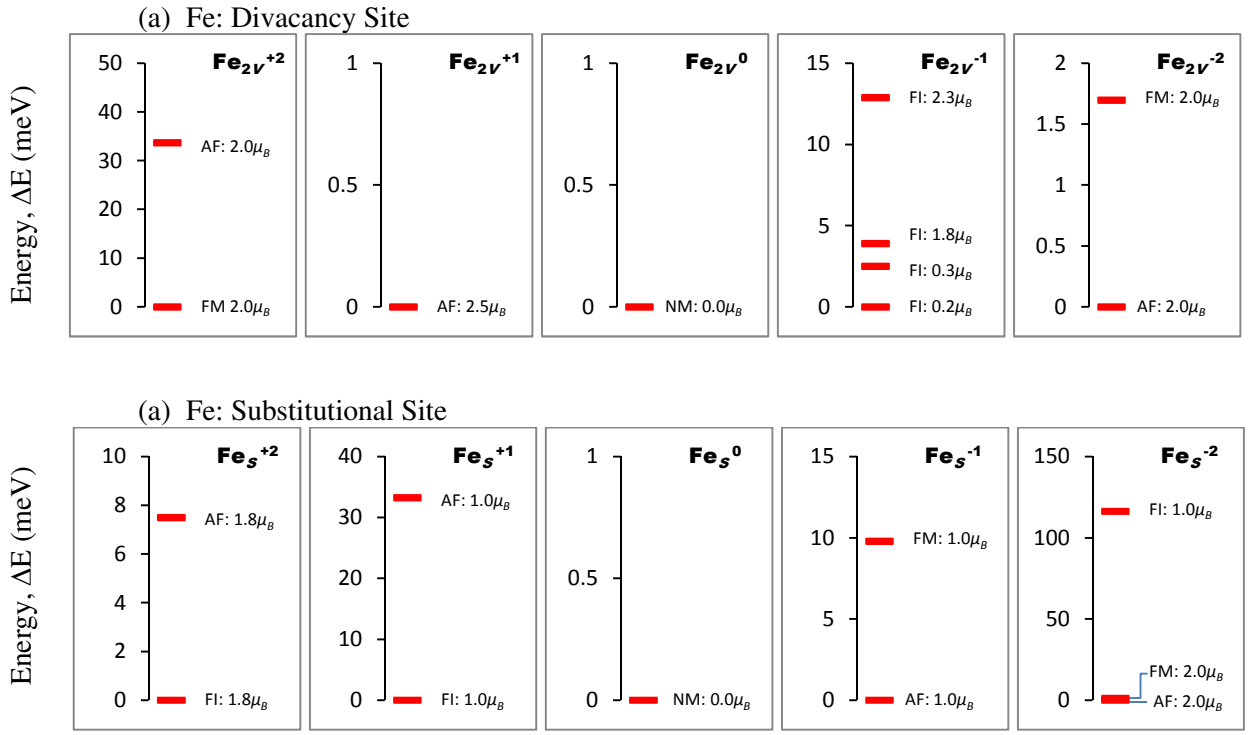

Figure 6.3 (iii): Magnetic states of Fe-doped diamond for Fe at (a) divacancy and (b) substitutional lattice sites, similar to Table 6.3 (i) for chromium. Details of each state are summarized in Table 6.1 (iii).

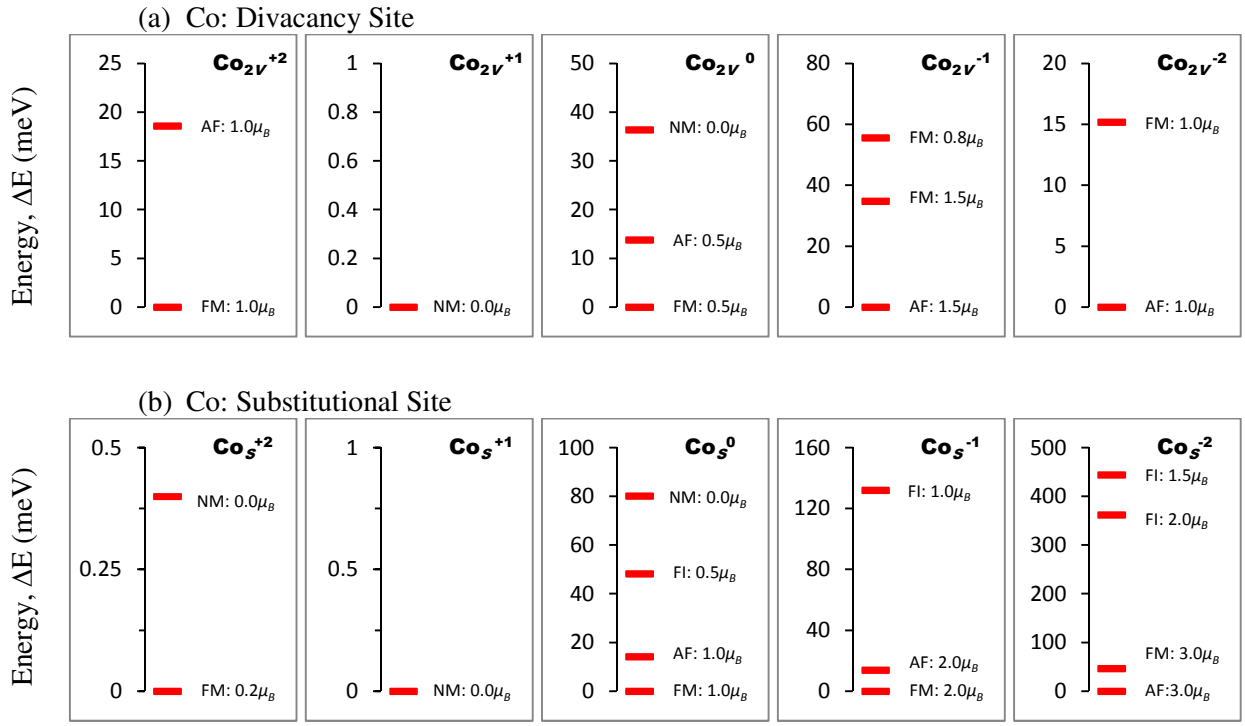

Figure 6.3 (iv): Magnetic states of Co-doped diamond for Fe at (a) divacancy and (b) substitutional lattice sites, similar to Table 6.3 (i) for chromium. Details of each state are summarized in Table 6.1 (iv).

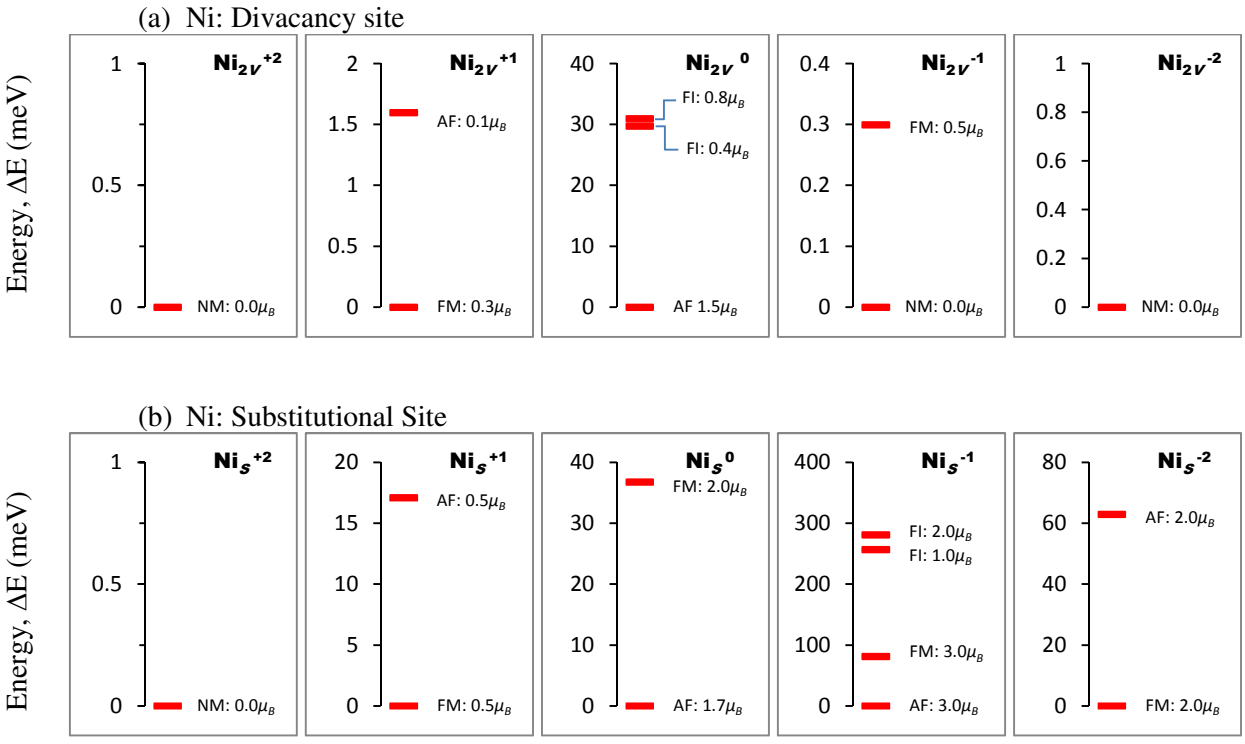

Figure 6.3 (v): Magnetic states of Ni-doped diamond for Ni at (a) divacancy and (b) substitutional lattice sites, similar to Table 6.3 (i) for chromium. Details of each state are summarized in Table 6.1 (v).

6.4.1 Magnetic stabilization energy

Figure 6.4 illustrates the magnetic ground state stabilization energies across the central portion of the 3*d* series, from Cr to Ni, in different charge states ($q = +2, +1, 0, -1, -2$) at the divacancy and substitutional lattice sites in diamond. It is seen that each of these transition metal atoms achieves a ground state with some form of magnetic ordering in at least one charge state.

We find that the ground state magnetic stabilization energies are critically dependent on the charge state, and therefore on the type of doping in diamond (*n*-type, *p*-type, or intrinsic). As a result, the achievable ground state magnetic ordering of transition metal-doped diamond is predicted to be significantly influenced by position of the Fermi level, and thus co-doping with shallow donors or acceptors (such as N, P or B) will play a key role in determining the ground state magnetic ordering properties of transition metals in diamond.

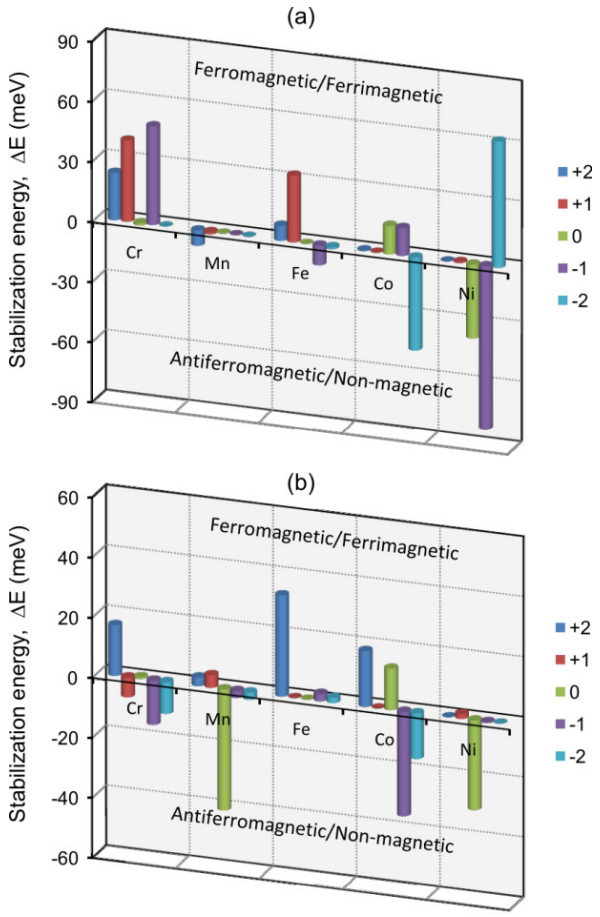

Figure 6.4: Magnetic ground state stabilization energies of 3*d* transition metals in diamond at (a) divacancy and (b) substitutional lattice sites for different charge states $(+2, +1, 0, -1, -2)$. The energies are relative to magnetic ground state in each case.

Table 6.2 provides a list of transition metals and specific charge states in which the ground state magnetic ordering is ferromagnetic or ferrimagnetic. The corresponding details of magnetic stabilization energies, Mean-Field Approximation (MFA) T_C, magnetic moment per impurity ion and the Fermi energy stability range for each charge state are also given. In substitutional Mn^{0}_{S} and Mn^{-2}_{S}, the ferromagnetic spin ordering is found to be the only magnetic state, with magnetic moments of 1.0 μ_B and 0.3 μ_B, without any metastable antiferromagnetic or non-magnetic states, thus suggesting that ferromagnetic ordering could readily be achieved in these cases.

TM defect	Stabilization energy, ΔE (meV)	T_C (K)	Magnetic Moment per TM ion μ_B	Fermi energy stability (eV)
Cr^{+2}_{2V}	16.9	130.7	2.5	0.00 – 0.54
Cr^{+2}_{S}	23.6	182.6	0.5	0.00 – 0.60
Cr^{+1}_{S}	40.5	313.3	1.0	0.60 – 1.18
Cr^{-1}_{S}	49.2	380.6	1.0	4.68 – 5.22
Mn^{+2}_{2V}	2.9	22.4	3.0	0.00 – 0.71
Mn^{+1}_{2V}	4.2	32.5	2.5	0.71 – 1.02
Mn^{0}_{S}	-	-	1.0	1.39 – 3.50
Mn^{-2}_{S}	-	-	0.3	3.50 – 5.49
Fe^{+2}_{2V}	33.7	260.7	2.5	-
Fe^{-1}_{2V}	2.5	19.3	0.2	-
Fe^{-2}_{2V}	1.7	13.1	2.0	2.49 – 5.49
Fe^{+2}_{S}	7.5	58.0	1.8	0.00 – 0.37
Fe^{+1}_{S}	33.3	257.6	1.0	0.37 – 0.98
Co^{+2}_{2V}	18.6	143.9	1.0	-
Co^{0}_{2V}	13.8	106.8	0.5	1.06 – 2.25
Co^{+2}_{S}	0.4	3.1	0.2	0.00 – 0.21
Co^{-1}_{S}	13.9	107.5	2.0	4.28 – 4.39
Ni^{+1}_{2V}	1.6	12.4	0.3	0.50 – 0.82
Ni^{-2}_{S}	63.0	487.4	2.0	4.40 – 5.49

Table 6.2: A list of 3*d* transition metals with ferromagnetic/ferrimagnetic ground states in diamond. $T_C = \Delta E.(2/3\, k_B)$ is the predicted Mean Field Approximation (MFA) Curie temperature. The band gap stability range are energy ranges of Fermi level in the band gap for which the particular charge state will be most stable, with the Fermi level position relative to the top of the valence band maximum (E_V). The T_C values not listed correspond to cases with only ferromagnetic ordering without any other magnetic or non-magnetic states (therefore the Curie temperature cannot be estimated). Fe^{+2}_{2V}, Fe^{-1}_{2V} and Co^{+2}_{2V} charge states are not stable for any position of the Fermi level. Charge states highlighted in bold are the energetically most favourable, hence likely to be achieved in diamond.

However, in order to predict 3*d* transition metal atoms which may potentially lead to non-vanishing magnetic moments (Ferromagnetic or ferrimagnetic ordering) in diamond, the energetic stability of a particular charge state, relative to all other possible charge states and lattice sites (at a particular Fermi energy) must be taken into consideration. For example, substitutional $Cr^{-1}{}_S$ is predicted to order ferromagnetically with a ferromagnetic stabilization energy of 49.2 meV at Fermi energies ranging from 4.68 – 5.22 eV (Figure 4.2), but it is unfortunately higher in energy by 5.0 eV compared to the divacancy site where the antiferromagnetic spin state is favourable, thus making it unlikely to be observed in diamond samples.

In addition to the relative energetic stability of a specific charge state, the magnitude of its ground state magnetic moment should also be as large as possible, and with strongly spin polarized states at the Fermi level so as to sustain significant spin polarization current at high Curie temperatures.

Based on the above criteria, we predict that ferromagnetic/ferrimagnetic ordering of transition metal-doped diamond is likely to be achieved in divacancy: $Cr^{+2}{}_{2V}$ ($\Delta E = 16.9$ meV), $Mn^{+2}{}_{2V}$ ($\Delta E = 2.9$ meV), $Mn^{+1}{}_{2V}$ ($\Delta E = 4.2$ meV), $Co^{0}{}_{2V}$ ($\Delta E = 13.8$ meV) and substitutional: $Fe^{+2}{}_S$ ($\Delta E = 7.5$ meV), $Fe^{+1}{}_S$ ($\Delta E = 33.3$ meV), which are advantageously most stable in *p*-type B-doped diamond ($E_V + 0.37$ eV), except $Co^{0}{}_{2V}$ which is most stable at Fermi levels in the mid-range of the diamond band gap. Therefore, co-doping with B is likely to result in an increase of charge concentration, which may potentially lead to mediation of ferromagnetic exchange interactions [123]. However, we note that the ferromagnetic and anti-ferromagnetic spin sates in divacancy $Mn^{+1}{}_{2V}$, $Mn^{+1}{}_{2V}$ and substitutional $Co^{+2}{}_S$ are at approximately equal energies, with the ferromagnetic spin state being more stable by only <5 meV, suggesting that ferromagnetic ordering in these cases will only persist up to very low temperatures. In divacancy $Co^{0}{}_{2V}$, the Fermi level stability range is 1.06 – 2.25 eV above the diamond valence band and therefore achieving a ferromagnetic response in Co-doped intrinsic diamond will require Fermi level engineering to pin the Fermi to within these Fermi energies.

In addition to the above results of predicted ferromagnetic ordering in transition metal-doped diamond, substitutional $Fe^{+1}{}_S$ presents a special case whereby states at the Fermi level possess a half-metallic character, with a magnetic moment of 1.0 μ_B per Fe^{+1} ion, consistent with the condition of spin integer magnetic moment for half-metals [234]. Similarly, the calculated

magnetic moment in divacancy $Mn^{+2}{}_{2V}$ is an integer spin of 3.0 μ_B per Mn^{+2} ion, although we note that the ferromagnetic spin state is lower in energy by only 2.7 meV compared to the antiferromagnetic spin state, which will most likely lead to antiferromagnetic spin alignment, even at low temperatures.

We note that the stabilization energies between different magnetic states discussed in this Thesis describe the magnetic interactions only at TM-TM separations of $2a_0$. To evaluate the effect of TM-TM separation on magnetic ordering and stabilization energies, we repeated representative calculations for Co^0 and Cr^{+2} at both the divacancy and substitutional site with a reduced separation of one lattice constant (3.569 ˚A). We find that although the induced magnetic moment is independent of the TM-TM separation, the total energy is slightly higher at the reduced separation (by $0.02 - 0.05$ eV) due to increased elastic energy resulting from the large size of the transition metal atoms relative to C-C bond length.

Importantly, the ground state spin coupling in these cases is antiferromagnetic at the closer TM-TM separation (3.569Å), in contrast to ferromagnetic coupling at the larger 7.138 Å separation discussed above, indicating that clustering will be detrimental to ferromagnetic ordering in transition metal doped, similar to what has been predicted for transition metal-doped GeN [235]. However, this result is unlikely to affect the magnetic ordering properties of transition metals in diamond since the increased energy at closer transition metal separations will likely oppose clustering.

6.4.2 Estimated Curie temperatures

The magnetic stabilization energy, ΔE measures the relative energetic stability of parallel spin ordering (ferromagnetic) versus anti-parallel spin ordering (anti-ferromagnetic), $\Delta E = E_{FM} - E_{AF}$, and is proportional to the Curie temperature T_C of a diluted magnetic semiconductor [91], as discussed in Section 2.5.4.

Within the Mean Field-Approximation (MFA) [91], $T_C = \Delta E.(2/3\,k_B)$, where k_B is the Boltzmann constant and ΔE is a function of impurity concentration (and therefore impurity separation) which is assumed to be uniform throughout the semiconductor matrix [91]. From Table 6.2, we therefore predict that $Cr^{+2}{}_{2V}$ and $Fe^{+1}{}_{S}$, both in p-type diamond, and $Co^{0}{}_{2V}$ in intrinsic diamond are likely to order ferromagnetically at significantly high Curie temperatures compared to other DMS which have been studied so far (at comparable

impurity concentrations) [225], including the prototype DMS Mn-doped GaAs [236], in which a ferromagnetic stabilization energy (with respect to paramagnetic ordering) of < 3 meV has been found at 5% Mn impurity concentration [91].

6.4.3 Ferromagnetic stabilization

To understand the differences between ferromagnetic over antiferromagnetic stabilization in transition metal-doped diamond, Figure 6.5 presents a plot of the atomic partial density of states (PDOS) for ferromagnetic and antiferromagnetic divacancy Cr^{+2} and Mn^{+1}, illustrating hybridization of carbon 2*s*, 2*p* and transition metal 3*d* orbitals. An important difference between the density states of ferromagnetic and antiferromagnetic spin alignment is the energy mismatch between the spin-up and spin-down bands. The energy mismatch at the Fermi level in ferromagnetic spin configurations leads to band filling predominantly in one spin direction, while the other spin direction is occupied by a fewer number of electrons. This leads to spin polarisation in accordance with the Stoner model of ferromagnetism [218,237,238], and thus, if the density of states at the Fermi level is large enough, many electrons can occupy higher energy states above the Fermi energy in one spin direction. Therefore, the exchange interaction energy between overlapping electron states with opposite spin directions favours ferromagnetic over antiferromagnetic stabilization [239].

In the corresponding antiferromagnetic configurations, the exchange splitting in both spin directions is balanced by the crystal field (i.e. the total spin-up and spin-down density of states are symmetric in energy) and thus any remaining electrons above the Fermi level are accommodated equally in both spin directions as guided by Pauli's exclusion principle, resulting in a net magnetic moment of zero.

Further, we observe that the amplitude of the 3*d* partial density of states per unit energy of the main peak in the ferromagnetic configuration is higher than that of the antiferromagnetic configuration (Figure 6.5). In addition, the 3*d* orbitals in ferromagnetic cases hybridize with the C-2*p* orbitals in valence band, suggesting that co-doping with shallow acceptors such as Boron ($E_V + 0.37$ eV) will lead to an increase in hole concentration, which is likely to promote stronger ferromagnetic stabilization interactions [123].

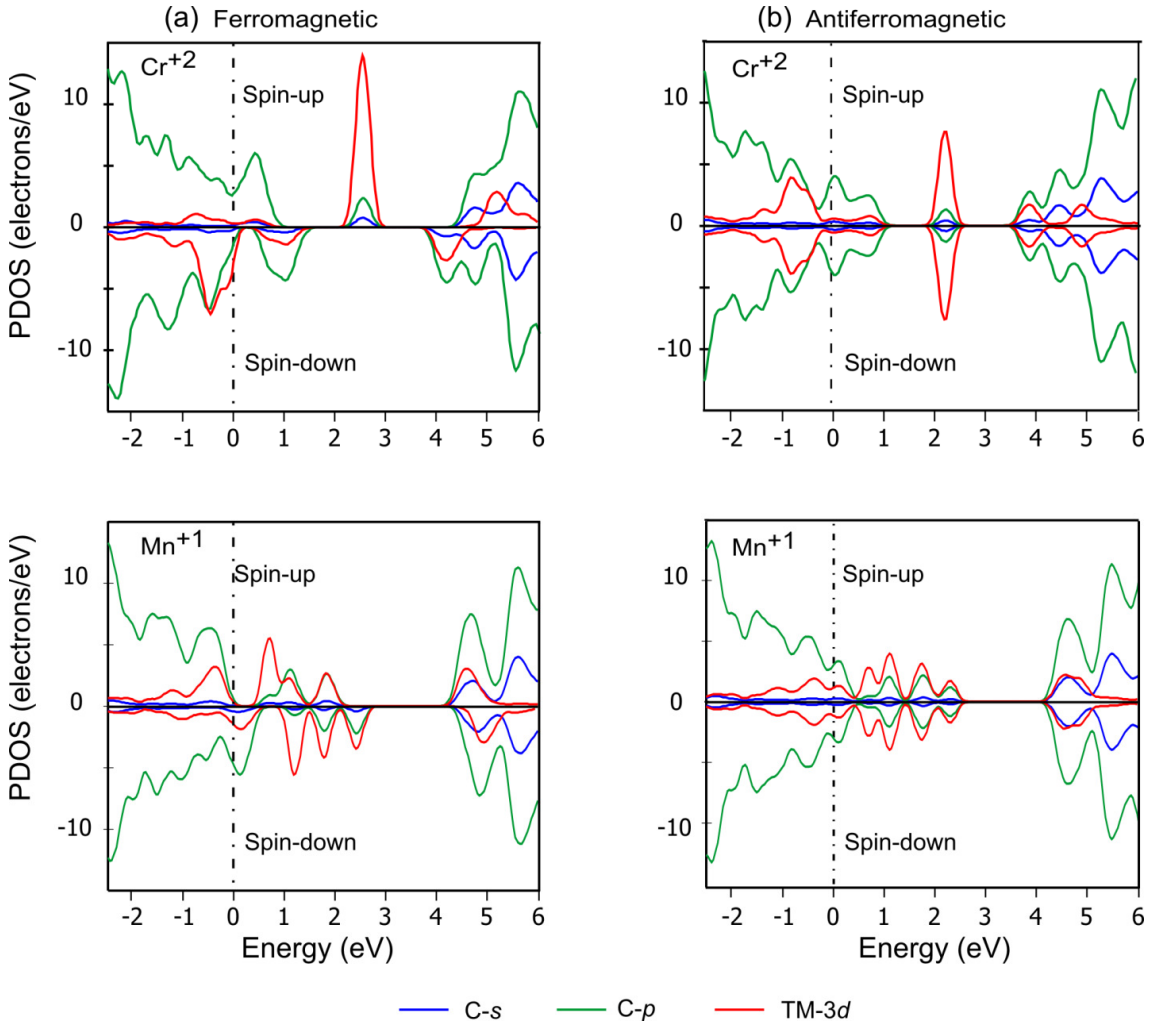

Figure 6.5: Partial density of states (PDOS) for divacancy $Cr^{+2}$and Mn^{+1} in diamond showing (a) Ferromagnetic and (b) Antiferromagnetic interactions. The energies are relative to the Fermi energy shown with the vertical dashed line.

6.5 Half-metallic ferromagnetic ordering in Fe-doped diamond

Half-metallic ferromagnetic semiconductors (HMFS) by definition have got only one spin component available for conduction of charge at the Fermi level, with the Fermi level crossing bands for only one spin orientation [240]. For this reason, HMFS are potentially of considerable interest in spintronic device applications (such as memory devices and computer processors [241]) for injection and transport of highly spin polarised currents [234,240-242][241]. HMFS have theoretically been predicted in many materials, mainly in ternary compounds including Fe_3O_4, Co_2MnSi, NiMnSb and the binary compound CrO_2, but low Curie temperatures and lack of other fundamental material properties [4] has remained a major challenge towards practical implementation in room temperature device applications.

Among the 3*d* transition metals which have been demonstrated in the present study to order ferromagnetically in diamond (Table 6.2), substitutional $Fe^{+1}{}_S$ presents an exceptional case with the highest ferromagnetic stabilization energy of 33.3 meV, and most significantly, exhibits half-metallic ferromagnetic ordering of states at the Fermi level. The half-metallic character of states at the Fermi level in substitutional Fe^{+1} occurs because the exchange splitting is greater than the occupied bandwidth of the spin-up electrons, so that the Fermi level only passes through the spin-up bands, similar to CrO_2 [238] in which experimental evidence for half-metallicity is strongest [238,241-243]. As a consequence, the spin-up electrons at the Fermi level are 100% spin polarized (therefore conduction electrons will exclusively have the spin-up component). This result implies that electronic transport in Fe-doped diamond will take place only in the spin-up band, with the spin-down band acting as an insulator for the spin-down electrons, as depicted by the total density of states and band structure plots in Figure 6.6.

Another remarkable result in substitutional $Fe^{+1}{}_S$ is that its band gap stability range lies between 0.37 – 0.98 eV above the valence band maximum (within which it remains the most stable form of Fe in diamond), and therefore is most likely to achieved in B-doped *p*-type diamond (E_V + 0.37 eV). In addition, $Fe^{+1}{}_S$ will most likely hybridize with the boron acceptors in diamond which may result in an increase carrier concentration, and hence promote stronger ferromagnetic exchange interactions due to hole mediation.

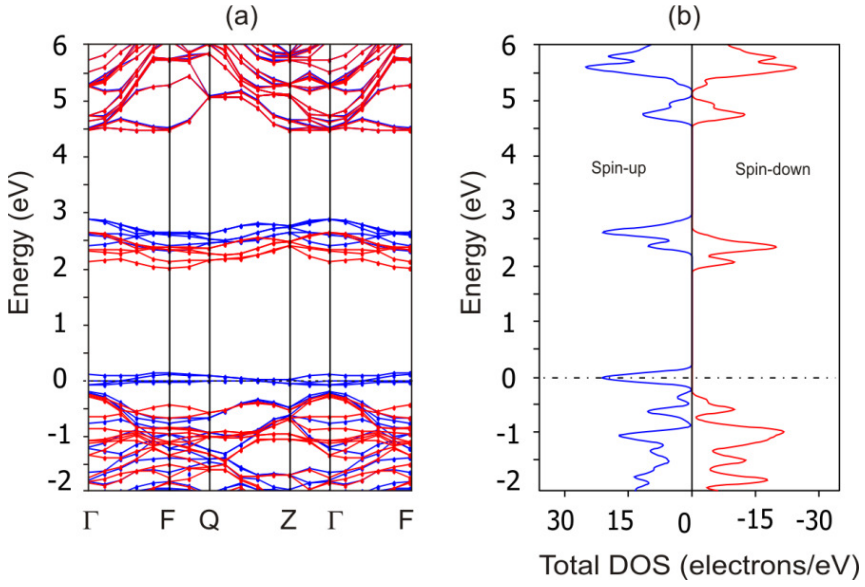

Figure 6.6: (a) Band structure and (b) Total DOS for substitutional $Fe^{+1}{}_S$ in diamond (drawn from a 128-atom diamond supercell) showing spin polarized states with half-metallic character at the Fermi level. Energies are relative to the Fermi level shown with the horizontal dashed lines, respectively.

7. Summary and conclusions

In this Thesis, the energetic stability of 3*d* transition metals and their magnetic ordering properties at different lattice sites and charge states in diamond have been investigated using *ab* initio pseudopotential density functional methods. The study considers for the first time, the effect of impurity charge states on the magnetic properties of 3*d* transition metals in diamond, showing that both the spin polarisation and the magnetic stabilization energies are critically dependent on the charge state and the position of the Fermi level in diamond.

Across the 3*d* series of transition metals, from Sc to Zn, a distinctive trend of the energetic stability at the divacancy, substitutional, hexagonal interstitial and tetrahedral interstitial lattice sites is seen, with the formation energies of transition metals in the middle of the series at any charge state ($q = 2, +1, 0, -1, -2$) being considerably lower compared to those early or late in the series. We find that the majority of transition metals at any charge state are energetically stable at the divacancy site compared to substitutional or interstitial or lattice sites, while transition metals at the interstitial sites are highly unstable (by ~8 eV compared to the divacancy site), hence making the interstitial species unlikely to be achieved in significant concentrations.

Importantly, the energetic stability of all the 3*d* transition metals in diamond is found to be strongly dependent on their charge state, and therefore on the position of the Fermi level or type of doping (intrinsic, *n*-type or *p*-type). At any lattice site, the formation energies are predicted to be lower in *p*-type (B-doped) or *n*-type (N- or P-doped) diamond compared to intrinsic diamond, thus indicating that co-doping with boron, nitrogen or phosphorus, which are the most common dopants in diamond, will considerably enhance the energetic stability of transition metals in diamond.

Further, we find that 3*d* transition metals occupying divacancy and substitutional lattice sites induce deep donor and acceptor levels in the diamond band gap, thus underscoring the fact that their electronic and magnetic properties in diamond will be strongly dependent on their charge state. The magnitude of the induced magnetic moments is also found to depend on the

doping site and charge state, with the different charge states inducing non-vanishing magnetic moments in diamond, thus indicating that transition metal impurities may lead to collective magnetic ordering when incorporated into the diamond lattice.

Incorporation of single transition metal impurities into diamond is found to introduce spin polarised impurity bands into the diamond band gap while maintaining the semiconducting nature of diamond, with band gaps in both spin channels. These impurity bands are seen to originate mainly from $s, p - d$ hybridization between carbon sp^3 orbitals and the $3d$ orbitals of the transition metal atoms. In addition, we find the $4p$ orbitals of the transition metals at substitutional sites also contribute to hybridization, but not at the divacancy site, indicating that that the magnetic nature of $3d$ transition metal-doped diamond will also be dependent on the occupied lattice site, and hence on the local symmetry around the transition metal impurity.

Further, by considering spin interactions between transition metal atoms in diamond to determine the energetically most stable magnetic odering state as a function of charge state and lattice site, we find the magnetic stability and ordering to be critically dependent on the charge state and lattice site. This suggests that magnetic ordering of transition metal-doped diamond will depend significantly on the position of the Fermi level in the diamond band gap, and therefore on the type of doping (*n*-type, *p*-type or intrinsic) in diamond, thus indicating that co-doping with shallow donors or acceptors (such as N, P or B) will play a key role in influencing the spin properties of transition metal defects in diamond.

Based on the energetic stability of the various charge states and lattice sites, as well as their ground state magnetic moments, magnetic ordering and stabilization energies (ΔE), we find that ferromagnetic ordering of transition metal-doped diamond is likely to be achieved in divacancy: $Cr^{+2}{}_{2V}$ ($\Delta E = 16.9$ meV; $2.5\ \mu_B$), $Mn^{+2}{}_{2V}$ ($\Delta E = 2.9$ meV; $3.0\ \mu_B$), $Mn^{+1}{}_{2V}$ ($\Delta E = 4.2$ meV; $2.5\ \mu_B$), and $Co^{0}{}_{2V}$ ($\Delta E = 13.8$ meV; $0.5\ \mu_B$), and in substitutional: $Fe^{+2}{}_{S}$ ($\Delta E = 7.5$ meV; $1.8\ \mu_B$) and $Fe^{+1}{}_{S}$ ($\Delta E = 33.3$ meV; $1.0\ \mu_B$). Importantly, these results predict that transition metal-doped diamond is likely to order ferromagnetically at significantly high Curie temperatures compared to other diluted magnetic semiconductors (DMS) which have been studied so far (at comparable impurity concentrations) [225], including the prototype DMS Mn-doped GaAs [236], in which a ferromagnetic stabilization

energy (with respect to paramagnetic ordering) of < 3 meV has been found at 5% Mn impurity concentration [91]. Advantageously, the Fermi level stability range of the above charge states corresponds to *p*-type diamond, except for divacancy Co^0 (which is most stable at Fermi levels in the middle of the diamond band gap). In addition, co-doping with shallow acceptors such as B ($E_V + 0.37$ eV) is likely to result in an increase of charge concentration, which has been demonstrated to play a key role in mediating ferromagnetic exchange interactions in other semiconductors [123]. In divacancy Co^0, the Fermi level stability range is 1.06 – 2.25 eV above the diamond valence band, and therefore Fermi level engineering will be needed to achieve a ferromagnetic response in Co-doped diamond.

The magnetic interaction in the above cases is ferromagnetic at the considered transition metal impurity separation of two diamond lattice constants (7.138 Å), while at closer separations of one lattice constant (3.569 Å), selected cases show that the interaction becomes antiferromagnetic, implying that clustering will be detrimental to ferromagnetic ordering in transition metal-doped diamond.

Substitutional $Fe^{+1}{}_S$ presents an interesting case of ferromagnetic diamond with the highest ferromagnetic stabilization energy of 33.3 meV, and most importantly, exhibits half-metallic ordering of states at the Fermi level, with a magnetic moment of 1.0 μ_B per Fe^{+1} ion. As a consequence, conduction electrons at the Fermi level will be 100% spin polarized, implying that electronic transport in Fe-doped diamond will take place in bands of only one spin direction, with bands of the other spin direction acting as an insulator.

In addition to diamond's extreme properties, the results presented in this Thesis demonstrate that transition metal-doped diamond could form a stable diluted magnetic semiconductor which may order ferromagnetically at high Curie temperatures, and is likely to have significant applications in the emerging field of spintronics.

8. References and Bibliography

[1] K. Sato, P.H. Dederics, and H.K. Yoshida, Europhys. Lett. 61 (2003) 403.

[2] T. Story, R.R. Galazka, R.B. Frankel, and P.A. Wolff, Phys. Rev. Lett. 57 (1986) 777.

[3] S.J. Pearton, D.P. Norton, M.P. Ivill, A.F. Herbard, J.M. Zavada, W.M. Chen, and I.A. Buyanova, J. Electr. Mater. 36 (2007) 462.

[4] S.A. Wolf, D.D. Awschalom, R.A. Buhrman, J.M. Daughton, S. von Molnar, M.L. Roukes, A.Y. Chatcehlkanova, and D.M Treger, Science 294 (2001) 1488.

[5] Y. Matsumoto, M. Murakami, T. Shono, T. Hasegawa, T. Fukumura, M. Kawasaki, P. Ahmet, T. Chikyow, S. Koshikara, and H. Koinuma, Science 291 (2001) 854.

[6] J.D.H. Donnay and H.M. Ondik, *Crystal Data: Determinative Tables vol 2, 3rd ed.* (US Department of Commerce - National Bureau of Standards - JCPDS, 1973).

[7] J.E. Field, *The Properties of Natural and Sythetic Diamond:* Academic Press, London (1992).

[8] J.R. Weber, W.F. Koehl, J.B. Varley, A. Janotti, B.B. Buckley, C.G. Van de Walle, and D.D. Awschalom, Proc. Nat. Acad. Sci. 107 (2010) 8513.

[9] I. Aharonovich and S. Prawer, Diamond Rel. Mater. 19 (2010) 729.

[10] I. Aharonovich, C. Zhou, A. Stacey, J. Orwa, S. Castelletto, D. Simpson, A.D. Greentree, F. Treussart, J.F. Roch, and S. Prawer, Phys. Rev. B 79 (2009) 235316.

[11] G. Balasubramanian, P. Neumann, and D. Twitchen, Nature Mater. 8 (2009) 383.

[12] N.B. Manson and R.L. McMurtrie, J. Lumin 127 (2007) 98.

[13] A.M. Zaitazev, *Optical properties of diamond: A data hand book* (Springer, 2001).

[14] M. O'Donoghue, *Gems: their sources, descriptions and identification* (Oxford, Butterworth-Heinemann, 2006).

[15] P.W. May, Science 319 (2008) 1490.

[16] Diamond materials-company, *The CVD diamond booklet* (www.diamond materials.com/download (Accessed November 2011).

[17] J. Isberg, J. Hammersberg, E. Johansson, T. Wikström, D.J. Twitchen, A.J. Whitehead, S.E. Coe, and G.A. Scarsbrook, Science 297 (2002) 1670.

[18] M. Geis, Mat. Res. Soc. Symp. Proc. 152 (1990) 15.

[19] J.H. Wort and R.S. Balmer, Mater. Today 11 (2008) 22.

[20] R. Kalish, J. Phys. D: Appl. Phys 40 (2007) 6467.

[21] M.I. Katsnelson, V.Yu. Irkhin, L. Chioncel, A.I. Lichtenstein, and R.A. de Groot, Rev. Mod. Phys. 80 (2008) 315.

[22] J. Kohanoff, *Electronic Structure Calculations for Solids and Molecules* (Cambridge University Press, UK, 2006).

[23] E.B. Lombardi, *A Quantum Mechanical Study of Dopants in Diamond:* University of South Africa, (2003).

[24] J.R. Chelikowsky, T. Kaxiras, and R.M. Wentzcovitch, Phys. Stat. Sol. (b) 243 (2006) 2133.

[25] D. Hamann, R. Schluter, and M. Chiang, Phys. Rev. Lett. 43 (1979) 1494.

[26] R.M. Martin, *Electronic Structure: Basic theory and practical methods* (Cambridge University Press, UK, 2006).

[27] P. Hohenberg and W. Kohn, Phys. Rev. 136 (1964) 864.

[28] F.L. Pilar, *Elementary Quantum Chemistry* (McGraw-Hill, New York, 1990).

[29] A. Szabo and N.S. Ostlund, *Modern Quantum Chemistry* (McGraw-Hill, New York, 1989).

[30] I.N. Levine, *Quantum Chemistry* (Prentice-Hall, Englewood Cliffs, NJ, 1991).

[31] S. Cottenier, *Density Functional Theory and the Family of (L)APW- Methods: A Step-by-Step in-Introduction:* Instituut voor Kern- en Stralingsfysica,Belgium (2002).

[32] J. Singh, *Planewaves, Pseudopotentials and the LAPW Method* (Kluwer academic, Boston, 1994).

[33] S. Fabris, S. de Gironcoli, S. Baroni, G. Vicario, and G. Balducci, Phys. Rev. B 71 (2005) 041102(R).

[34] K. Schwarz and P. Mohn, J. Phys. F: Met. Phys. 14 (1984) L129.

[35] R. Zeller, Comput. Nanoscience 31 (2006) 419.

[36] D.C. Langreth and M.J. Mehl, Phys. Rev. B 28 (1983) 1809.

[37] D.C. Langreth and M.J. Mehl, Phys. Rev. Lett. 47 (1981) 446.

[38] K. Schwartz and P. Blaha, Comp. Mater. Science 28 (2003) 269.

[39] S. Tosoni, C. Tuma, J. Sauer, B. Civalleri, and P. Ugliengo, J. Chem. Phys. 127 (2007) 154102.

[40] M. Segall, *an Ab Initio Study of Biological Systems:* University of Cambridge, (1997).

[41] S.J. Clark, M.D. Segall, C.J. Pickard, P.J. Hasnip, M.J. Probert, K. Refson, and M.C. Payne, Zeitschrift fuer Kristallographie 220 (2005) 567.

[42] O.K. Anderson, Phys. Rev. B 12 (1975) 3060.

[43] D.D. Koelling and G.O. Arbman, J. Phys. F (Metal Phys.) 5 (1975) 2041.

[44] J. Grotendorst, S. Blugel, and D. Marx, *Full Potential Linearized Augmented Plane Wave Method, Computational Nano Science: Do it Yourself:*, 31(2006) 85.

[45] T. Sasaki, A.M. Rappe, and S.G. Louie, Phys. Rev. B 52 (1995) 12760.

[46] P. Blaha, K. Schwarz, G.K.H. Madsen, D. Kvasnicka, and J. Luitz, WIEN2k An Augmented PlaneWave + Local Orbitals Program for Calculating Crystal Properties, Techn. Universität Wien, Austria, 2008.

[47] M. Fuchs, J.I.F. Da Silva, C. Stampfl, J. Neugebauer, and M. Scheffler, Phys. Rev. B 65 (2002) 245212.

[48] V. Milman, B. Winkler, J.A. White, C.J. Pickard, M.C. Payne, E.V. Akhmatskaya, and R.H. Nobes, Int. J. Quantum Chem. 77 (2000) 895.

[49] K. Laasonen, A. Pasquarello, R. Car, C. Lee, and D. Vanderbilt, Phys. Rev. B 47 (1993) 10142.

[50] R. Car and M. Parrinello, Phys. Rev. Lett. 55 (1985) 2471.

[51] R. Natarajan and D. Vanderbilt, J. Comput. Phys. 82 (1989) 218.

[52] L. Kleinman and D.M. Bylander, Phys. Rev. Lett. 48 (1982) 1425.

[53] D. Vanderbilt, Phys. Rev. B 41 (1990) 7892.

[54] S.G. Louie, S. Froyen, and M.L. Cohen, Phys. Rev. B 26 (1982) 1738.

[55] J.H. Cho and M. Scheffler, Phys. Rev. B 53 (1996) 10685.

[56] S. Fabris, S. de Girancoli, S. Baroni, G. Vicario, and G. Balducci, Phys. Rev. B 72 (2005) 237102.

[57] K.K. Irikura and D.J. Frurip, *Computational Thermochemistry: Prediction and Estimation of Molecular Thermodynamics :* American Chemical Society, Washington DC (1998).

[58] H. Li, L. Shi, M. Zhang, Z. Su, X. Wang, l. Hu, and G. Chen, J. of Chem. Phys. 126 (2007) 144101.

[59] L.H. Hu, X.J. Wang, L.H. Wong, and G. H. Chen, J. Chem. Phys. 119 (2003) 11501.

[60] X. Zheng, L.H. Hu, X.J. Wang, and G.H. Chen, Chem. Phys. Lett. 390 (2004) 186.

[61] N.D.M. Hine, K. Frensh, W.M.C. Foulkes, and M.W. Finnis, Phys. Rev. B 79 (2009) 024112.

[62] C.G. Broyden, SIAM J. Appl. Math. 6 (1970) 222.

[63] R. Fletcher, The Computer Journal 13 (1970) 317.

[64] D. Goldfarb, SIAM J. Appl. Math. 24 (1970) 23.
[65] D.F. Shanno, Math. Comp. 24 (1970) 647.
[66] J.M. Rondinelli, B. Deng, and L.D. Marks, Comp. Mater. Science 40 (2007) 345.
[67] M.L. Cohen, M. Shluter, J.R. Chelikowsky, and S.J. Louie, Phys. Rev. B 12 (1975) 5575.
[68] A.F. Kohan, G. Ceder, D. Morgan, and C.G. Van de Walle, Phys. Rev. B 61 (2000) 15019.
[69] A. Zunger and C. Kilic, Phys. Rev. Lett. 88 (2002) 095501.
[70] A. Togo, F. Oba, I. Tanaka, and K. Tatsumi, Phys. Rev. B 74 (2006) 195128.
[71] S.B. Zhang, S.H. Wei, and A. Zunger, Phys. Rev. B 63 (2001) 075205.
[72] C.G. Van de Walle and J. Neugebauer, J. Appl. Phys. 95 (2004) 3851.
[73] S.C. Erwin and C.S. Hellberg, Phys. Rev. B 68 (2003) 245206.
[74] D.A. Drabold and S.K. Estreicher, *Theory of Defects in Semiconductors:* Spinger,Verlag (2007).
[75] C.O. Almbladh and U. von Barth, Phys. Rev. B 31 (1985) 3231.
[76] J.W. Jeong and A. Oshiyama, Phys. Rev. B 64 (2001) 235204.
[77] G.A. Baraff, E.O. Kane, and M. Schluter, Phys. Rev. B 21 (1980) 5662.
[78] C. Stampfl, C.G. Van de Walle, D. Vogel, P. Kruger, and J. Pollman, Phys. Rev. B 61 (2000) R7846.
[79] J.P. Goss, R.J. Eyre, and P.R. Briddon, Phys. Stat. Sol. (b) 245 (2008) 1679.
[80] G. Makov and M.C. Payne, Phys. Rev. B 51 (1995) 4014.
[81] H. Nozaki and S. Itoh, Phys. Rev. E 62 (2000) 1390.
[82] U. Gerstmann, P. Deak, R. Rurali, B. Aradi, T. Frauenheim, and H. Overhof, Physica B (2003) 340 & 190.
[83] C.W.M. Castleton and S. Mirbt, Phys. Rev. B 70 (2004) 195202.
[84] J. Shim, E.K. Lee, Y.J. Lee, and R.M. Nieminen, Phys. Rev. B 71 (2005) 035206.
[85] C.W.M. Castleton, A. Hoglund, and S. Mirbt, Phys. Rev. B 73 (2006) 035215.
[86] P. Erhart, K. Albe, and A. Klein, Phys. Rev. B 73 (2006) 205203.
[87] F. A. Kroger, *The Chemistry of Imperfect Crystals* (North Holland, Amsterdam, 1964).
[88] J. Shim, E. K. Lee, Y. J. Lee, and R. M. Nieminen, Phys. Rev. B 71 (2005) 035206.
[89] J.P. Perdew, K. Burke, and M. Ernzerhof, Phys. Rev. Lett. 77 (1996) 3865.
[90] H.J. Monkhorst and J.D. Pack, Phys. Rev. B 13 (1976) 5188.
[91] K. Sato, L. Bergqvist, J. Kudrnovsky*, et al*, Rev. Mod. Phys. 82 (2010) 1633.
[92] L. Kronik, M. Jain, and J.R. Chelikowsky, Phys. Rev. B 66 (2002) 041203(R).
[93] V. Pardo, P. Blaha, M. Iglesias K. Schwarz, D. Baldomir, and J.E. Arias, Phys. Rev. B 70 (2004) 144422.
[94] J.O. Guille´n, S. Lany, S.V. Barabash, and A. Zunger, Phys. Rev. Lett. 96 (2006) 107203.
[95] L. Bergqvist, O. Eriksson, J. Kudrnovský, V. Drchal, A. Bergman, L. Nordström, and I. Turek, Phys. Rev. B 72 (2005) 195210.
[96] T. Fukushima, K. Sato, H.K. Yoshida, and P.H. Dederichs, Jpn. J. Appl. Phys. 43 (2004) L1416.
[97] K. Sato, W. Schweika, P.H. Dederichs, and H.K. Yoshida, Phys. Rev. B 70 (2000) 201202(R).
[98] L. Kronik, M. Jain, and J.R. Chelikowsky, Phys. Rev. B 66 (2002) 041203.
[99] K. Osuch, E.B. Lombardi, and L. Adamowicz, Phys. Rev. B 71 (2005) 165213.
[100] K. Osuch, E.B. Lombardi, and W. Gebicki, Phys. Rev. B 73 (2006) 075202.
[101] A. Los and V. Los, J. Phys. : Condens. Matter 22 (2010) 245801.
[102] M. Berciu and R.N. Bhatt, Phys. Rev. Lett. 87 (2001) 108203.
[103] R.N. Bhatt, M. Berciu, M.D. Kennett, and X. Wan, J. Supercond. : Incorp. Novel Magn. 15 (2002) 71.

[104] S.J. Pearton, C.R. Abernathy, D.P. Norton, A.F. Hebard, Y.D. Park, L.A. Boatner, and J.D. Budai, Materials Science and Engineering: R: Reports 40 (2003) 137.

[105] L. Bergqvist, O. Eriksson, J. Kudrnovsky, P. Korzhavyi, V. Drchal, and I. Turek, Phys. Rev. Lett. 93 (2004) 137202.

[106] O. Eriksson, D. Iuşan, R. Knut, and B. Sanyal, J. Appl. Phys. 101 (2007) 09H114.

[107] A. Zunger and S. Lany, Physics 3 (2010) 53.

[108] G. Binasch, P. Grinberg, F. Saurenbach, and W. zinn, Phys. Rev. B 39 (1989) 4828.

[109] S.J. Perton, C.R. Albernathy, D.P. Norton, A.F. Herbard, Y.D. Park, L.A. Boatner, and J.D. Budai, Mat. Sc. and Eng. 137 (2003) R40.

[110] S.J. pearton, M.E Overberg, C.R. Abernathy*, et al*, J. Appl. Phys 92 (2002) 2047.

[111] H. Ohno and F. Matsukura, Sol. St. Comm. 117 (2001) 179.

[112] G.A. Medvedkin, K. Hirose, T. ishibashi, T. Nishi, V.G. Voevodin, and K.Sato , J. Cryst. Growth 236 (2002) 609.

[113] J.K. Furdyna, Jpn. J. Appl. Phys. 64 (1988) R29.

[114] A. Haury, A. Wasiela, A. Arnoult, J. Cibert, S. Tatarenko, T. Dietl, and Y. M. d'Aubigne , Phys. Rev. Lett. 79 (1997) 511.

[115] Y. Fukuma, H. Asada, J. Miyashita, N. Nishimura, and T. Koyanagi, J. Appl. Phys. 93 (2003) 7667.

[116] M. Henini, III-Vs Review 13 (2000) 32.

[117] M.K. Jain, *Diluted Magnetic Semiconductors:* World Scienntific, (1991).

[118] H. Munekata, H.Ohno, S. Von Molnar, A. Segmuller, L.L. Chang, and L. Esaki, Phys. Rev. Lett. 63 (1989) 1849.

[119] H. Ohno, H. Munekata, T. Penny, S. Von Monar, and L.L. Chang, Phys. Rev. Lett. 68 (1992) 2664.

[120] H. Ohno, A. Shen, F. Matsukura, A. Oiwa, A. Endo, S. Katsumoto, and Y. Iye, Appl. Phys. Lett. 69 (1996) 363.

[121] T. Dietl, H. Ohno, F. Matsukura, J. Cibert, and D. Ferrand, Science 287 (2000) 1019.

[122] Interview with S. Chambers, Nature Mater. 9 (2010) 956.

[123] T. Dietl, H. Ohno, and F. Matsukura, Phys. Rev. B 63 (2001) 195205.

[124] C. Zener, Phys. Rev. B 81 (1951) 440.

[125] D. Dietl, J. Appl. Phys. 89 (2001) 7437.

[126] V.I. Litvinov and V.A. Dugaev, Phys. Rev. Lett. 86 (2001) 5593.

[127] J. Konig, H.H. Lin, and A.H. MacDonald, Phys. Rev. Lett. 84 (2001) 5628.

[128] J. Schliemann, J. Konig, and A.H. MacDonald, Phys. Rev. B 64 (2001) 165201.

[129] D.D. Awschalom, R. Epstein, and R. Hanson, Scientific American 297 (2007) 84.

[130] M. Garbrysch, *Electronic Properties of Diamond:* Uppsala University, (2008).

[131] http://www.cvd-diamond.com/properties_en.htm (Accessed November2011).

[132] V.A. Nadolinny, J.M. Baker, M.E. Newton, and H. Kanda, Diamond and Related Materials 11 (2002) 627.

[133] A.J. Neves, R. Pereira, N.A. Sobolev, M.H. Nazaré, W. Gehlhoff, A. Näser, and H. Kanda, Physica B: Cond. Matter 273-274 (1999) 651.

[134] J. Isoya, H. Kanda, I. Sakaguchi, Y. Morita, and T. Ohshima, Radiat. Phys. Chem. 50 (1997) 321.

[135] R.N Pereira, W. Gehlhoff, N.A. Sobolev, A.J. Neves, and D. Bimberg., Physica B: Cond. Matter 308-310 (2001) 589.

[136] A.M. Edmonds, *Magnetic Resonance of Point Defects in Single Crystal Diamond:* University of Warwick, (2008).

[137] A. Wotherspoon, J.W. Steeds, P. Coleman, D. Wolverson, J. Davies, S. Lawson, and J. Butler., Diamond Rel. Mater. 11 (2002) 692.

[138] T.S. McCauley and Y.K. Vohra, Phys. Rev. B 49 (1994) 5046.

[139] S. Takeyasu, K. Masanori, K. Katsuki, M. Shigeharu, M. Hideaki, H. Yasunori, A. Tanemasa, and K. Akihiko, J. Cryst. Growth 191 (1998) 723.

[140] P. Muret, J. Pernot, A. Kumar, L. Magaud, C. Mer-Calfati, and P. Bergonzo, Phys. Rev. B 81 (2010) 235205-1.

[141] V.I. Polyakov, A.I. Rukovishnikov, N.M. Rossukanyi, V.G. Pereverzev, S.M. Pimenov, J.A. Carlisle, D.M. Gruen, and E.N. Loubnin, Diamond Rel. Mater. 12 (2003) 1776.

[142] J. Shim and E.K. Lee, Phys. Rev. B 71 (2005) 035206.

[143] M.I. Samoilovich, G.N. Bezrukov, and V.P. Butuzov, JETP Lett. 14 (1971) 379.

[144] G. Davies, A.J. Neeves, and M.H. Nazar´e, Europhys. Lett. 9 (1989) 47.

[145] D.J. Twitchen, J.M. Baker, M.E. Newton, and K. Johnston, Phys. Rev. B 61 (2000) 9.

[146] M. Watkins and A. Mainwood, J. Phys. : Condens. Matter 15 (2003) S2913.

[147] G.D. Watkins, Physica B+C 117B/118B (1983) 9.

[148] K. Johnston and A. Mainwood, Diamond Rel. Mater. 11 (2002) 631.

[149] K. Johnston and A. Mainwood, Physica B 565 (2001) 308.

[150] A.T. Collins, Diamond Rel. Mater. 9 (2000) 417.

[151] J.P. Goss, P.R. Brodon, R. Jones, and S. Oberg, J. Phys Condens. Matter 16 (2004) 4567.

[152] R.S. Sussmann, *CVD Diamond for Electronic Devices and Sensors:* John Wiley and Sons Ltd, United Kingdom (2009).

[153] J. Isoya, H. Kanda, J.R. Norris, and M.K. Bowman, Phys. Rev. B 41 (1990) 3905.

[154] D.M. Hofmann, M. Ludwig, P. Christmann, D. Volm, B.K. Meyer, L. Santos, and E. Pereira, Phys. Rev. B 50 (1994) 17618.

[155] J. Isoya, H. Kanda, and Y. Uchida, Phys. Rev. B 42 (1990) 9843.

[156] J.M. Baker, J. Phys. : Condens. Matter 15 (2003) S2929.

[157] S.C. Lawson and H. Kanda, J. Appl. Phys. 73 (1993) 3967.

[158] W. Gehlhoff and R.N. Pereira, J. Phys. : Condens. Matter 14 (2002) 13751.

[159] F. Jelezko and J. Wrachtrup, Phys. Stat. Sol. (a) 203 (2006) 3207.

[160] R. Larico, J.F. Justo, W.V.M. Machado, and L.V.C. Assali, Brazilian J. of Phys. 34 (2004) 669.

[161] X. Jia, S. Hayakawa, W. Li, Y. Gohshi, and M. Wakatsuki., Diamond Rel. Mater. 8 (1999) 1895.

[162] L.V.C. Assali, W.V.M. Machado, R. Larico, and J.F. Justo, Diamond Rel. Mater. 16 (2007) 819.

[163] R. Larico, L.V.C Assali, W.V.M Machado, and J.F. Justo, J. Phys. : Condens. Matter 20 (2008) 415220.

[164] E.B. Lombardi, Diamond Rel. Mater. 17 (2008) 1345.

[165] K. Johnston, A. Mainwood, T.A. Collins, G. Davies, D. Twitchen, J.M. Baker, and M. Newton, Physica B: Cond. Matter 273-274 (1999) 647.

[166] M. Bolduc, C. Awo-Affouda, A. Stollenwerk, M.B. Huang, F.G. Ramos, G. Agnello, and V.P. LaBella, Phys. Rev. B 71 (2005) 033302.

[167] F. Beeler, O.K. Anderson, and M. Sob, *Electronic Bandstructure and its Applications*, edited by M. Yussouff (Springer, Heidelberg, 1987).

[168] A. Bekhti-Siad, A. Mokrani, C. Demangeat, and A. Khelil, J. Mol. Struc. :THEOCHEM 777 (2006) 11.

[169] L.G. Wang and A. Zunger, Phys. Rev. B 66 (2002) 161202(R).

[170] D.M. Wood and A. Zunger, Phys. Rev. B 40 (1989) 4062.

[171] A. Zunger and D.M. wood, J. Cryst. Growth 98 (1989) 1.

[172] S.B. Zhang and A. Zunger, Appl. Phys. Lett. 71 (1987) 677.

[173] H. Kato, T. Makino, S. Yamasaki, and H. Okushi, J. Phys. D: Appl. Phys. 40 (2007) 6189.

[174] E. Gheeraert, S. Koizumi, T. Teraji, H. Kanda, and M. Neslasdek, Diamond Rel. Mater. 9 (2000) 948.

[175] K. Iakoubovskii, A. Stesmans, B. Nouwen, and G.J. Adriaenssens, Phys. Rev. B 62 (2000) 16587.

[176] E. Gheeraert, S. Koizumi, T. Teraji, H. Kanda, and M. Nesladek, Diamond & Rel. Mater. 9 (2000) 948.

[177] R. Jones, J.E. Lowther, and J. Goss, Appl. Phys. Lett. 69 (1996) 2489.

[178] R. Farrer, Solid State Commun. 7 (1969) 685.

[179] E. Nebel and J. Ristein, *Thin Film Diamond I (Semiconductors Science and Semimetals):* Elsevier,Amsterdam, 76.

[180] G. Braunstein and R. Kalish, J. Appl. Phys. 54 (1983) 2106.

[181] T. Vogel, J. Meijer, and A. Zaitsev, Diamond Rel. Mater. 13 (2004) 1822.

[182] R. Kalish, A. Reznik, C. Uzan-Saguy, and C. Cytermann, Appl. Phys. Lett. 76 (2000) 757.

[183] K.-W. Lee and P. W. E. Pickett, Phys. Rev. Lett. (2004) 237003.

[184] T. Yokoya, T. Nakamura, T. Matsushita, T. Muro, Y. Takano, M. Nagao, T. Takenouchi, H. Kawarada, and T. Oguchi, Nature 438 (2005) 647.

[185] T. Dietl, Semicond. Sci. Technol. 17 (2002) 377.

[186] M. Watkins and A. Mainwood, J. Phys. : Condens. Matter 15 (2003) S2913.

[187] L.V.C. Assali, W.V.M. Machado, J.F. Justo, Physica B 404 (2009) 4515.

[188] G. Davies, Physica B 273 (1999) 15.

[189] V.A. Nadolinny, A.P. Yelisseyev, O.P. Yuryeva, and B.N. Feygelson, Appl. Magn. Reson. 12 (1997) 543.

[190] K. Bharuth-Ram, U. Wahl, and J.G. Correia, Nucl. Instrum. Meth. B 206 (2003) 941.

[191] I. Aharonovich, S. Castelletto, D.A. Simpson, A. Stacey, J. McCallum, A.D. Greentree, and S. Prawer, Nano Lett. 9 (2009) 3191.

[192] S. Castelletto, I. Aharonovich, B.C. Gibson, B.C. Johnson, and S. Prawer, Phys. Rev. Lett. 105 (2010) 217403.

[193] I. Aharonovich, J. C. M. S.Castelletto, and S. Prawer, New J. Phys. 13 (2011) 045015.

[194] A. Gali, J.E. Lowther, and P. Deak, J. Phys. : Condens. Matter 13 (2001) 11607-13.

[195] E.D. Seebauer and M.C. Kratzer, Mat. Sc. and Eng. R55 (2006) 57.

[196] H. Ehrenreich and D. Turnbull, *Solid State Physics:* New York Academic Press, New York, 39 (1996) 275.

[197] H. Raebiger, S. Lany, and A. Zunger, Phys. Rev. B 79 (2009) 165202.

[198] A. Zunger, Appl. Phys. Lett. 83 (2003) 57.

[199] S. Lany and A. Zunger, Phys. Rev. B 72 (2005) 035215.

[200] T.C. Moss, Proc. Phys. Soc. B 67 (1954) 775.

[201] E. Burstein, Phys. Rev. 93 (1954) 632.

[202] P. Gold, T. Dietl, T. Fromherz, G. Bauer, and I. Miotkowski, Phys. Rev. B 49 (1994) 7797.

[203] T. Dietl, Nature Mater. 9 (2010) 965.

[204] S. Ohya, K. Takata, and M.Tanaka, http://arxiv. org/abs/1009. 2235 (2010) (Accessed November 2011)

[205] T. Dietl, F. Matsukura, and H. Ohno, Phys. Rev. B 66 (2002) 033203.

[206] S. Lany, H. Raebiger, and A. Zunger, Phys. Rev. B 77 (2008) 241201(R).

[207] C.D. Pemmaraju, T. Archer, D.S. Portal, and S. Sanvito, Phys. Rev. B 75 (2007) 045101.

[208] A. Walsh, J.L.F. Da Silva, and S.H. Wei, Phys. Rev. Lett. 100 (2008) 256401.

[209] S. Sanvito and C.D. Pemmaraju, Phys. Rev. Lett. 102 (2009) 159701.

[210] G.P. Srivastava, *Theoretical Modeling ofSemiconductor Surfaces* (World Scientific, Singapore, 1999).

[211] D. Porezag, M.R. Pederson, and A.Y. Liu, Phys. Rev. B 60 (1999) 14132.

[212] S. Mirbt, S. Sanyal, and P. Mohn, J. Phys. : Condens. Matter 14 (2002) 3295.

[213] P. Söderlind, R. Ahuja, O. Erickson, and B. Johanson, Phys. Rev. B 50 (1994) 5918.

[214] P. Söderlind, J.A. Moriarty, and J.M. Willis, Phys. Rev. B 53 (1996) 14063.

[215] M. Schilfgaarde, V.P. Antropov, and B.N. Harmon, J. Appl. Phys 79, (1996) 4799.

[216] G.W. Ludwig and H.H. Woodbury, Solid State Phys. 13 (1962) 223.

[217] L. Ma, J. Zhao, J. Wang, B. Wang, and G. Wang, Phys. Rev. B 75 (2007) 045312.

[218] P.M. Marcus and V. L. Moruzz, Phys. Rev. B 38 (1998) 6949.

[219] A.M. Zaitsev, Phys. Rev. B 61 (2000) 12909.

[220] H.W.L. Alves, J.L.A. Alves, and J.R. Leite, Mat. Sc. and Eng. B 11 (1992) 285.

[221] R. Larico, L.V.C. Assali, W.V.M. Machado, and J.F. Justo, Appl. Phys. Lett. 84 (2004) 720.

[222] G.B Bachelet, G.A. Baraff, and M. Schl¨uter, Phys. Rev. B 24 (1981) 4736.

[223] S.C. Erwin and W.E. Pickett, Phys. Rev. B 42 (1990) 11056.

[224] T. Dietl, in *Proc. 27th Int. Confe. on the Physics of Semiconductors, Melvile*, edited by J. Men`endez and C.G. Van de Walle (AIP, NY, 2005), p. 56.

[225] C. Liu, F. Yun, and H. Morkoc, J. Mater. Sci. : Mater. Electron 16 (2005) 555.

[226] E. Ruiz, J. Cirera, and S. Alvarez, Coordn. Chem. Rev. 249 (2005) 2649.

[227] A. Bousseksou, C. Vieu, J.F. Letard, P. Demont, J.P. Tuchagues, L. Malaquin, and J. Menegotto, *Molecular Memory with Spin Crossover Complexes:* PCT/FR02/02961,France, 01/11328 (31/08/2001) (2002).

[228] O. Kahn and C.J. Martinez, Science 279 (1998) 44.

[229] O. Kahn and J.P. Launay, Chemtronics 3 (1988) 140.

[230] O. Kahn, Curr. Opin. Solid State Mater. Sci. 1 (1996) 547.

[231] O. Kahn, J. Kröber, and C. Jay, Adv. Mater. 11 (1992) 718.

[232] S. Koshihara, A. Oiwa, M. Hirasawa, S. Katsumoto, Y. Iye, C. Urano, H. Takagi, and H. Munekata, Phys. Rev. Lett. 78 (1997) 4617.

[233] H. Ohno, D. Chiba, F. Matsukura, T. Omiya, E. Abe, T. Dietl, Y. Ohno, and K. Ohtani, Nature 408 (2000) 944.

[234] M. Donath and W. Nolting, *Local-Moment Ferromagnets- Unique Properties for Modern Applications:* Springer-Verlag,Berlin, Heidelberg (2005).

[235] S.L. Zhang, W. Wang, E.H. Zhang, and W. Xiao, Phys. Lett. A 374 (2010) 3234.

[236] M. Wang, R.P. Campion, A.W. Rushforth, K.W. Edmonds, C.T. Foxon, and B. L. Gallaghe, Appl. Phys. Lett. 93 (2008) 132103.

[237] R. Skomski and J.M.D. Coey, *Permanent Magnetism* (IOP Publishing, Bristol, 1999).

[238] J.M.D Coey, J. Versluijs, and M. Venkatesen, J. Phys. D: Appl. Phys. 35 (2002) 2457.

[239] M.P. Marder, *Condensed Matter Physics* (John Wiley & Sons Inc., New York, 2000).

[240] R.A. de Groot, F.M. Muller, P.G. v Engen, and K.H.J. Bushchow, Phys. Rev. Lett. 50 (1983) 2024.

[241] D.D Awschalom and J. Kikwaka, Phys. Today (1999) 33.

[242] H. Ohno, Science 281 (1998) 951.

[243] J.M.D. Coey and S. Sanvito, J. Phys. D: Appl. Phys. 37 (2004) 988.